Total Internal Reflection – Fluorescence Correlation Spectroscopy (TIR-FCS): Application to the Study of Ligand – Receptor Interactions

Punya Navaratnarajah

A dissertation submitted to the faculty of the University of North Carolina at Chapel Hill in partial fulfillment of the requirements for the degree of Doctor of Philosophy in the Department of Biochemistry and Biophysics.

Chapel Hill
2012

Approved by:

Kenneth A. Jacobson, PhD

Gerhard Meissner, PhD

Matthew R. Redinbo, PhD

Nancy L. Thompson, PhD

Richard V. Wolfenden, PhD

ABSTRACT

PUNYA NAVARATNARAJAH: Total Internal Reflection – Fluorescence Correlation Spectroscopy (TIR-FCS): Application to the Study of Ligand – Receptor Interactions (Under the Direction of Nancy L. Thompson)

Ligand-receptor interactions are an integral part of cellular processes. Fully understanding these processes requires that the thermodynamic and kinetic parameters of ligand-receptor interactions be measured. Total internal reflection fluorescence microscopy combined with fluorescence correlation spectroscopy (TIR-FCS) can be used to characterize the interactions between a fluorescent ligand and surface-associated receptors. The overall objective of this work was to develop TIR-FCS so as to ease its implementation, and expand its application to the study of complex ligand-receptor systems.

Theoretical models describing ligand-receptor interactions measured by TIR-FCS depend on numerous parameters, which complicate the identification of optimal experimental conditions. Criteria, that, if satisfied, would yield autocorrelation curves containing significant information about the kinetics, were defined. Parameter space was systematically explored to identify experimental conditions that satisfy the criteria.

Theoretical work has indicated that TIR-FCS curves contain information about nonfluorescent species that associate with receptors and, thereby, alter the interaction of receptors and fluorescent reporter-ligands. Two nonfluorescent species were defined: 1) nonfluorescent effectors (NE) allosterically enhance or inhibit the binding of fluorescent

ligand and receptors; while 2) nonfluorescent competitors (NC) compete with fluorescent species for receptors. To test these theoretical predictions, work was conducted to establish systems consisting of a NE and NC.

The pregnane X receptor (PXR), a transcription factor, peptides derived from co-activator and co-repressor proteins and a PXR ligand, rifampicin, were chosen to test NE theory. It was found that, contrary to the existing model of PXR action, rifampicin fails to allosterically enhance and reduce PXR's affinity for co-activator and co-repressors, respectively. The biological significance of these results is discussed. These findings preclude the system from being used to test NE theory. As co-activators and co-repressors compete for PXR, the system can be used to test NC theory.

An IgG and Fc receptor, FcγRII, were initially chosen to test NC theory. Peptides derived from the antibody binding site on FcγRII were tested to identify those that compete with soluble FcγRII for surface-bound IgG. A poorly soluble peptide that performs this function was identified. An improvement in solubility is required if the system is to be used to test NC theory.

To ammi and thaththi

ACKNOWLEDGEMENTS

I would like to express my profound gratitude and sincere appreciation to Dr. Nancy L. Thompson for her guidance and friendship during my graduate studies at UNC Chapel Hill. She created a unique learning environment that allowed me to become a well-rounded and independent scientist. Owing to her mentorship, I am a better researcher and experimentalist, scientific writer and communicator. Thank you, Nancy.

I would like to express my appreciation to my committee members Dr. Gerhard Meissner, Dr. Richard Wolfenden, Dr. Matthew Redinbo and Dr. Ken Jacobson. Dr. Redinbo, and a member of his lab, Dr. Laurie Betts, provided much helpful and crucial advice with regards the PXR project. Dr. Ken Jacobson kindly allowed me to take part in joint journal clubs between his lab and that of Dr. Klaus Hahn.

I owe a big thank you to Dr. Linda Spremulli whose door was always open to me. Her advice regarding my thesis work and graduate career were greatly appreciated.

I would also like to thank Dr. Barry Lentz for his mentorship early in my graduate career. The Biophysics Program offered a rigorous training for which I am truly grateful.

I am thankful to my fellow lab members Xiang Wang and Bridgett Steele for being both supportive colleagues and friends. I am grateful to Imola Zigoneanu whose advice and encouragement got me through some trying days in lab. I would also like to mention Michelle Itano and Ping Liu, members of the Jacobson Lab, who have been especially kind and helpful to me. Kaiulani Houston (Waters Lab) and Qunzhao Wang

(Lawrence Lab) have always been unselfish with their time, helping me with the HPLC and mass spec, respectively.

I am immensely grateful to my friends in Chapel Hill, particularly Rukie, Dinuka, Laya and Jen, without whom graduate school would have been intolerable. Rukie, I am incredibly lucky to have had you both as a friend and roommate. I am going to miss you, your culinary inventions and the steady supply of good Sri Lankan tea. Dinuka, I look forward to you arranging all our reunions. Laya and Jen thank you for the endless hours of laughter, entertainment and forced trips to Glenwood Av.

Last, but not least, I would like to thank my parents and brother for their unconditional love and unwavering support. They have listened to my concerns and frustrations with great patience these past five years, and given me sound counsel. Above all, I am grateful for a mother and father who have been incredibly selfless in supporting their children, an older brother who is an excellent role model and a family that genuinely enjoys each other's company.

TABLE OF CONTENTS

LIST OF TABLES

LIST OF FIGURES

LIST OF ABBREVIATIONS

AF-2	activation function – 2
ATP	adenosine triphosphate
CCD	charge-coupled device
CHO	Chinese hamster ovary
DLS	dynamic light scattering
DMEM	Dulbecco's modified eagle medium
DMF	dimethylformamide
DMSO	dimethyl sulfoxide
DNA	deoxyribonucleic acid
DBD	DNA binding domain
DNP-cap-DPPE	1,2-dipalmitoyl-*sn*-glycero-3-phosphoethanolamine-N-[6-[(2,4-dinitrophenyl)amino]hexanoyl]
DNP-G	dinitrophenyl – glycine
DPPC	1,2-dipalmitoyl-*sn*-glycero-3-phosphocholine
EDTA	ethylenediaminetetraacetate
EGFP	enhanced green fluorescent protein
ELISA	enzyme-linked immunosorbent assay
ER	estrogen receptor
FCS	fluorescence correlation spectroscopy
FcγRII	mouse Fc receptor
FITC	fluorescein isothiocyanate
FRET	fluorescence resonance energy transfer
GR	glucocorticoid receptor
GST	glutathione S-transferase

HPLC	high-performance liquid chromatography
HRP	horseradish peroxidase
IDM	indomethacin
IgG	immunoglobulin G
NCoR	nuclear receptor co-repressor
PBS	phosphate buffered saline
PPAR	peroxisome proliferator-activated receptor
PXR	pregnane X receptor
PXR-LBD	ligand binding domain of the pregnane X receptor
RID	receptor interaction domain
RXR	retinoid X receptor
SDS-PAGE	sodium dodecyl sulfate polyacrylamide gel electrophoresis
sFcγRII	soluble, extracellular domain of FcγRII
SMRT	silencing mediator for retinoid and thyroid hormone receptors
SRC-1	steroid receptor co-activator – 1
SUV	small unilamellar vesicle
TCEP	tris(2-carboxyethyl)phosphine hydrochloride
TFP	tetrafluorophenyl
TIR	total internal reflection
TIRFM	total internal reflection fluorescence microscopy
FRAP	fluorescence recovery after photobleaching
TNP	trinitrophenyl

LIST OF SYMBOLS

α	angle on incidence
α_c	critical angle
A	average concentration of fluorescent ligand in solution (Chapters 2 and 3)
B	average density of unoccupied, nonfluorescent surface binding sites (Chapter 2)
C	average density of bound, fluorescent surface binding sites (Chapter 2)
d	depth of the evanescent wave
D	solution diffusion coefficient of fluorescent molecules
ε	molar extinction coefficient
$G(\tau)$	fluorescence fluctuation autocorrelation function
$G_a(\tau)$	autocorrelation term related to diffusion through the evanescent wave
$G_s(\tau)$	autocorrelation term related to surface association/dissociation kinetics
h	radius of the observation area in the sample plane defined by the pin hole
I_0	intensity of incident light
K, K_1, K_2	equilibrium association constants for [fluorescent ligand (Chpater 2), fluorescent reporter-ligand (Chapter 4), nonfluorescent competitor (Chapter 4)] and surface binding sites
K_d, K_d'	equilibrium dissociation constants for (SRC-1, co-repressor) and PXR (Chapter 3)
k_1, k_2	association rate constants for (fluorescent reporter-ligand, nonfluorescent competitor) and surface binding sites (Chapter 4)
k_{-1}, k_{-2}	dissociation rate constants for (fluorescent reporter-ligand, nonfluorescent competitor) and surface binding sites (Chapter 4)

k_a, k_d	association, dissociate rate constants for fluorescent ligand and surface binding sites (Chapter 2)
k_{off}	dissociation rate constant for SRC-1 and PXR (Chapter 3)
λ_0	vacuum wavelength of incident light
L_c	nonfluorescent competitor (Chapter 4)
L_f	fluorescent reporter-ligand (Chapter 4)
n_1	refractive index of glass medium
n_2	refractive index of aqueous medium
N_B	average number of unoccupied surface binding sites in the observation area (Chapter 2)
N_C	average number of occupied, fluorescent surface binding sites in the observation area (Chapter 2)
R_r	rate of diffusion parallel to the sample plane through the observation area
R_z	rate of diffusion through the evanescent wave
S	total density of surface binding sites

Chapter 1

Introduction

1.1 Overview

A comprehensive mechanistic understanding of biochemical processes requires that the thermodynamic and kinetic parameters pertaining to the interaction of relevant biological molecules be measured. Several techniques, including isothermal calorimetry and surface plasmon resonance, allow for such measurements. A fluorescence microscopy-based technique, total internal reflection – fluorescence correlation spectroscopy (TIR-FCS), can also be used to study the thermodynamics and kinetics of interacting molecules. TIR-FCS and variations thereof have the advantage that that they are versatile and amenable to live cell imaging, yielding both thermodynamic and spatio-temporal information. The focus of the present work has been the development of TIR-FCS for its application towards the thermodynamic and kinetic characterization of fluorescent molecules in solution that reversibly interact with surface-bound, non-fluorescent molecules. In practical terms, this work facilitates the adoption of the technique to study the interaction between soluble ligands and membrane-bound receptors, as well as the interaction between soluble biological molecules where at least one of the interacting partners is amenable to surface-immobilization.

1.2 Total Internal Reflection Fluorescence Microscopy (TIRFM)

TIR-FCS combines two well established techniques, total internal reflection fluorescence microscopy (TIRFM) and fluorescence correlation spectroscopy (FCS). In TIRFM (*1-3*), evanescent illumination is used to specifically excite fluorescently labeled molecules that are in close proximity to a surface, usually an aqueous/glass interface. Briefly, when light traveling in a medium with refractive index n_1 impinges on an interface with a lower refractive index (n_2) medium, at an angle greater than the critical angle, α_c, where

$$\alpha_c = \sin^{-1}\left(n_2 / n_1\right), \tag{1.1}$$

the light is completely reflected back into the first medium in a process called total internal reflection. During TIR, a component of the incident light propagates parallel to the TIR interface and penetrates into the lower refractive index medium, where the intensity, I(z), decays exponentially with increasing distance, z, from the interface:

$$I(z) = I_0 e^{-z/d}. \tag{1.2}$$

The depth, d, of this exponentially decaying evanescent wave is determined by the vacuum wavelength of the incident light, λ_0, the angle of incidence, α, and refractive indices, n_1 and n_2:

$$d = \frac{\lambda_0}{4\pi\sqrt{n_1^2 \sin^2 \alpha - n_2^2}}. \tag{1.3}$$

The depth of the evanescent wave is typically on the order of 100 nm, and only those fluorescently labeled molecules within this depth are likely to be excited.

1.3 Fluorescence Correlation Spectroscopy (FCS)

As fluorescently labeled molecules diffuse in and out of the observation volume, the fluorescence signal fluctuates. The temporal pattern of these fluorescence fluctuations is altered if the molecules reversibly interact with surface binding sites, for instance, impeding their ability to freely diffuse. FCS (*4-9*) can be used to measure the temporal pattern of fluorescence fluctuations and, thereby, gain insight into the dynamics of the fluorescent species being studied. Towards this end, fluctuations in the fluorescence signal, defined as the difference $(\delta F(t))$ between the instantaneous fluorescence, F(t), and the time-averaged fluorescence, $\langle F \rangle$, are autocorrelated as a function of the lag-time, τ, using the following equation:

$$G(\tau) = \frac{\langle \delta F(t) \delta F(t+\tau) \rangle}{\langle F \rangle^2}. \qquad (1.4)$$

The autocorrelation function, $G(\tau)$, is independent of the time, t, when the system of interest is at equilibrium. $G(\tau)$ decays to zero as τ approaches infinity. The magnitude of this function is inversely related to the average number of fluorescent molecules in the observation volume. The rate of decay and shape of $G(\tau)$ contain information about the processes that affect the pattern of fluorescence fluctuations, including photo-physical dynamics (e.g., triplet state kinetics), solution diffusion, association and dissociation with surface-binding sites, and/or enzyme kinetics.

As FCS monitors the deviation of the instantaneous fluorescence from the time-averaged fluorescence, recording the fluorescence emanating from a large number of fluorescent molecules will only yield ensemble-averaged fluorescence measurements and fluorescence fluctuation autocorrelation functions that are small in magnitude. To obtain

autocorrelation functions with magnitudes large enough to be accurately measured, the average number of fluorescent molecules in the observed volume has to be small. Most FCS measurements are carried out with at most 100 fluorescent molecules in the observed volume. One way to reduce the average number of fluorescent molecules in the observation volume, other than by simply decreasing the concentration, is to reduce the size of the detection volume.

1.4 Total Internal Reflection – Fluorescence Correlation Spectroscopy (TIR-FCS)

TIR-FCS (*10-12*) is used to study the dynamics of fluorescent molecules at surfaces (Figure 1). Apart from conferring surface selectivity, TIR illumination serves to reduce the size of the observation volume via axial confinement and lower the background signal (*13*). However, evanescent illumination does not reduce the detection volume sufficiently to achieve an acceptable number of fluorescent molecules in the observation volume for FCS. Therefore, a circular pinhole (*14, 15*) or fiber optic cable (*16, 17*) placed at a back image plane of the microscope is used to achieve lateral (x-y sample plane) confinement that reduces the observed area to about 1 μm^2. A schematic of the particular TIR-FCS set up we employ is shown in Figure 1.1.

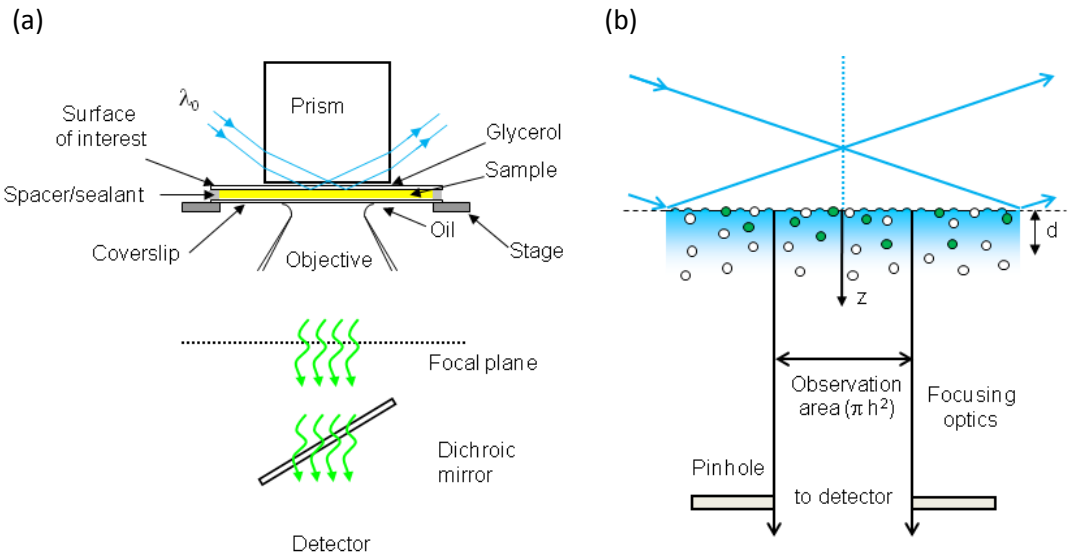

Figure 1.1: Through-Prism TIR-FCS. (a) A laser beam is totally internally reflected at a sample plane through a prism that is mounted on the stage of an inverted microscope. (b) An evanescent wave of depth d excites fluorescence, which is collected through the high-aperture objective and passed through a spectral filter to remove scattered evanescent light. The light is passed through a small aperture, placed at a back image plane of the microscope, before reaching a single-photon counting detector. The detector signal is processed using a computer with a correlator card and associated software. Reproduced with permission from J. Struct. Biol. 2009. 168, 95-106.

In TIR-FCS fluorescence fluctuations arising from fluorescent species that move in and out of the detection volume, undergo photophysics and/or reversibly associate with the surface are autocorrelated (Figure 1.2). Measured autocorrelation functions are fit to theoretical models derived for a given system, to obtain values of the parameters of interest. These theoretical autocorrelation functions take into account the optical arrangement of the excitation and emission pathways, as well as the processes giving rise to the observed fluorescence fluctuations. Many different theoretical models have been described in the literature: triplet state kinetics (*18*); diffusion in the evanescent field (*20-24*); ligand-receptor kinetics (*25, 26*); enzyme kinetics (*27*); cross-correlation TIR-FCS (*28*); and other situations (*16, 17, 29, 30*).

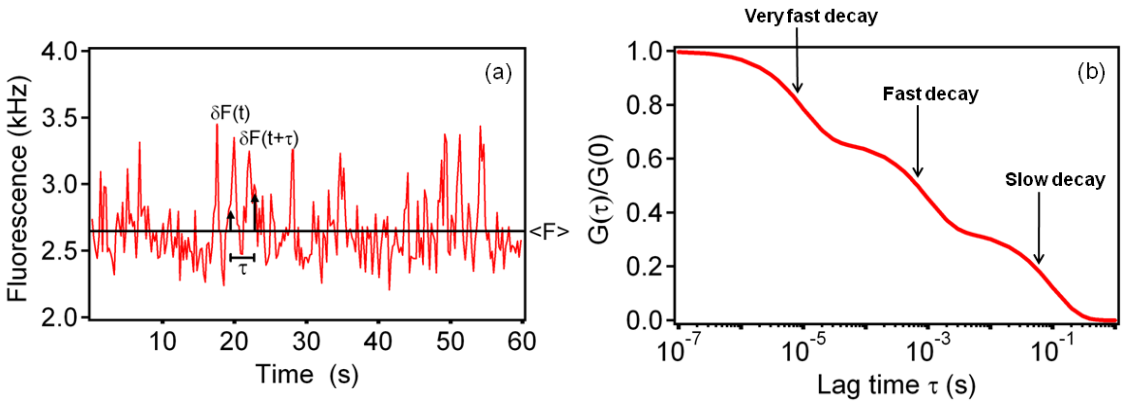

Figure 1.2: Fluorescence Fluctuation Autocorrelation Functions. (a) The fluorescence measured from the observation volume fluctuates with time as individual fluorescent molecules diffuse through the evanescent field, associate with and dissociate from surface binding sites, and/or undergo transitions between states with different detected fluorescence intensities. (b) The temporal fluorescence fluctuations are autocorrelated (see Eq. 1.4). This plot shows an idealized case in which three components with different characteristic rates are present in G(τ); e.g., a very fast decay arising from photophysics, a fast decay arising from free diffusion of the fluorescent molecules through the depth of the evanescent field, and a slow decay resulting from reversible association of the fluorescent molecules with surface sites. Reproduced with permission from Reviews in Fluorescence 2009; Geddes, CD, Ed.; Springer: New York; pp 345-380.

1.5 Outline of Dissertation

In the present work we are concerned with the extension of TIR-FCS to the study of ligand-receptor kinetics. This particular application of TIR-FCS was first demonstrated when the technique was used to examine the kinetics of the mouse Fc receptor, FcγRII, and an IgG (*14*). To conduct these measurements, FcγRII was reconstituted in supported planar membranes deposited on fused silica microscope slides, while the antibody was fluorescently labeled and introduced into the aqueous medium between the microscope slide and cover slip. TIR-FCS was used to measure the fluorescence fluctuations that arose as fluorescently labeled antibodies diffused in and out of the observation volume, and reversibly associated with surface-bound FcγRII. These fluorescence fluctuations were autocorrelated and fit to a theoretical model describing ligand-receptor kinetics to obtain the dissociation rate constant. The autocorrelation

curves obtained for ligand-receptor interactions contained a long-time component that is absent when the fluorescence fluctuations arise due to diffusion alone (Figure 1.3).

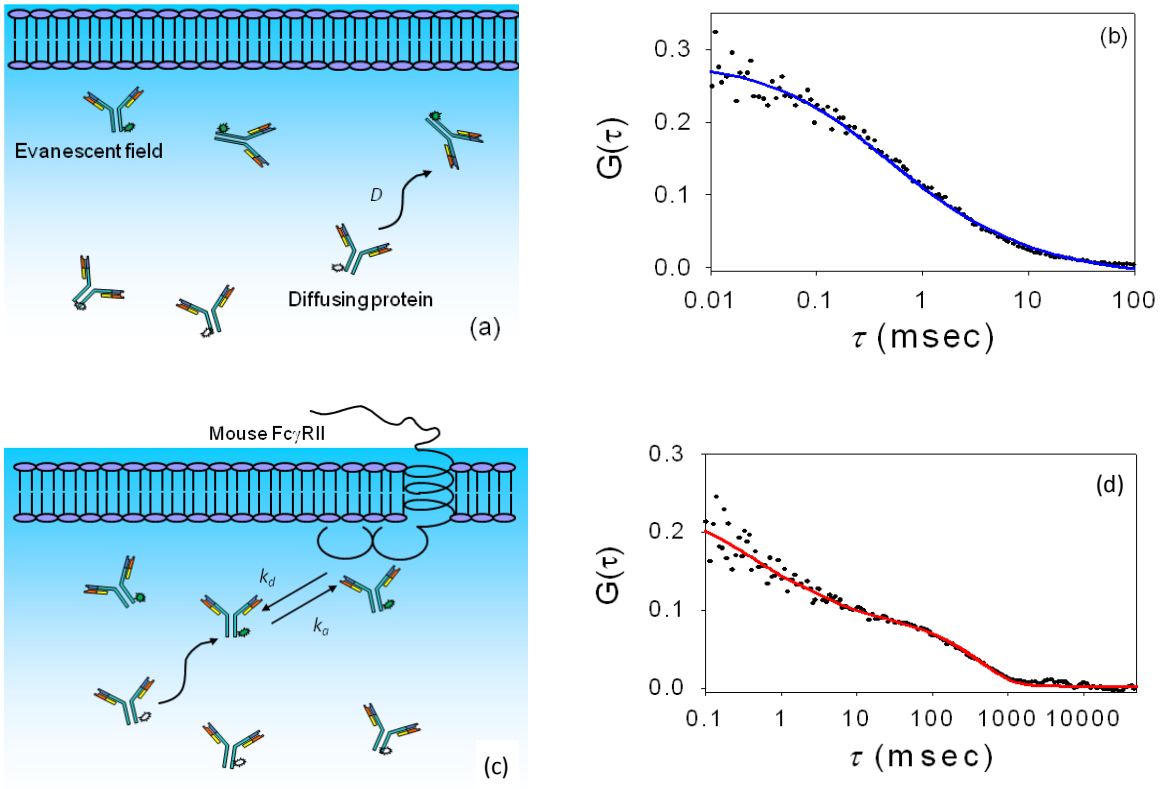

Figure 1.3: IgG Dynamics. (a) Schematic of antibody diffusion close to a supported planar membrane. Fluorophores within the evanescent wave are excited and fluoresce. (b) Representative TIR-FCS data and the best fit to an appropriate theoretical expression. The data are for a mixture of 10 nM Alexa448-labeled IgG, 1 μM unlabeled IgG and 10 mg mL^{-1} ovalbumin in phosphate-buffered saline close to surfaces coated with supported phospholipid bilayers. (c) Schematic of antibodies diffusing close to and reversibly associating with a supported planar membrane containing purified and reconstituted Fc receptors. The parameters k_a and k_d are the association and dissociation rate constants, respectively. d) Representative TIR-FCS data and the best fit to an appropriate theoretical expression. The data are for a mixture of 10 nM Alexa448-labeled IgG, 1 μM unlabeled IgG and 10 mg mL^{-1} ovalbumin in phosphate-buffered saline close to surfaces coated with supported phospholipid bilayers containing approximately 800 receptors per μm^2. Parts (a) and (c) are reproduced with permission from Reviews in Fluorescence 2009; Geddes, CD, Ed.; Springer: New York; pp 345-380. Parts (b) and (d) are reproduced with permission from Biophys. J. 2003. 85, 3294-3302.

1.5.1 Identifying Optimal Experimental Conditions for Measuring Surface Binding Thermodynamics and Kinetics using TIR-FCS

The theoretical model pertaining to ligand-receptor kinetics was extensively described by Lieto and Thompson (*25*). This work showed that numerous experimental

parameters, including the dimensions of the detection volume, concentration of fluorescent ligand and density of surface-bound receptors, affect the magnitude and shape of the autocorrelation curve. As a result, it is difficult to identify experimental conditions that will yield TIR-FCS curves that have high signal-to-noise ratios and contain significant information about the thermodynamic and kinetic parameters of interest. To address this difficulty, we defined criteria that, if satisfied, would yield autocorrelation curves that allow for successful measurement of equilibrium binding constants and rate constants. We then systematically explored the parameter space to identify experimental conditions that would satisfy the criteria. The work is geared to serve as a general guide to determine optimal experimental conditions for TIR-FCS measurements involving different biological systems and thereby ease the implementation of the technique. This work was outlined in a paper I co-authored (*31*) and is included in Chapter 2 of this dissertation.

1.5.2 Establishing Biological Systems to Test TIR-FCS Theory Pertaining to Nonfluorescent Molecules

Previous theoretical work had indicated that TIR-FCS can also be used to measure the thermodynamic and kinetic properties of nonfluorescent molecules that reversibly associate with surface binding sites and thereby interfere with the binding of a fluorescent species (*25, 30*). These nonfluorescent molecules may either *compete* with the fluorescent reporter to bind surface binding sites (*25*), or bind the receptor and allosterically *enhance or reduce* the affinity of the receptor for the fluorescent ligand (Thompson et al., unpublished). As a first step towards determining whether TIR-FCS yields the thermodynamic and kinetic parameters of nonfluorescent molecules in practice,

I set out to implement two biological test systems, one containing a nonfluorescent enhancer and the other, a nonfluorescent competitor.

1.5.2.1 Rifampicin – independent interactions between the pregnane X receptor ligand binding domain and peptide fragments of co-activator and co-repressor proteins

For a test system containing a nonfluorescent enhancer, we chose a nuclear receptor, the pregnane X receptor (PXR), one of its co-activator proteins and an established ligand of PXR, rifampicin. PXR regulates the expression of drug metabolizing enzymes in a ligand-dependent manner (*32*). The existing model of nuclear receptor action states that upon binding agonists, nuclear receptors associate with co-activators, which in turn recruit downstream members of the cell's transcription machinery. We thought to adopt a system in which the PXR agonist rifampicin would serve as a nonfluorescent enhancer and a fluorescently labeled peptide derived from the steroid receptor co-activator 1 (SRC-1) would serve as the fluorescent reporter. The PXR ligand binding domain (PXR-LBD) was in turn immobilized on fused silica microscope slides via a biotin – avidin linkage. As the interaction among PXR, its co-regulator proteins and agonists had not been biophysically characterized prior to this work, we used established techniques, TIRFM and TIRFM combined with fluorescence recovery after photobleaching (TIR-FRAP), to measure the thermodynamics and kinetics of the interaction between PXR-LBD and SRC-1 in the presence and absence of rifampicin. Contrary to expectations, rifampicin did not alter the affinity of PXR-LBD for SRC-1. Although the system could not be used to test TIR-FCS theory pertaining to nonfluroescent enhancers, the work strongly suggested that the mechanism of PXR action differed from that of other nuclear receptors. These findings were published in *Biochemistry* (*33*) and are included in Chapter 3 of this dissertation.

As agonists are also thought to decrease the affinity of nuclear receptors for co-repressors (*34-36*), we used TIRFM to investigate the interaction between PXR-LBD and peptides derived from co-repressor proteins. Again, rifampicin did not alter the affinity of PXR-LBD for its co-repressors. However, as co-activator and co-repressor binding sites on nuclear receptors overlap significantly (*37*), co-activator and co-repressor peptides compete with each other to bind PXR-LBD. We thereby had a system with which to test the nonfluorescent competitor theory. In addition, PXR-LBD and its interacting partners could be used to test the experimental conditions (Chapter 2) that were predicted to yield informative autocorrelation curves with good signal-to-noise ratios.

1.5.2.2 Fc Receptor and IgG Interactions: A Test System for TIR-FCS

To test the nonfluorescent competitor theory, we initially sought to use an IgG and its Fc receptor, FcγRII. Unlike PXR interactions, the interaction between antibodies and their Fc receptors are well characterized (*14*). However, a known competitive inhibitor of IgG/FcγRII binding did not exist. We designed a system in which an IgG, 1B7.11, was immobilized on supported planar membranes via its antigen binding site. The soluble, extracellular portion of FcγRII (sFcγRII) was fluorescently labeled and introduced into the aqueous medium between the microscope slide and cover slip. To obtain nonfluorescent competitors, we synthesized peptides fashioned from the antibody binding site on FcγRII (*38, 39*). One of these peptides was able to compete with sFcγRII to bind surface-bound IgG. However, this peptide was not sufficiently soluble in aqueous media. If this system is to be used for purposes of testing the theory, the solubility of the peptide would have to be improved. The above work is described in Chapter 4 of this dissertation.

1.6 Summary

The motivation for the work described herein was the development and extension of TIR-FCS to the study of ligand-receptor kinetics. We systematically examined TIR-FCS theory pertaining to ligand-receptor interactions to identify experimental conditions that were most likely to yield autocorrelation curves containing significant information about the thermodynamic and kinetic parameters of interest. Subsequent work showed that PXR and antibody/Fc receptor systems could be used to test the predicted experimental conditions. To determine whether TIR-FCS yielded information about nonfluorescent molecules that alter the binding of fluorescent ligands to surface binding sites, we established a system in which peptides derived from co-regulator and co-activator proteins compete with each other to bind surface-bound PXR. In establishing this system, we determined that the PXR agonist, rifampicin, does not alter the affinity of the receptor for peptides derived from co-regulator proteins. These findings have significant implications for the existing model of PXR action, and are of interest to the nuclear receptor community. In future work, we would use the biological systems established herein to test the theoretical predictions and explore the limits of TIR-FCS with regards its application to the study of ligand-receptor interactions.

1.7 References

1. Simon, S. M. (2009) Partial internal reflections on total internal reflection fluorescent microscopy. *Trends in Cell Biology 19*, 661-668.

2. Axelrod, D. (2008) Total internal reflection fluorescence microscopy. *Methods in Cell Biology 89*, 169-221.

3. Schneckenburger, H. (2005) Total internal reflection fluorescence microscopy: technical innovations and novel applications. *Current Opinion in Biotechnology 16*, 13-18.

4. Fitzpatrick J. A. J., Lillemeier, B. F. (2011) Fluorescence correlation spectroscopy: linking molecular dynamics to biological function in vitro and in situ. *Current Opinion in Structural Biology 21*, 650 – 660.

5. Chiantia, S., Reis, J., Schwille, P. (2009) Fluorescence correlation spectroscopy in membrane structure elucidation. Biochimica et Biophysica Acta 1788, 225-233.

6. Chen, H., Farkas, E. R., Webb, W.W. (2008) *In vivo* applications of fluorescence correlation spectroscopy. *Methods in Cell Biology 89*, 3-35.

7. Kolin, D. L., Wiseman, P. W. (2007) Advances in image correlation spectroscopy: Measuring number densities, aggregation states, and dynamics of fluorescently labeled macromolecules in cells. *Cell Biochemistry and Biophysics 49*, 141-164.

8. Haustein, E., Schwille, P. (2007) Fluorescence correlation spectroscopy: Novel variations of an established technique. *Annu. Rev. Biophys. Biom. 36*, 151-169.

9. Blom, H., Kastrup, L., Eggeling, C. (2006) Fluorescence fluctuation spectroscopy in reduced detection volumes. *Current Pharmaceutical Biotechnology 7*, 51-66.

10. Thompson, N. L., Navaratnarajah, P., Wang, X. (2009a) Total internal reflection with fluorescence correlation spectroscopy. *Reviews in Fluorescence 2009*; Geddes, CD, Ed.; Springer: New York; pp 345-380.

11. Thompson, N. L., Wang, X., Navaratnarajah, P. (2009b) Total internal reflection with fluorescence correlation spectroscopy: Applications to substrate-supported planar membranes. *J. Struct. Biol.* 168(1):95-106.

12. Thompson, N. L., Steele, B. L. (2007) Total internal reflection with fluorescence correlation spectroscopy. *Nature Protocol 2*, 878-890.

13. Huang, Z., Thompson, N. L. (1996) Imaging fluorescence correlation spectroscopy: Nonuniform IgE distributions on planar membranes. *Biophysical Journal 70*, 2001-2007.

14. Lieto, A. M., Cush, R. C., Thompson, N. L. (2003) Ligand-receptor kinetics measured by total internal reflection with fluorescence correlation spectroscopy. *Biophysical Journal 85*, 3294-3302.

15. Starr, T. E., Thompson, N. L. (2002) Local diffusion and concentration of IgG near planar membranes: measurement by total internal reflection with fluorescence correlation spectroscopy. *Journal of Physical Chemistry B 106*, 2365-2371.

16. Hassler, K., Anhut, T., Rigler, R., Gösch, M., Lasser, T. (2005a) High count rates with total internal reflection fluorescence correlation spectroscopy. *Biophysical Journal 88*, L01-L03.

17. Hassler, K., Leutenegger, M., Rigler, P., Rao, R., Rigler, R., Gösch, M., Lasser, T. (2005b) Total internal reflection fluorescence correlation spectroscopy (TIR-FCS) with low background and high count-rate per molecule. *Optics Express 13*, 7415-7423.

18. Widengren, J., Mets, U., Rigler, R. (1995) Fluorescence correlation spectroscopy of triplet states in solution: a theoretical and experimental study. *Journal of Physical Chemistry 99*, 13368-13379.

19. Kyoung, M., Sheets, E. D. (2008) Vesicle diffusion close to a membrane: intermembrane interactions measured with fluorescence correlation spectroscopy. *Biophysical Journal 95*, 5789-5797.

20. Borejdo, J., Calander, N., Gryczynski, Z., Gryczynski, I. (2006) Fluorescence correlation spectroscopy in surface plasmon coupled emission microscope. *Optics Express 14*, 7878-7888.

21. Pero, J. K., Hass, E. M., Thompson, N. L. (2006) Size dependence of protein diffusion very close to membrane surfaces: measurement by total internal reflection with fluorescence correlation spectroscopy. *Journal of Physical Chemistry B 110*, 10910-10918.

22. Holt, M., Cooke, A., Neef, A., Lagnado, L. (2004) High mobility of vesicles supports continuous exocytosis at a ribbon synapse. *Current Biology 14*, 173-183.

23. Starr, T. E., Thompson, N. L. (2001) Total internal reflection with fluorescence correlation spectroscopy: combined surface reaction and solution diffusion. *Biophysical Journal 80*, 1575-1584.

24. Johns, L. M., Levitan, E. S., Shelden, E. A., Holz, R. W., Axelrod, D. (2001) Restriction of secretory granule motion near the plasma membrane of chromaffin cells. *Journal of Cell Biology 153*, 177-190.

25. Lieto, A. M., Thompson, N. L. (2004) Total internal reflection with fluorescence correlation spectroscopy: nonfluorescent competitors. *Biophysical Journal 87*, 1268-1278.

26. Thompson, N. L., Burghardt, T. P., Axelrod, D. (1981) Measuring surface dynamics of biomolecules by total internal reflection fluorescence with photobleaching recovery or correlation spectroscopy. *Biophysical Journal 33*, 435-454.

27. Hassler, K., Rigler, P., Blom, H., Rigler, R., Widengren, J., Lasser, T. (2007) Dynamic disorder in horseradish peroxidase observed with total internal reflection fluorescence correlation spectroscopy. *Optics Express 15*, 5366-5375.

28. Leutenegger, M., Blom, H., Widengren, J., Eggeling, C., Gösch, M., Leitgeb, R. A., Lasser, T. (2006) Dual-color total internal reflection fluorescence cross-correlation spectroscopy. *Journal of Biomedical Optics 11*, 1-3.

29. Ries, J., Petrov, E. P., Schwille, P. (2008) Total internal reflection fluorescence correlation spectroscopy: Effects of lateral diffusion and surface-generated fluorescence. *Biophysical Journal 95*, 390-399.

30. Thompson, N. L. (1982) Surface binding rates of nonfluorescent molecules may be obtained by total internal reflection with fluorescence correlation spectroscopy. *Biophysical Journal 38*, 327-329.

31. Thompson, N. L., Navaratnarajah, P., Wang, X. (2011) Measuring surface binding thermodynamics and kinetics by using total internal reflection with fluorescence correlation spectroscopy: Practical considerations. *J. Phys. Chem. B.* 115(1):120-131.

32. di Masi, A., De Marinis, E., Ascenzi, P., and Marino, M. (2009) Nuclear receptors CAR and PXR: Molecular, functional, and biomedical aspects, *Mol. Asp. Med. 30*, 297-343.

33. Navaratnarajah, P., Steele, B. L., Redinbo, M. R., Thompson, N. L. (2012) Rifampicin – independent interactions between the pregnane X receptor ligand binding domain and peptide fragments of coactivator and corepressor proteins, *Biochemistry, in press*.

34. Takeshita, A., Taguchi, M., Koibuchi, N., and Ozawa, Y. (2002) Putative Role of the Orphan Nuclear Receptor SXR (Steroid and Xenobiotic Receptor) in the Mechanism of CYP3A4 Inhibition by Xenobiotics, *J. Biol. Chem. 277*, 32453-32458.

35. Johnson, D. R., Li, C.-W., Chen, L.-Y., Ghosh, J. C., and Chen, J. D. (2006) Regulation and Binding of Pregnane X Receptor by Nuclear Receptor Corepressor Silencing Mediator of Retinoid and Thyroid Hormone Receptors (SMRT), *Molecular Pharmacology 69*, 99-108.

36. Li, C.-W., Dinh, G. K., and Chen, J. D. (2009) Preferential Physical and Functional Interaction of Pregnane X Receptor with the SMRTα Isoform, *Molecular Pharmacology 75*, 363-373.

37. Xu, H. E., Stanley, T. B., Montana, V. G., Lambert, M. H., Shearer, B. G., Cobb, J. E., McKee, D. D., Galardi, C. M., Plunket, K. D., Nolte, R. T., Parks, D. J., Moore, J. T., Kliewer, S. A., Willson, T. M., and Stimmel, J. B. (2002) Structural basis for antagonist-mediated recruitment of nuclear co-repressors by PPAR[alpha], *Nature 415*, 813-817.

38. Goldsmith, E. B., Erickson, B. W., Thompson, N. L. (1997) Synthetic peptides from mouse Fc receptor (moFcγRII) that alter the binding of IgG to moFcγRII. *Biochemistry 36*: 952-959.

39. Sondermann, P., Huber, R., Oosthuizen, V., Jacob, U. (2000) The 3.2-Å crystal structure of the human IgG Fc fragment-FcγRIII complex. *Nature 406*, 267-273.

Chapter 2

Identifying Optimal Experimental Conditions for Measuring Surface Binding Thermodynamics and Kinetics using TIR-FCS

2.1 Overview

The combination of total internal reflection illumination and fluorescence correlation spectroscopy (TIR-FCS) is an emerging method useful for, among a number of things, measuring the thermodynamic and kinetic parameters describing the reversible association of fluorescently labeled ligands in solution with immobilized, nonfluorescent surface binding sites. However, there are many parameters (both instrumental and intrinsic to the interaction of interest) that determine the nature of the acquired fluorescence fluctuation autocorrelation functions. In this work, we define criteria necessary for successful measurements, and then systematically explore the parameter space to define conditions that meet the criteria. The work is intended to serve as a guide for experimental design; in other words, to provide a methodology to identify experimental conditions that will yield reliable values of the thermodynamic and kinetic parameters for a given interaction.

Chapter 2 reproduced with permission from: Thompson, N. L., Navaratnarajah, P., Wang, X. (2011) *Journal of Physical Chemistry B*, 115, 120-131.

2.2 Introduction

Interactions between soluble ligands and membrane-bound species are an integral part of many, if not most, cellular processes. Many disease-causing microorganisms bind cell-surface molecules as a first step in pathogenesis and the subsequent immune response. A majority of pharmaceutical products target cell-surface receptors. Intercellular communication is often facilitated by soluble factors circulating between cells. Numerous intracellular mechanisms involve the interaction of soluble factors with the membranes of sub-cellular organelles, with the factors being present either in the cytosol or within the organelle. Consequently, to fully understand pathogenic processes, determine the mechanism of action of drugs, and characterize both intercellular and intracellular biological processes, the thermodynamic and kinetic parameters of relevant ligand-receptor interactions must be known. Total internal reflection with fluorescence correlation spectroscopy (TIR-FCS) is an emerging technique that allows one to study the reversible interaction between soluble and surface-associated species *(1-5)*.

TIR-FCS combines two established techniques: total internal reflection fluorescence microscopy (TIRFM) and fluorescence correlation spectroscopy (FCS). In TIRFM, a laser beam approaching an interface between two media with different refractive indices, from the higher refractive index side and at an angle greater than the critical angle, is internally reflected. Total internal reflection gives rise to a thin, surface-associated light layer called the evanescent wave. This wave penetrates into the lower refractive index medium, and decays approximately exponentially with increasing distance from the interface. Evanescent illumination can therefore be used to achieve surface specificity and limit the size of the detection volume. In TIR-FCS, a pinhole or

fiber optic, placed at a back image plane, is employed to further reduce this volume. A small detection volume ensures that a small number of fluorescent molecules are observed at a given time, not a large number that would only yield small fluorescence fluctuations. The fluorescence fluctuations arising from number fluctuations are auto-correlated. The magnitude of the fluorescence fluctuation autocorrelation function is inversely related to the average number of fluorescent molecules in the detection volume. The rate and shape of decay of the autocorrelation function contain information about the processes giving rise to the observed fluorescence fluctuations, such as diffusion through the evanescent wave or reversible association with the surface. To obtain values of the parameters describing these processes from TIR-FCS autocorrelation functions, knowledge of the appropriate theoretical form for a given optical arrangement and molecular process is required.

TIR-FCS has thus far been used primarily to investigate the mobility of small fluorescent molecules close to surfaces (*6-12*). TIR-FCS has also been used to characterize the diffusion coefficients of fluorescently labeled proteins (*13, 14*) and particles (*15*) close to supported phospholipid membranes; molecular transport in sol-gel films (*16-18*), and the mobility of intracellular vesicles very close to the basal membranes of live, adherent cells (*19, 20*). In addition, TIR-FCS has been used to study the reversible interaction of fluorescent species with surfaces; i.e., fluorescently labeled IgG and insulin with albumin-coated surfaces (*21*), rhodamine 6G with C_{18}-coated silica (*22-23*), fluorescently labeled bovine serum albumin and *Thermomyces lanuginosus* lipase with C_{18}-coated glass in the presence of surfactants (*24*), and fluorescently labeled IgG with Fc receptors reconstituted in supported planar membranes (*25*). Applications to

enzyme kinetics (*26*), triplet state photo-physics (*27, 28*), and the association of cytosolic molecules with the basal membranes of live, adherent cells (*7, 29, 30*) have also been reported.

The use of TIR-FCS to examine the thermodynamic and kinetic parameters of soluble, fluorescent ligands reversibly associating with non-fluorescent surface binding sites is a promising method because it requires very small amounts of material. First, the fluorescence fluctuation autocorrelation functions obtained from FCS, in general, are roughly inversely proportional to the average number of fluorescent molecules within the observed volume. Therefore, TIR-FCS has the advantage of requiring low concentrations of fluorescent ligands. Second, because the non-fluorescent binding sites are present in a monomolecular layer on a surface, only small amounts of these molecules are also required. Another advantage of TIR-FCS is related to its recent combination with high-speed imaging detectors (*30-33*). This arrangement, coupled with microfluidic devices, promises high throughput acquisition of numerous fluorescence fluctuation autocorrelation functions (e.g., as a function of the fluorescent ligand concentration and surface site density) from a single time-sequence of images and therefore rapid dissection of surface binding mechanisms.

TIR-FCS autocorrelation functions are predicted to depend on many different parameters; so many that it is difficult to readily identify experimental conditions that will yield autocorrelation curves that contain significant information about the thermodynamic and kinetic parameters which describe the interaction of fluorescent ligands with non-fluorescent surface binding sites. Therefore, in this work, we evaluate the parameter space in a systematic manner to identify viable experimental conditions.

First, a set of criteria necessary for the autocorrelation curves to contain the desired information with high signal-to-noise ratios are defined. Then the previously derived theoretical form of the autocorrelation function is used to determine the experimental conditions that meet these criteria. The results are somewhat surprising in the inferred limitations on experimental parameters (primarily, upper limits on the allowed concentrations of fluorescent ligands given a defined equilibrium association constant). While many conditions are predicted not to yield viable TIR-FCS data, a number of conditions that are likely to yield productive data are identified. Thus, the results presented in this paper serve as a comprehensive guide to the design of TIR-FCS measurements aimed at measuring the kinetic and thermodynamic parameters describing the association of fluorescent ligands with non-fluorescent surface binding sites. Also, the work described here serves as a prerequisite for the design of measurements aimed at using a single, well characterized fluorescent reporter to scan non-fluorescent, soluble competitors for the thermodynamic and kinetic properties describing reversible association with the non-fluorescent surface binding sites (*34, 35*). Similarly, a single fluorescent reporter might be used to characterize non-fluorescent effectors that non-competitively interact with binding sites and enhance or reduce fluorescent reporter binding.

2.3 Theoretical Background

2.3.1 Total Internal Reflection with Fluorescence Correlation Spectroscopy

Figure 2.1 illustrates the conceptual basis of TIR-FCS. Measurements are carried out on an inverted optical microscope. The sample plane, containing surface-binding sites for soluble fluorescent ligands, is the interface between optically transparent high

and low refractive index materials (usually fused silica or glass and a buffered aqueous solution, respectively) and is placed at the focal plane of the microscope. Positions within the sample plane are described by polar coordinates (r, φ) and the distance from the sample plane into the lower refractive index medium is defined by coordinate $z \geq 0$. An excitation source is internally reflected at the sample plane, creating a thin, surface-associated evanescent wave in the lower refractive index medium. Internal reflection may be generated by using either a through-prism or through-objective mechanism. The evanescent excitation intensity is assumed to decay exponentially with position z and characteristic distance d (usually ≈ 0.1 μm). Worth noting is that this assumption may not be completely accurate, as previously reviewed (*1*), but that deviations from exponential behavior, if they occur, are expected to be minimal. The observed volume is further defined by a pinhole or fiber optic placed at a back image plane of the microscope. It is assumed that the observation area in the sample plane, as defined by the back image plane detection restriction, is circular with radius $h \approx 0.5$ μm and area $\approx \pi h^2$. Furthermore, the spatial extent of the evanescent intensity within the sample plane is assumed to be large enough so that the evanescent intensity within the observation volume does not depend on r. At chemical and thermal equilibrium, individual fluorescent molecules diffuse in solution within the observation volume, and also bind to and dissociate from surface binding sites. The fluorescence arising from the observation volume, defined by the evanescent excitation and projected area of the back image plane aperture on the sample plane, is collected through a high numerical aperture objective, detected by a sensitive photomultipler or silicon avalanche diode, and is denoted as F(t). Because only a small number of fluorescent molecules are within the observed volume,

the fluorescence fluctuates significantly with time. The fluorescence fluctuations, $\delta F(t) = F(t) - \langle F \rangle$, where the brackets denote equilibrium (i.e., time-averaged or ensemble-averaged) values, are auto-correlated. The normalized, dimensionless autocorrelation function is defined as

$$G(\tau) = \frac{\langle \delta F(\tau) \delta F(0) \rangle}{\langle F \rangle^2} \tag{2.1}$$

and contains information about diffusion through the evanescent wave in addition to surface binding kinetics.

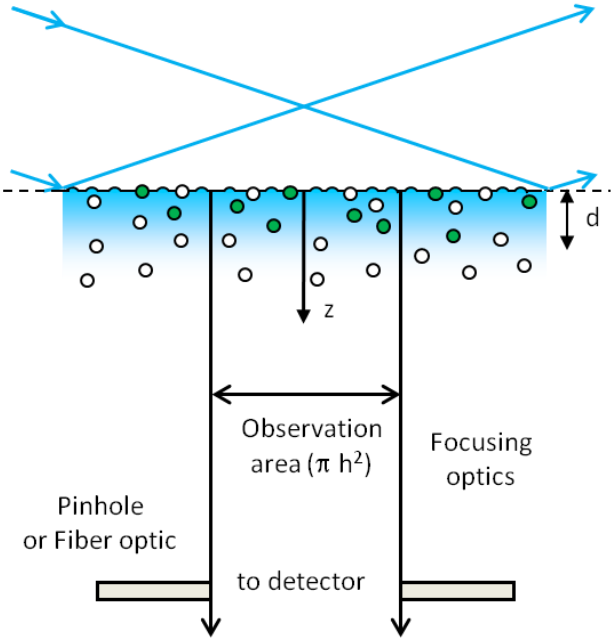

Figure 2.1: TIR-FCS. A laser beam is totally internally reflected at a planar interface between media with two different refractive indices, creating an evanescent field that penetrates a depth d into the lower refractive index medium. A small sample volume is defined by this depth in combination with a circular aperture or fiber optic placed at an intermediate image plane of the microscope that defines an area of radius h in the sample plane. The fluorescence measured from the small sample volume adjacent to the surface fluctuates with time as individual fluorescent ligands diffuse into the volume, bind to surface-associated receptors, dissociate, and diffuse out of the volume. These fluorescence fluctuations are autocorrelated and fit to theoretical expressions to obtain information about the dynamics at or near the surface.

2.3.2 Reaction Mechanism

Consider a situation in which a single fluorescent species in solution interacts with binding sites on a surface through a simple, reversible bimolecular reaction (Figure 2.2). Fluorescent molecules in solution with average concentration A are in equilibrium with unoccupied, nonfluorescent surface binding sites of average density B, forming an average density of fluorescent, surface-bound complexes, C. The surface association and dissociation rate constants are denoted by k_a and k_d, respectively. The mechanism can be written as

$$A + B \underset{k_d}{\overset{k_a}{\leftrightarrow}} C \tag{2.2}$$

where the equilibrium association constant describing the reaction is

$$K = \frac{k_a}{k_d} = \frac{C}{AB} \tag{2.3}$$

The total surface site density is denoted by S. Thus,

$$S = B + C \qquad B = \frac{S}{1 + KA} \qquad C = \frac{KAS}{1 + KA} \tag{2.4}$$

The total number of surface binding sites within the observed area is defined as N. In this case,

$$N = \pi h^2 S = N_B + N_C \qquad N_B = \frac{N}{1 + KA} \qquad N_C = \frac{KAN}{1 + KA} \tag{2.5}$$

where N_B is the average number of unoccupied binding sites in the observed area and N_C is the average number of surface-bound fluorescent molecules in the observed area.

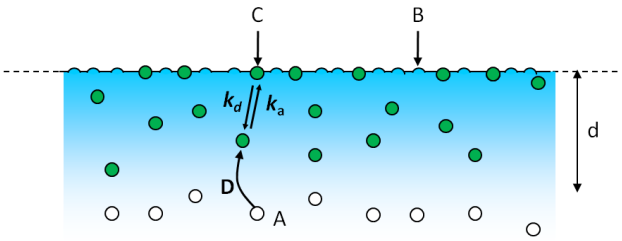

Figure 2.2: Reaction Mechanism. Fluorescent molecules in solution, A, reversibly bind to non-fluorescent surface sites, B, forming fluorescent complexes, C. The association and dissociation rates constants are k_a and k_d, respectively. The solution diffusion coefficient is D. The surface binding sites and surface-bound complexes are not laterally mobile.

2.3.3 Fluorescence Fluctuation Autocorrelation Function

A general expression for G(τ) which accounts for fluorescence fluctuations arising from diffusion through the evanescent field and from surface association and dissociation has previously been published (*36*). In this work, it is assumed that the surface binding sites and surface-associated complexes are not laterally mobile along the surface. Furthermore, it is assumed that the excitation intensity is low enough so that photo-physical processes do not contribute significantly to G(τ). The first assumption can be proven by using fluorescence recovery after photobleaching and the second can be shown by acquiring data as a function of the excitation intensity. The published general expression is rather complex (*36*). In the work described here, we consider the more simple form for G(τ) which is applicable when (1) the rates for diffusion in solution through the observation volume are much faster than the rates associated with surface association and dissociation and (2) rebinding of previously dissociated fluorescent molecules within the small observed area is negligible. In this case,

$$G(\tau) = G_s(\tau) + G_a(\tau) \qquad (2.6)$$

where the first term describes contributions to the autocorrelation function from surface binding kinetics and the second term describes contributions from diffusion of fluorescent molecules in solution but within the evanescent wave.

2.3.4 Magnitude of the Fluorescence Fluctuation Autocorrelation Function

Because the observation volume is open with respect to coordinate z, fluctuations in the concentration of fluorescent molecules in solution obey Poisson statistics. However, because there is a finite number of surface binding sites in the observed area, fluctuations in the densities of surface-bound species obey binomial rather than Poisson statistics. These statements lead to the conclusion that (*36*)

$$G_a(0) = \frac{N_A}{2(N_C + N_A)^2} \qquad G_s(0) = \frac{N_B N_C}{N(N_C + N_A)^2} \tag{2.7}$$

where the average number of unbound fluorescent molecules in the observed volume is

$$N_A = \pi h^2 dA \tag{2.8}$$

It is convenient to define a dimensionless quantity proportional to the solution concentration, X = KA. In this case, Eqs. 2.7 can be rewritten as

$$G_a(0) = \frac{dK(1+X)^2}{2\pi h^2 X[KS + d(1+X)]^2} \qquad G_s(0) = \frac{K^2 S}{\pi h^2 X[KS + d(1+X)]^2} \tag{2.9}$$

2.3.5 Time-Dependence of $G_a(\tau)$

As shown previously (*9*, *36*),

$$\frac{G_a(\tau)}{G_a(0)} = [(1 - 2R_z\tau)\exp(R_z\tau)erfc(\sqrt{R_z\tau}) + 2\sqrt{\frac{R_z\tau}{\pi}}][\frac{1}{1+R_r\tau}]$$
$$R_z = \frac{D}{d^2} \qquad R_r = \frac{4D}{h^2} \tag{2.10}$$

where D is the diffusion coefficient of the fluorescent molecules in solution, R_z is the rate associated with diffusion in solution perpendicular to the surface and through the depth of the evanescent wave, and R_r is the rate associated with diffusion in solution parallel to the surface and through the extent of the observed area. Both factors in the first expression in Eq. 2.10 equal one when $\tau = 0$ and monotonically decay to zero as $\tau \rightarrow \infty$. For a protein with a molecular weight of ≈ 100 kD, D ≈ 50 $\mu m^2 sec^{-1}$. Typically, d ≈ 0.1 μm, and h ≈ 0.5 μm, so that, for this value of D, $R_z \approx (0.2\ ms)^{-1}$ and $R_r \approx (1.25\ ms)^{-1}$. The minimum decay rate of $G_a(\tau)$ is R_z; R_r only speeds the decay.[1]

2.3.6 Time-Dependence of $G_s(\tau)$

Given the assumptions that the rates for diffusion in solution through the observation volume are much faster than the rates associated with surface association and dissociation and that rebinding of previously dissociated fluorescent molecules within the small observed area is negligible, $G_s(\tau)$ has the form of an exponential decay (*36*, *37*):

$$\frac{G_s(\tau)}{G_s(0)} = \exp(-\lambda\tau) \qquad \lambda = k_d + k_a A = k_d(1+X) \tag{2.11}$$

The first expression decays from one to zero with time.

2.4 Results

2.4.1 Measurement of K by Steady-State TIRFM

Independent of TIR-FCS, the simplest method for measuring the value of the equilibrium association constant is by using steady-state TIRFM (*38-42*). In this approach, the evanescently excited fluorescence is measured as a function of the concentration of fluorescent molecules in solution. The data are of the form

$$F_{pos}(A) = Q[\frac{KAS}{1+KA} + dA]$$
$$F_{neg}(A) = QdA \qquad (2.12)$$

where $F_{pos}(A)$ is the fluorescence measured for surfaces containing binding sites, the first term in $F_{pos}(A)$ arises from fluorescent ligands bound to surface sites, the second term in $F_{pos}(A)$ arises from fluorescent molecules in solution but close enough to the surface to be excited by the evanescent wave, $F_{neg}(A)$ is the fluorescence measured for surfaces not containing binding sites, and Q is a proportionality constant.

The difference between the fluorescence measured in the presence (S > 0) and absence (S = 0) of surface binding sites has the shape of a standard binding isotherm which can be curve-fit as a function of A to find the best value of K (and QS). The primary limitation of this type of measurement is that the surface site density in the positive samples must be high enough so that the first term in Eq. 2.12 is not overwhelmed by the second term. This feature is illustrated in Figure 2.3. As shown, higher binding site densities are required for lower values of K. If a general rule is set that the fluorescence measured in the presence of binding sites must be at least twice that measured in the absence of binding sites when $A = K^{-1}$, then one finds that $S \geq 2d/K$. Thus, when d = 0.1 μm, the approximate lower limit for S ranges from 12,000 molecules/μm^2 for $K = 10^4 M^{-1}$ to 12 molecules/μm^2 for $K = 10^7 M^{-1}$. In addition, for adequate curve-fitting, because the value of QS and therefore the saturation point is usually unknown, data must be acquired for solution concentrations up to at least (approximately) 4/K, where the surface binding sites are 80% occupied.

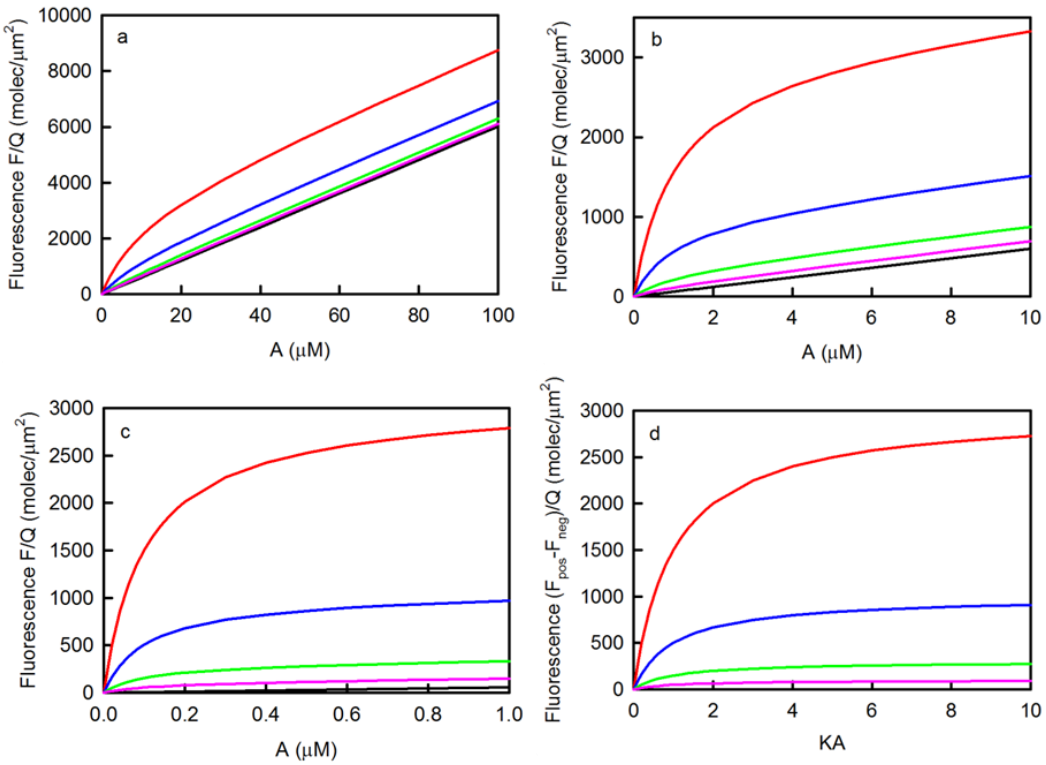

Figure 2.3: Measurement of K by Steady-State TIRFM. These plots show the values of Eq. 2.12 for d = 0.1 μm and K equal to (a) $10^5 M^{-1}$, (b) $10^6 M^{-1}$ or (c) $10^7 M^{-1}$. The surface site densities S in units of molecules/μm^2 are (red) 3000, (blue) 1000, (green) 300, (pink) 100 or (black) zero. The difference between the values shown in (a-c) with S > 0 and with S = 0 have the same shape when plotted as a function of the product of K and A and are shown in panel (d).

2.4.2 Criteria for TIR-FCS

As shown in the previous section, G(τ) is predicted to depend on a rather large number of parameters, some of which are experimentally adjustable and some of which will be intrinsic to a given system of interest. Because so many parameters are present in the expression specifying the autocorrelation function and because all measured G(τ) will contain experimental uncertainties, identifying combinations of the parameter values which can be reasonably predicted to allow characterization of the mechanism shown in Figure 2.2 is not straightforward. Referring to Eqs. 2.6 and 2.9-2.11, one finds that the expression for G(τ) depends on seven independent parameters: K, k_d, X, d, h, D and S (Table 2.1). To make analysis tractable, we have set the values of d (0.1 μm), h (0.5 μm),

and D (50 $\mu m^2 s^{-1}$), leaving four free parameters rather than seven. In addition, in many cases we have assumed that $k_a = 10^6\ M^{-1}s^{-1}$ as is common for processes at surfaces, thus fixing the value of k_d given a value for K, leaving three free parameters: K, X, and S. Although these selections may not apply to a given system being considered for investigation, the procedure we outline below is readily amenable to generalization.

Table 2.1: Parameters Governing the Behavior of G(τ)

Parameter	Description
A	average concentration of fluorescent molecules in solution
K (*)	equilibrium association constant for fluorescent molecules and surface binding sites
X (*)	product of K and A
k_a (***)	kinetic association rate constant for fluorescent molecules and surface binding sites
k_d	kinetic dissociation rate for fluorescent molecules and surface binding sites
S (*)	total surface site density
d (**)	evanescent wave depth
h (**)	radius of observed area
D (**)	solution diffusion coefficient of fluorescent molecules
R_z	rate for diffusion in solution of fluorescent molecules through the evanescent wave
R_r	rate for diffusion in solution of fluorescent molecules through the observed area

There are three free (*), three fixed (**) and one partially fixed (***) parameters. The other four quantities depend on different subsets of these parameters as described in the text.

This work addresses combinations of the values of the three free parameters which will reasonably allow measurement by TIR-FCS of properties describing the thermodynamic and kinetic behavior of the mechanism shown in Figure 2.2. The criteria that we use are defined in Table 2.2: (A) G(τ) decays with reasonable rapidity so that data can be acquired in a reasonable amount of time. (B) Diffusion through the evanescent wave is fast enough so that Eqs. 2.6 and 2.11 are applicable (*36*); worth noting is that R_r only increases the decay rate of $G_a(\tau)$ over that determined by R_z.[1] (C) $G_s(0)$ is high enough so that $G_s(\tau)$ is measurable with high accuracy. Although

fluorescence fluctuation autocorrelation functions with magnitudes much lower than the minimum given in Table 2.2 are often measurable, in all but the simplest case (Eq. 2.11), $G_s(\tau)$ is not a single exponential (*35*) and higher values of $G_s(0)$ are required to resolve, for example, the rates and relative amplitudes associated with two exponentials. (D) The magnitude of $G_s(\tau)$ is high enough so that $G(\tau)$ is not dominated by $G_a(\tau)$. (E) Significant rebinding to the surface within the observed area does not occur so that Eqs. 2.6 and 2.11 are applicable.

Table 2.2: Criteria

Criterion	Description	Quantification
A	fluorescence fluctuations must be fast enough	$\lambda \geq 0.1\ s^{-1}$
B	diffusion through the evanescent wave must be fast enough	$\lambda \leq 500\ s^{-1}$
C	magnitude of $G_s(\tau)$ is high enough	$G_s(0) \geq 0.05$
D	$G_s(\tau)$ is not overwhelmed by $G_a(\tau)$	$G_s(0)/G_a(0) \geq 0.1$
E	surface rebinding is negligible	$P \leq 0.05$

This table describes the criteria used to determine conditions for which TIR-FCS can measure thermodynamic and kinetic parameters describing the interaction of fluorescent molecules with surface binding sites given that the mechanism is a simple bimolecular reaction as defined in Eq. 2.2.

2.4.3 Experimental Conditions that Meet the Criteria

Criterion A requires that the fluorescence fluctuations be fast enough for $G(\tau)$ to be measurable with a good signal-to-noise ratio. We have quantified this criterion by specifying that $G_s(\tau)$ decays with a rate $\geq 0.1\ s^{-1}$. Referring to Eq. 2.11, one sees that the decay rate for $G_s(\tau)$ will always be $\geq k_d$. Thus, assuming that $k_a = 10^6\ M^{-1}s^{-1}$ (see above), $K \leq 10^7\ M^{-1}$ (Eq. 2.3).

Criterion B requires that the decay rate of $G_s(\tau)$ be at least ten times slower than R_z ($5000\ s^{-1}$). To determine k_a, it would be far above sufficient to obtain $G(\tau)$ for values of $k_aA = 4k_d$ ($\lambda = 5k_d$ in Eq. 2.11). In this case, the decay rate of $G_s(\tau)$ for $K = 10^7\ M^{-1}$

would range from 0.1 to 0.5 s^{-1}, meeting criterion B. The minimum value of $5k_d$ is 500 s^{-1}, implying that (with $k_a = 10^6\ M^{-1}s^{-1}$) $K \geq 10^4\ M^{-1}$.

Criteron C requires that $G_s(0) \geq 0.05$. Although this condition might seem to be too restrictive, it has been adopted primarily because we are ultimately interested in $G_s(\tau)$ that are more complex than Eq. 2.11 (see above). $G_s(0)$ depends on three independent parameters (K, S and X) (Eq. 2.9), not including those that have been set at fixed values (h and d). Table 2.3 shows the conditions which conform to criterion C for different values of K, S and X. Worth noting first is that the partial derivative of $G_s(0)$ with respect to X is negative, indicating that $G_s(0)$ increases with decreasing X for set values of S and K. Second, the partial derivative of $G_s(0)$ with respect to K is positive, indicating that $G_s(0)$ increases with increasing K for set values of S and X. Third, the situation is a bit more complex when one considers the dependence of $G_s(0)$ on S. In this case, each value of K and X has a value of S for which $G_s(0)$ is maximized, found from the partial derivative of $G_s(0)$ with respect to S. These values of S, denoted by S_{max}, are

$$S_{\max} = \frac{d(1+X)}{K} \tag{2.13}$$

and are shown in Table 2.3. By using Eq. 2.13 in Eq. 2.9, one finds that, when $S = S_{max}$,

$$[G_s(0)]_{\max} = \frac{K}{4\pi h^2 dX(1+X)} \tag{2.14}$$

These values are shown as upper limits in Table 2.3. Eq. 2.14 implies a maximum value of X, which is found by setting this expression equal to 0.05 and solving for X. The result is

$$X_{\max} = \frac{1}{2}\left[-1+\sqrt{1+\frac{20K}{\pi h^2 d}}\ \right] \tag{2.15}$$

The values of X_{max} are given as upper limits in Table 2.3. Fourth, there are two values of S for which $G_s(0) = 0.05$ (criterion C), denoted as $S_{1,2}$, which bracket the acceptable range of surface site densities. These values, found by setting $G_s(0)$ in Eq. 2.9 equal to 0.05, are

$$S_{1,2} = \frac{10K - \pi h^2 dX(1+X) \mp 10\sqrt{K^2 - \frac{\pi}{5} h^2 dKX(1+X)}}{\pi h^2 KX}. \qquad (2.16)$$

S_1 and S_2 are real for $X \leq X_{max}$. When $X=X_{max}$, the square root in Eq. 2.16 is zero and $S_1=S_2=S_{max}$. In some cases, the minimum value of S, S_1, is < 1 molecule/μm^2. Because h = 0.5 μm, the approximate size of the observed area is $\pi h^2 = 0.8$ μm^2 so that, for these low values of S, some observed areas will contain no binding sites. In other cases, the maximum value of S, S_2, is very high and may not be experimentally achievable. However, criterion E reduces these maximum values to experimentally reasonable ones (see below). The values of $G_s(0)$ as a function of X, for different values of K and $S = S_{max}$ are plotted in Figure 2.4a. As shown, in many cases $G_s(0) >> 0.05$.

Table 2.3: Conditions for which Criteria A-E are satisfied

			S range			P range		ρ range		$G_s(0)$			$G_s(0)/G_a(0)$	
K	X	A	lower	S_{max}	upper	lower	upper	lower	upper	lower	S_{max}	upper	lower	upper
10^7	0.0001	0.01	0.30	6.0	3300	5×10^{-6}	0.05	0.050	550	95	530	3.8	0.10	1100
	0.300	30	0.90	7.8	68	1×10^{-5}	9×10^{-4}	0.15	11	0.050	0.14	0.050	0.18	13
	0.643	64.3	9.9	9.9	9.9	1×10^{-4}	1×10^{-4}	1.6	1.6	0.050	0.050	0.050	1.2	1.2
3×10^6	0.0001	0.0333	1.0	20	3300	2×10^{-5}	0.05	0.050	160	29	160	3.8	0.10	330
	0.100	33.3	2.3	22	210	4×10^{-5}	0.003	0.11	10	0.050	0.14	0.050	0.19	17
	0.253	84.3	25	25	25	3×10^{-4}	3×10^{-4}	1.2	1.2	0.050	0.050	0.050	1.6	1.6
10^6	0.0001	0.1	3.0	60	3300	5×10^{-5}	0.05	0.050	55	9.5	53	3.7	0.10	110
	0.030	30	5.4	62	720	9×10^{-5}	0.01	0.090	12	0.050	0.17	0.050	0.17	23
	0.0964	96.4	66	66	66	0.001	0.001	1.1	1.1	0.050	0.050	0.050	1.8	1.8
3×10^5	0.0001	0.33	10	201	3300	2×10^{-4}	0.05	0.050	16	2.9	16	3.4	0.10	33
	0.010	33.3	19	203	2100	3×10^{-4}	0.03	0.095	10	0.050	0.16	0.050	0.19	21
	0.0308	103	207	207	207	0.003	0.003	1.0	1.0	0.050	0.050	0.050	1.9	1.9
10^5	0.0001	1	30	602	3300	5×10^{-4}	0.05	0.050	5.5	0.95	5.3	2.8	0.10	11
	0.003	30	50	604	3300	8×10^{-4}	0.05	0.083	5.5	0.050	0.18	0.092	0.17	11
	0.0105	105	609	609	609	0.01	0.01	1.0	1.0	0.050	0.050	0.050	2.0	2.0
3×10^4	0.0001	3.33	100	2008	3300	0.002	0.05	0.050	1.6	0.29	1.6	1.5	0.10	3.3
	0.0010	33.3	190	2010	3300	0.003	0.05	0.094	1.6	0.050	0.16	0.15	0.19	3.3
	0.00316	105	2014	2014	2014	0.03	0.03	1.0	1.0	0.050	0.050	0.050	2.0	2.0
10^4	0.0001	10	301	6025	3300	0.005	0.05	0.050	0.55	0.096	0.53	0.48	0.10	1.1
	0.0003	30	502	6026	3300	0.008	0.05	0.083	0.55	0.050	0.18	0.16	0.17	1.1
	0.000965	96.5	3300	6030	3300	0.05	0.05	0.55	0.55	0.05	-	0.05	1.1	1.1
	0.00106	106	6030	6030	3300	-	-	-	-	-	-	-	-	-

K values are in units of M^{-1}, A values are in units of nM, and surface site densities are in units of molecules/μm^2. All other quantities are unitless. S_{max} was calculated by using Eq. 13. The allowed values of S range from the maximum of S_1 and S_3, to the minimum of S_2 and S_4. S_1 and S_2 were calculated by using Eq. 16, S_3 was calculated by using Eq. 18, and S_4 was found numerically as described in the text. P, ρ, $G_s(0)$ and $G_s(0)/G_a(0)$ were calculated for the lower and upper limits of S by using Eqs. 19 & 20, Eq. 23, Eq. 9 and Eq. 17, respectively. P, ρ and $G_s(0)/G_a(0)$ all increase monotonically with S. $G_s(0)$ peaks when $S = S_{max}$; these values were calculated by using Eq. 14.

Criteron D requires that the ratio of $G_s(0)$ and $G_a(0)$ be ≥ 0.1, so that the long-time tail of $G_a(\tau)$ does not overlap too much with $G_s(\tau)$. This ratio (see Eqs. 2.9) is

$$\frac{G_s(0)}{G_a(0)} = \frac{2KS}{d(1+X)^2} \tag{2.17}$$

and, as shown, increases with K and S; and decreases with X and d. However, when S = S_{max}, $G_s(0)/G_a(0) = 2/(1 + X)$ and depends only on X (Figure 2.4b). In this case, because X is always less than or approximately equal to 0.64 (Table 2.3), the ratio ranges from ≈ 2 at low X to 1.2, well above 0.1. In general, for a given value of K and X, an initial maximum value of $G_s(0)/G_a(0)$ can be found with $S = S_2$. As shown in Figure 2.4b, these maximum values of the ratio are all much greater than 0.1, so that in these cases criterion D is always satisfied. However, for a given value of K and X, the minimum value of the surface site density, according to criterion C, is for $S = S_1$, and as shown in Figure 2.4b, the ratios $G_s(0)/G_a(0)$ for S_1 are not all greater than the allowed value of 0.1. This result sets a new minimum for the site density, denoted by S_3, which is determined by setting the expression for the ratio in Eq. 2.17 equal to 0.1 and solving for the value of S. The values of S_3 are

$$S_3 = \frac{d(1+X)^2}{20K} \tag{2.18}$$

The actual minimum site densities are thus equal to the maxima of S_1 and S_3 and are shown as the lower limits in the S ranges in Table 2.3.

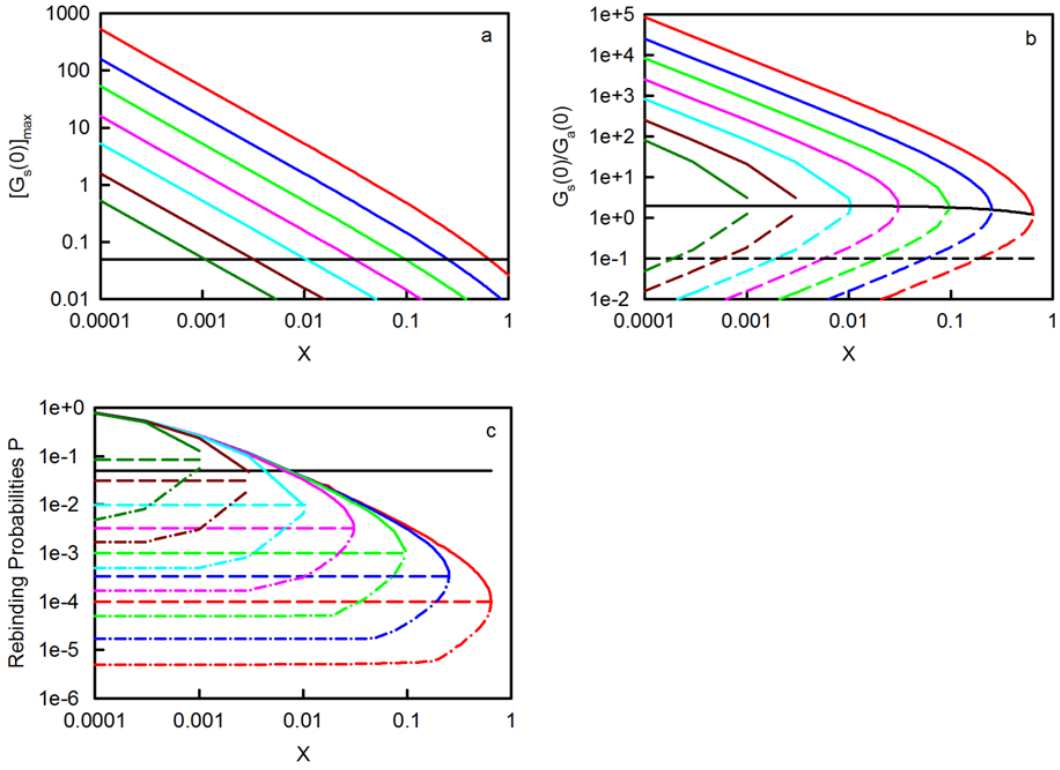

Figure 2.4: Conditions Required for TIR-FCS. In all panels, the colors denote (red) $K = 10^7$ M^{-1}; (blue) $K = 3 \times 10^6$ M^{-1}; (green) $K = 10^6$ M^{-1}; (pink) $K = 3 \times 10^5$ M^{-1}; (cyan) $K = 10^5$ M^{-1}; (dark red) $K = 3 \times 10^4$ M^{-1}; and (dark green) $K = 10^4$ M^{-1}. Panel (a) shows the values of $[G_s(0)]_{max}$ calculated from Eq. 2.14 and as a function of X. In these plots, $S = S_{max}$ (Eq. 2.13 and Table 2.3). The black line depicts the cutoff values of X for which $G_s(0) \leq 0.05$ and criterion C is not satisfied. Panel (b) shows the values of $G_s(0)/G_a(0)$ calculated from Eq. 2.17 and as a function of X. Solid, colored lines are for $S = S_2$ and dashed, colored lines are for $S = S_1$. The solid black line is for $S = S_{max}$ and does not depend on K. The dashed black line shows the cutoff value below which the ratio is unacceptable according to criterion D. Panel (c) shows P calculated by numerically integrating Eq. 2.19 with Eq. 2.20. The value of k_a is taken to equal 10^6 $M^{-1}s^{-1}$ and the values of S are (solid) S_2; (dash) S_{max}; and (dash-dot) the maximum of S_1 and S_3. The black line depicts the cut-off value for which $P \geq 0.05$ and criterion E is not satisfied.

Criterion E requires that rebinding to the surface after dissociation, within the observed area, is negligible. The purpose of this requirement is to ensure that Eqs. 2.6 and 2.11 are applicable, as their derivation depends on the assumption that the rates associated with rebinding are much lower than the intrinsic rates associated with the mechanism shown in Eq. 2.2 (*36*). As shown previously (*43*, *44*), the probability that a

molecule which dissociates from the origin at time zero has rebound at least once between positions r = 0 and r = h, and at time infinity, is

$$P = -\int_0^{\infty} dt \int_0^{2\pi} d\varphi \int_0^{h} dr \, \frac{r}{4\pi Dt} \exp(-\frac{r^2}{4Dt}) \frac{\partial}{\partial t} [\exp(\eta^2 t) erfc(\eta\sqrt{t})]$$
$$= \int_0^{\infty} dt \, [1 - \exp(-\frac{h^2}{4Dt})] \, [-\frac{\partial}{\partial t} \exp(\eta^2 t) erfc(\eta\sqrt{t})] \qquad (2.19)$$

In Eqs. 2.19, the parameter η describes the propensity for surface rebinding and is defined as

$$\eta = \frac{k_a S}{\sqrt{D}(1+X)} \qquad (2.20)$$

Rebinding is more likely when the surface site density is higher, when the surface binding sites are less occupied, when the association kinetic rate constant is higher, and when the diffusion coefficient in solution is small. When $h \rightarrow \infty$, the integral in Eq. 2.19 is (*45*)

$$[P]_{h\rightarrow\infty} = -\int_0^{\infty} dt \, [\frac{\partial}{\partial t} \exp(\eta^2 t) erfc(\eta\sqrt{t})] = [-\exp(\eta^2 t) erfc(\eta\sqrt{t})]_0^{\infty} = 1 \qquad (2.21)$$

A molecule which dissociates from an infinite plane always eventually rebinds somewhere on the surface. However, in the work described in this paper, h is small and the values of P are also (usually) small. Values of P as a function of X, with $k_a = 10^6$ $M^{-1}s^{-1}$ and S = S_2, S_{max}, or the maximum of S_1 and S_3, were calculated by numerically integrating the second expression in Eq. 2.19 with Eq. 2.20. As shown in Figure 2.4c, P is usually much less than the cutoff value of 0.05. Exceptions are found for higher values of S, and lower values of X and K. For a given X value, an upper limit for S, denoted by S_4, can be found numerically for P = 0.05. These values range from 3300 – 5400

molecules/μm^2. The true maximum site densities are equal to the minima of S_2 and S_4 and are shown as upper limits in the S ranges in Table 2.3. [For the lowest K, S_{max} is greater than the upper limit and, when $X=X_{max}$ (0.00106), the upper limit is less than the lower limit, and therefore no values of S meet all five criteria. These results set a new upper limit for X (9.65×10^{-4}).]

2.4.4 Measurement of K by TIR-FCS

A first question, given that criteria A-E are satisfied, is how one might go about measuring the equilibrium association constant K by using TIR-FCS rather than steady-state TIRFM. This type of measurement might be useful for a number of situations. One class of such situations includes *in vivo* cases in which the parameters cannot be precisely controlled or known (e.g., when one is interested in examining reversible association of fluorescent molecules in the cytosol with sites on the cytoplasmic face of adherent cells illuminated by evanescent excitation). Another class includes those in which one finds it not to be possible to make steady-state *in vitro* TIRFM measurements up to $A \approx 4/K$ (see above) because the required higher concentrations of fluorescent ligands with good purity are not obtainable within a reasonable amount of time and expense, or precipitate and/or oligomerize at high concentrations. Thus, we define below two methods in which K might be measured by using TIR-FCS.

First, it should be noted that measures of $F_{pos}(A)$ and $F_{neg}(A)$ (Eq. 2.12) will be a natural consequence of acquiring TIR-FCS data. No extraneous steady-state TIRFM data acquisition is required. Then, from the two measured quantities, one can calculate

$$\frac{F_{pos}(A) - F_{neg}(A)}{F_{neg}(A)} = \frac{KS}{d}\frac{1}{1+KA} = \frac{\rho}{1+KA} \tag{2.22}$$

where the dimensionless parameter ρ is

$$\rho = \frac{KS}{d} \tag{2.23}$$

The wide range of ρ values (0.05 to 550) for different values of K and X are shown in Table 2.3. Curve-fitting the measured values of Eq. 2.22 to the form on the right side, as a function of A, will give a best-fit value for ρ and, if high enough A values are accessible, also for K. If one chooses to assume an approximate value for d (*1*), then an approximate value for S can be found from ρ, K and d. Predicted data are illustrated in Figure 2.5a. As shown, this strategy for measuring K is more likely to be successful for higher K values. Because the accessible values of X are capped at very low values for smaller K (Table 2.3), in these cases Eq. 2.22 is approximately constant and equal to ρ. Thus, low K values are predicted to be measurable by this method only if the values of S and d are independently calibrated.

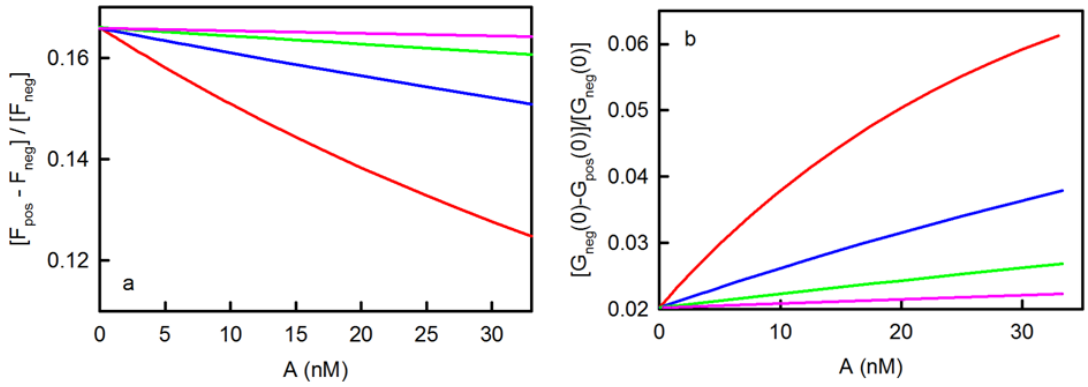

Figure 2.5: Measurement of K by using TIR-FCS. In both panels, the colors denote (red) K = 10^7 M^{-1}, (blue) K = 3 x 10^6 M^{-1}, (green) K = 10^6 M^{-1}, and (pink) K = 3 x 10^5 M^{-1}; surface site densities are (red) 1, (blue) 3.33, (green) 10, and (pink) 33.3 molecules/μm^2; and ρ = 0.166. Panel (a) shows the values of $[F_{pos}(A)-F_{neg}(A)]/F_{neg}(A)$ calculated from Eq. 2.22. The intercepts equal ρ. The initial slopes equal –ρK; their magnitudes increase with K. These slopes are indicative of the ability of the proposed strategy to measure K. Panel (b) shows the values of $[G_{neg}(0)-G_{pos}(0)]/[G_{neg}(0)]$ calculated from Eq. 2.25. The intercepts equal $[\rho/(1+\rho)]^2$. The initial slopes are $2K\rho/(1+\rho)^3$ and increase with K.

Because measuring equilibrium association constants by using only values of A that are less than K^{-1} is vulnerable to potential artifacts, it is desirable to confirm the measured K value by using the information contained in the magnitudes of the acquired $G(\tau)$. There are two directly measurable quantities, G(0) in the presence and absence of surface binding sites, denoted as $G_{pos}(0)$ and $G_{neg}(0)$, respectively. Referring to Eqs. 2.6 and 2.9, one finds that

$$G_{pos}(0) = \frac{2KS + d(1+KA)^2}{2\pi h^2 A[KS + d(1+KA)]^2}$$
$$G_{neg}(0) = \frac{1}{2\pi h^2 dA} \tag{2.24}$$

To accurately measure these quantities, it may be necessary to account for photophysical effects that can occur at high excitation intensities and low time lags τ (*27*, *28*). This correction is necessary only if the excitation intensity is high enough so that the measured $G(\tau)$ are dependent on it. In addition, the G(0) values must be extrapolated from $G(\tau)$ at low τ because when $\tau = 0$ the autocorrelation functions contain contributions from shot noise. In analogy to Eq. 2.22, the following function can be defined:

$$\frac{[G_{neg}(0) - G_{pos}(0)]}{G_{neg}(0)} = \frac{KS[KS + 2dKA]}{[KS + d(1+KA)]^2} = \frac{\rho(\rho + 2KA)}{(1+\rho+KA)^2} \tag{2.25}$$

Eq. 2.25 is positive because $G_{neg}(0) > G_{pos}(0)$. This at first counter-intuitive result is because, when comparing $G_{neg}(0)$ to $G_{pos}(0)$ for a given A value, there are fewer fluorescent molecules in the observed volume due to the lack of surface binding sites, and fewer fluorescent molecules in general translates into higher magnitudes for fluorescent fluctuation autocorrelation functions. Figure 2.5b shows the expected values of Eq. 2.25 as a function of K, A and set values of S. Curve-fitting the measured values of Eq. 2.25

to the form on the right side, as a function of A, will return best-fit values of ρ and, if high enough values of A are accessible, K.

2.4.5 Measurement of k_d, or k_d and k_a, by TIR-FCS

One way to measure k_d is by using evanescent illumination with fluorescence recovery after photobleaching (*37, 38, 40, 46, 47*). However, this method cannot directly report the value of k_a, which would need to be inferred from a previously measured value of K and the measured value of k_d (Eq. 2.3). TIR-FCS does not have this strict feature of reporting only k_d and not k_a; both rate constants are present in the theoretically predicted form for $G(\tau)$ (Eq. 2.11).

The above discussion defines conditions, as illustrated in Figures 2.4a-c and summarized in Table 2.3, for which criteria A, B, C, D and E (Table 2.2) are met, given assumed values of d, h, D and k_a (Table 1.2). Thus, for the conditions summarized in Table 2.3, we conclude that it is reasonable to expect that the rate associated with the exponential decay of $G_s(\tau)$ (Eq. 2.11) can be measured with sufficient accuracy. This rate equals $k_d + k_aA$ and ranges from a minimum of k_d to infinity as the concentration of fluorescent molecules in solution, A, is increased. Plotting the measured rate vs. A and fitting to a line will in general yield an intercept of k_d and a slope of k_a.

The relaxation rate will increase fast enough with A for k_a to be directly measurable only if higher values of A are accessible. However, as shown in Table 2.3, it is the higher rather than lower values of A = X/K that limit the range of applicability. Rewriting the relaxation rate as $k_d(1+ X)$ shows that the measurable rate will increase only by a percentage determined by X. In particular, the prediction is that the measured relaxation rate will exceed k_d only by ≈ 65% for $K = 10^7\ M^{-1}$; by ≈ 25% for $K = 3 \times 10^6$

$M^{-1}s^{-1}$; and by less than 10% for $K = 10^6 – 10^4\ M^{-1}$. Thus, for low K values TIR-FCS will yield a measure of k_d, but not k_a. Subsequently, k_a can be inferred from the measured values of K and k_d (Eq. 2.3) in which K is measured either with steady-state TIRFM, TIR-FCS or with another method.

For higher values of K, k_a will be directly measurable by TIR-FCS. First, for $K = 10^7\ M^{-1}$, the relaxation rate is expected to be measurable through a range of k_d to 1.6 k_d and, given the accuracy of current FCS apparatuses, this range will most likely be wide enough for a direct measure of k_a. This optimal case is illustrated in Figures 2.6a-c. Figure 2.6a shows the predicted values of $G(\tau)$ as a function of τ, for four values of X and other defined experimental conditions. What is immediately obvious from this plot is that the main effect of increasing the solution concentration of fluorescent molecules is that G(0) is dramatically decreased. Figure 2.6b shows the predicted values of $G(\tau)/G(0)$ as a function of τ, for the same four values of X and the same other presumed experimental conditions. This plot shows that, when one changes A (and therefore X), the primary effect is that the fractional contributions to $G(\tau)$ arising from $G_s(\tau)$ and $G_a(\tau)$ change (Eq. 2.17); as expected, the contribution from $G_s(\tau)$ relative to that from $G_a(\tau)$ decreases with increasing X. This feature is a consequence of two effects (Eq. 2.5 and 2.7). As X is increased, both N_C/N_A and N_B/N decrease as $(1+X)^{-1}$. Figure 2.6c shows $G_s(\tau)/G_s(0)$ for the four chosen values of X. As shown, the decay rate increases with increasing concentrations of fluorescent reporter molecules. The case of $K = 3 \times 10^6\ M^{-1}$ is illustrated in Figures 2.6d-f. The same features are present, except that $G_s(\tau)/G_s(0)$ changes only slightly with X. Thus, accurate measurement of k_a will be possible only for experimental situations in which both K and the signal-to-noise ratio of $G(\tau)$ are high.

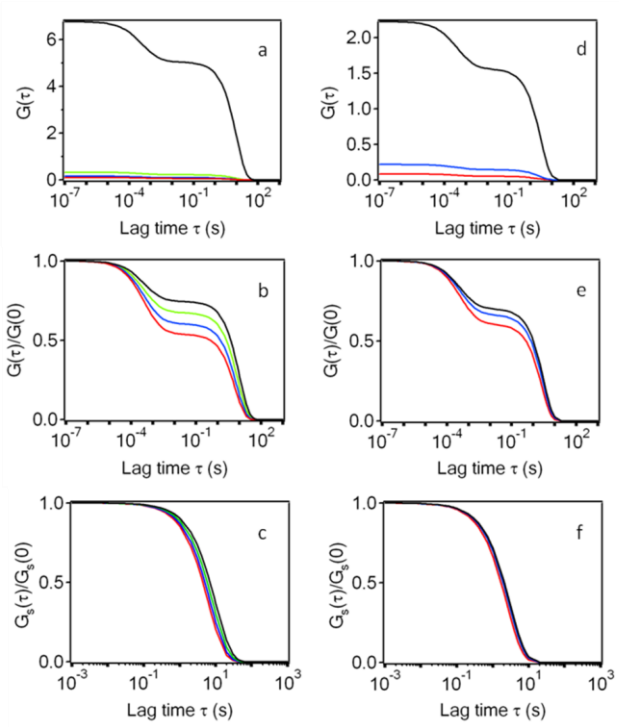

Figure 2.6: Measurement of kd, or kd and ka, by TIR-FCS. Panels (a) and (d) show G(τ) calculated from Eqs. 2.6 and 2.9-2.11. Panels (b) and (e) show G(τ)/G(0). Panels (c) and (f) show $G_s(\tau)/G_s(0)$. In all cases, D = 50 $\mu m^2 s^{-1}$, d = 0.1 μm, and h = 0.5 μm. In (a-c), K = 10^7 M^{-1}, k_d = 0.1 s^{-1}, S= 9 molecules/μm^2 and X is (red) 0.6, (blue) 0.4, (green) 0.2 or (black) 0.01. In (d-f), K = 3 x 10^6 M^{-1}, k_d = 0.33 s^{-1}, S= 24 molecules/μm^2 and X is (red) 0.25, (blue) 0.1, or (black) 0.01.

2.5 Discussion

2.5.1 Summary of Results

Conditions for which TIR-FCS measurements aimed at quantifying the thermodynamic and kinetic parameters associated with a simple, reversible association of fluorescent ligands with immobilized, non-fluorescent surface binding sites have been defined in detail, for assumed values of the solution diffusion coefficient D (50 $\mu m^2 s^{-1}$), the evanescent wave depth d (0.1 μm), the radius of the observed area h (0.5 μm) and for a (usually) assumed value of the association rate constant k_a (10^6 $M^{-1}s^{-1}$) (Table 2.1). The conditions are defined by five criteria as described in Table 2.2. Only values of the

solution concentration of fluorescent molecules A which are greater than or equal to $10^{-4}/K$, where K is the equilibrium constant, were considered.

Meeting the criteria gave the following results, as shown in Table 2.3 and Figure 2.4: 1) K is limited to the range $10^4 - 10^7$ M^{-1}. 2) For a given K, there is a maximum allowed value of A. These maximum values range from 64-100 nM and correspond to lower values of the product $X = KA$ with decreasing K. For $K = 10^7$ M^{-1}, the maximum value of X is 0.643 and for $K = 10^4$ M^{-1}, the maximum value of X is 10^{-3}. 3) Ranges of allowed total surface site densities, S, exist for given values of K and A. 4) $G_s(\tau)$, the quantity of interest, is maximized at a defined surface site density for given K and X values.

As illustrated in Figure 2.3, the most straightforward method of measuring K is to use steady-state TIRFM. However, this method is expected to be successful only for higher values of K and S. Measuring the lowest value of K (10^4 M^{-1}) is expected to be possible only if a total surface site density $\geq$ 12,000 molecules/μm^2 can be experimentally generated. At the highest limit of $K = 10^7$ M^{-1}, only very low total surface site densities, $\geq$ 12 molecules/μm^2, are predicted to be required. In addition, high A values must be experimentally accessible.

Two alternative methods for measuring K with TIR-FCS were also described. The first method uses the average fluorescence intensities in the presence and absence of binding sites, which will be found as a natural consequence of TIR-FCS measurements (Figure 2.5a). The second method uses G(0) values in the presence and absence of binding sites (Figure 2.5b). These methods are most likely to be successful either for high K or when S and d are independently calibrated.

It is desirable, in general, to independently measure all three parameters (K, k_a, and k_d) governing the mechanism shown in Eq. 2.2 and Figure 2.2 and to confirm their consistency (Eq. 2.3). However, as described in the text, both k_a and k_d are expected to be measurable only for higher K values (Figure 2.6). For lower values of K, TIR-FCS will yield only a measure of k_d. In these cases, k_a can be inferred from measured values of K and k_d.

2.5.2 Comparison with Experimental Results

Of interest is the comparison of the theoretical predictions described here with previously obtained experimental TIR-FCS data. The earliest attempt at characterizing surface binding kinetics by using TIR-FCS was carried out for the nonspecific, reversible interaction of fluorescently labeled IgG with albumin-coated surfaces (*21*). G(0) values were lower than those considered here (about 0.02) but were dominated by contributions from surface kinetics in that $G_s(0)/G_a(0)$ was greater than 10. However, the characteristic time for the decay of $G(\tau)$ was fast (several ms), and theoretical considerations suggested that the autocorrelation functions were dominated by contributions from surface rebinding. Fitting the data to a form that accounted for this probable effect gave $k_d = (0.4 \text{ ms})^{-1}$. This first work demonstrated the feasibility of TIR-FCS and provided a basis for future development.

In a subsequent work, extrapolated G(0) values from TIR-FCS measurements were used to measure equilibrium association constants for rhodamine 6G with C-18 derivatized fused silica, with the intent of better understanding reversed-phase chromatography (*22*). Measurements were carried out for a range of water/methanol solutions and NaCl concentrations. The measured K values were very low, ranging from

≈ 3 to $\approx 20{,}000$ M^{-1}. That such weak equilibrium association constants were measured is at first seemingly inconsistent with the results shown in Figure 2.5 and described in the associated text. One difference is that the probe concentrations were very low (50 pM – 1 nM) so that the values of X were much lower than those considered here (Table 2.3). Thus, the measured K values were obtained very far from the midpoint of the binding isotherm and must be taken as apparent K applicable to very low solution concentrations. However, the primary reason that such low K values were measurable (and with good accuracy) is not the low probe concentrations. The reason appears to be that a much different method than the ones considered here was used. The method incorporated direct calibration of Q (Eqs. 2.12) and the observation volume. In addition, the method did not use only the normalized fluorescence fluctuation autocorrelation function (Eq. 2.1) but instead used both the measured numerator extrapolated to $\tau = 0$, $\langle \delta F^2 \rangle$, and the measured average fluorescence, $\langle F \rangle$, as independent quantities.

In a very elegant companion study, the kinetics of rhodamine 6G reversibly associating with C-18 derivatized fused silica were examined (*23*). These measurements were also carried out for conditions of very low K (≈ 3 to 2000 M^{-1}) and A (50 pM – 1 nM). A number of features of this work are noteworthy. First, $G(\tau)$ were analyzed by using a more complex expression previously derived (*36, 37*) which includes contributions arising from a rate related to surface rebinding (*43, 44*), and these contributions were not negligible. Second, in most cases, G(0) was much lower than considered in this work ($\approx 5 \times 10^{-4}$ to 5×10^{-3}). Nonetheless, by estimating the rates associated with diffusion through the evanescent wave and with rebinding and fixing these rates before curve-fitting, values of the relaxation rate $k_a A + k_d$ were measured.

Not surprisingly, because the X values were so low, this rate was dominated by k_d, which ranged from ≈ 40 to 4000 s^{-1}. Previously measured values of K were then used to calculate k_a, which ranged from ≈ 10^4 to 10^5 $M^{-1}s^{-1}$. In comparison to the results described herein, this work highlights the fact that the criteria defined in Table 2.2 are more restrictive than is necessary. We have adopted the more restrictive criteria because of the goal of using a single fluorescent reporter to measure the thermodynamic and/or kinetic parameters associated with non-fluorescent species involved in more complex surface binding mechanisms (see below).

In a somewhat similar set of measurements, the kinetics of fluorescently labeled polyamidoamine dendrimers (with different sizes) at fused silica surfaces were characterized by using TIR-FCS (*16*). Equilibrium constants were found from G(0) values along with other calibrations, and ranged from 5 x 10^4 to 2 x 10^6 M^{-1}. The solution concentrations were very low, corresponding to much lower values of X than those considered here; the G(0) values were very low; and the surface site densities were also higher than the maximum values shown in Table 2.3. The low X values are predicted to preclude direct measurement of k_a, and this prediction was in fact observed. The high surface site densities should in theory result in significant rebinding, removing the ability of TIR-FCS to measure k_d. However, significant flow was included in this work, removing complications from rebinding, and values of k_d ranging from 6 to 70 s^{-1} were measured. Association rate constants k_a were inferred from the measured values of K and k_d and ranged from 3 x 10^6 to 10^7 $M^{-1}s^{-1}$. Overall, the experimental results described in this work are consistent with our theoretical predictions. The results also

provide a direct demonstration that flow can remove constraints arising from rebinding and that it is possible to work at very low G(0) values given adequate instrumentation.

The first use of TIR-FCS to examine the kinetics of the reversible association of fluorescent ligands with specific, molecular surface binding sites was carried out for fluorescently labeled IgG reversibly associating with the mouse Fc receptor FcγRII reconstituted into planar phospholipid bilayers formed on fused silica surfaces (*25*). There is a difficulty in comparing the results with those described herein because a tracer amount of labeled IgG was combined with a large excess of unlabelled IgG so that the total ligand concentration was close to the mid-point of the binding isotherm. The effects of the presence of the non-fluorescent competitors on TIR-FCS data have been formally defined (*35*) but have not yet been fully explored theoretically in a manner comparable to the work described here. Nonetheless, the data conformed in a general manner with theoretical expectations (*25*).

TIR-FCS has recently been used to examine the kinetics of fluorescently labeled bovine serum albumin and *Thermomyces lanuginosus* lipase with C_{18}-coated glass in the presence of surfactants (*24*). Again, it is difficult to compare the results reported in this work with the ones described herein, for several reasons. First, the surfactants can act as inhibitors of surface adsorption both by competitively occupying surface binding sites and by directly interacting with the proteins in solution. Also, in several of the measurements, free dye was present in addition to labeled proteins, photobleaching of tightly bound proteins was observed, the excitation intensities were high enough to produce photophysical effects at short times in the $G(\tau)$, and the systems were not at equilibrium. Nonetheless, this work provides a good deal of useful information about

carrying out TIR-FCS when competitors are present (as well as providing information about the protein adsorption process itself) and highlights the need for a more thorough theoretical understanding of how TIR-FCS might be used to examine surface binding kinetics for mechanisms more complex than a simple, reversible association between fluorescent ligands in solution and non-fluorescent surface binding sites.

Enzyme kinetics at surfaces have also been investigated by using TIR-FCS (*26*). In these measurements, the reduction of dihydrorhodamine 123 to the highly fluorescent rhodamine 123, as catalyzed by immobilized horseradish peroxidase (HRP), was followed. Single enzymes were located by using a CCD camera, and time-dependent fluorescence intensity data were obtained using a single-photon counting silicon avalanche photodiode. The autocorrelated fluorescence data were fit to a phenomenological expression for $G(\tau)$ which contained a term describing the diffusion of fluorophores through the observation volume and two terms describing the enzyme kinetics. For the last two terms, the multi-step enzyme mechanism was approximated as a unimolecular isomerization; one term was a stretched exponential with rate k_1 describing formation of the fluorescent enzyme-product complex and the other term was a simple exponential with rate k_2 describing all other steps in the mechanism. The total concentration of dihydrorhodamine 123 was $\approx$ 100-500 nM and the density of immobilized enzymes was 0.1 per μm^2. The value of R_z was measured in regions not containing enzymes and was found to be $(18\ \mu s)^{-1}$, which is somewhat higher than theory predicts even for fast rhodamine diffusion, but not completely unreasonable. A result that is inconsistent with theoretical predictions was the measured G(0) values, which were higher in the presence relative to the absence of enzyme. This inconsistency may be

a simple consequence that the work shows only representative $G(\tau)$ and not averages of $G(0)$ from many positions. The ratios of $G_s(0)$ to $G_a(0)$ were greater than one, more than adequate for measuring surface kinetics, and the values of $G(0)$ were quite high enough (0.2-0.4) for good signal-to-noise ratios. The measured values of k_2 were $\approx 1000\ s^{-1}$ and the measured values of k_1 were $\approx 15000\ s^{-1}$. Particularly the k_1 values do not comply with our criterion B, which may explain the somewhat fast measured value of R_z. Nonetheless, this work is seminal in that it demonstrates the ability of TIR-FCS to probe enzyme kinetics. The work also indicates that further work describing the nature of TIR-FCS kinetic data for different enzyme mechanisms is needed.

A series of three papers demonstrates the ability of TIR-FCS to probe the partitioning of fluorescent biomolecules between the cytoplasm and the inner face of the basal plasma membrane of adherent cells. In the first work, membrane binding of farnesylated EGFP in HeLa cells was examined (*7*). Autocorrelation data were analyzed with a model accounting for fast diffusion in solution coupled with slower diffusion on the membrane. The fractions of the magnitudes of the measured $G(\tau)$ associated with solution and membrane diffusion were found to be 0.72 and 0.28, respectively; and the times R_r^{-1} associated with these fractions were 3.3 and 65 ms, respectively. In a similar work, membrane binding of EGFP-conjugated protein kinase C in HeLa cells was examined (*8*). The fractions of $G(\tau)$ associated with solution and membrane diffusion, and the associated times R_r^{-1}, were 2.5 ms (0.82) and 160 ms (0.18). After treatment with ATP, these parameters changed to 4.4 ms (0.69) and 140 ms (0.31), suggesting an ATP-induced shift towards membrane binding. The most important conclusion to be derived from these studies is that TIR-FCS can be successful in living cells. In the third paper,

the work was extended by using seven different spatially separated observation volumes, each having its own photomuliplier as a detector (*29*). This study represents a first step towards creating a kinetic map of intracellular dynamics occurring on or near basal cell membranes.

There is an important feature related to the application of TIR-FCS to live cells that becomes apparent when considering the results of these three studies in relation to the work described herein. Possible contributions to $G(\tau)$ arising from association/dissociation kinetics at the cell membrane were not considered. In its simplest form, TIR-FCS can provide information about association and dissociation kinetics only if the times related to these processes are faster than the times for diffusion on the surface through the observed area. Because this area is usually required to be small to limit the average number of fluorescent molecules in the observation volume, obtaining information about on/off kinetics will be possible only if the membrane diffusion coefficient is slow enough and only through careful analysis as a function of the size of the observed area, to separate contributions from lateral mobility and surface binding kinetics. In the work described above, the membrane diffusion coefficients were on the order of 10^{-9} cm^2s^{-1} and the associated transport times were $\approx$ 150 ms; thus, only kinetic processes on the order of or faster than this time would be detectable. However, in many cases, apparent membrane diffusion coefficients could be much slower, making measurement of dissociation rates and/or association kinetic rate constants more tractable.

An extensive study of paxillin dynamics in focal adhesions of migratory cells has recently been reported (*30*). This work examined the behavior of EGFP-conjugated,

cytosolic paxillin in adherent CHO cells by using a large variety of state-of-the art fluorescence microscopy methods. Of the many methods employed, one was TIR-FCS coupled not with a single-point detector but with a fast imaging camera. This approach allows calculation of $G(\tau)$ from very many positions by auto-correlating the fluorescence fluctuations from single pixels (*33*). In the paxillin study, because the frame acquisition rate was ≈ 100 Hz, temporal contributions to the $G(\tau)$ from diffusion of the labeled paxillin through the depth of the evanescent wave were largely excluded. The $G(\tau)$ were fit to exponential decays (Eq. 2.11), yielding exchange rates that varied with position from 0.1 s^{-1} to 10 s^{-1}. By combining these results with those found from a number of other methods, considerable information about the role of paxillin in migratory cells was obtained. This work demonstrates that imaging TIR-FCS is extremely promising in the context of creating "kinetic maps" for fluorescently labeled molecules reversibly associating with the inner face of the plasma membrane of adherent cells and correlating the observed kinetics with other molecular details of the plasma membrane.

2.5.3 Expanded Range

Upon review of the available experimental data, it becomes apparent that TIR-FCS has been successfully carried for conditions that do not conform to our criteria (Table 2.2). The most glaring discrepancy is in our definition of the minimum allowable value of $G_s(0)$. Therefore, we relaxed Criterion C and carried out calculations in which the minimum value of $G_s(0)$ is not 0.05 but can also be 0.01, 0.005 or 0.001. Tables 2.4 – 2.7 show calculated quantities for the four considered values of $[G_s(0)]_{min}$, six considered values of K, and X = 0.0001 or X = X_{max}. Table 2.4 shows S_1, S_2, S_3, S_4, S_{max} and the S

range. Tables 2.5, 2.6 and 2.7 show predicted values of $G_s(0)$, $G_s(0)/G_a(0)$, and P, respectively, for the five surface site densities and the S range.

S_{max} values denote the surface site densities for which $G_s(0)$ is maximized; depend on d, X and K; and were calculated from Eq. 2.13. The S_{max} values give an expression for the maximum value of $G_s(0)$ which also depends on d, X and K (Eq. 2.14). By setting this expression equal to $[G_s(0)]_{min}$, one finds a maximum value of X, denoted by X_{max}, which equals

$$X_{max} = \frac{1}{2}[-1+\sqrt{1+\frac{K}{\pi h^2 d[G_s(0)]_{min}}}]. \qquad (2.26)$$

In Tables 2.4 – 2.7, for a given value of K and $[G_s(0)]_{min}$, the minimum value of X considered was 0.0001 and the maximum value of X was calculated from the above equation. Surface site densities S_1 and S_2 denote the minimum and maximum values for which $G_s(0) \geq [G_s(0)]_{min}$, depend on K, X, d and h, and were calculated from the following generalization of Eq. 16:

$$S_{1,2} = \frac{K - 2\pi h^2 dX(1+X)[G_s(0)]_{min} \mp \sqrt{K^2 - 4\pi h^2 dKX(1+X)[G_s(0)]_{min}}}{2\pi h^2 KX[G_s(0)]_{min}} \qquad (2.27)$$

Surface site densities S_3 denote values below which $G_s(0)/G_a(0)$ exceeds 0.1, depend on d, X and K, and were calculated from Eq. 2.18. Surface site densities S_4 denote values above which $P \geq 0.05$, depend on S and X, and were found by numerically integrating Eq. 2.19 with Eq. 2.20. The range of allowable surface site densities was calculated as the maximum of S_1 and S_3 to the minimum of S_2 and S_4. This range reflects the constraints that $G_s(0) \geq [G_s(0)]_{min}$, $[G_s(0)/G_a(0)] \geq 0.1$, and $P \leq 0.05$, and is not meant as an absolute requirement for successful TIR-FCS measurements. Using surface site densities outside of this range will have the consequence of violating one of these three constraints and the

violation of these constraints may require analysis with a more sophisticated model than that shown in Eqs. 2.6 and 2.9-2.11.

Table 2.4: Surface Site Densities for Lower Values of $G_s(0)$

$[G_s(0)]_{min}$	K	X	A	S_1	S_2	S_3	S_4	S_{max}	S range
0.05	10^7	0.0001	0.01	1.4×10^{-4}	2.5×10^5	0.30	3300	6.0	0.30-3300
		0.643	64.3	9.9	9.9	0.81	5400	9.9	9.9
	3×10^6	0.0001	0.0333	0.0016	2.5×10^5	1.0	3300	20	1.0-3300
		0.253	84.3	25	25	1.6	4100	25	25
	10^6	0.0001	0.1	0.014	2.5×10^5	3.0	3300	60	3.0-3300
		0.0964	96.4	66	66	3.6	3600	66	66
	3×10^5	0.0001	0.333	0.16	2.5×10^5	10	3300	200	10-3300
		0.0308	103	210	210	11	3400	210	210
	10^5	0.0001	1	1.4	2.5×10^5	30	3300	600	30-3300
		0.0105	105	610	610	31	3300	610	610
	3×10^4	0.0001	3.33	16	2.5×10^5	100	3300	2000	100-3300
		0.00316	105	2000	2000	100	3300	2000	2000
0.01	10^7	0.0001	0.01	2.9×10^{-5}	1.3×10^6	0.30	3300	6.0	0.30-3300
		1.85	185	17	17	2.4	9400	17	17
	3×10^6	0.0001	0.0333	3.2×10^{-4}	1.3×10^6	1.0	3300	20	1.0-3300
		0.855	285	37	37	3.5	6100	37	37
	10^6	0.0001	0.1	0.0029	1.3×10^6	3.0	3300	60	3.0-3300
		0.382	382	83	83	5.8	4500	83	83
	3×10^5	0.0001	0.333	0.032	1.3×10^6	10	3300	200	10-3300
		0.139	463	230	230	13	3700	230	230
	10^5	0.0001	1	0.29	1.3×10^6	30	3300	600	30-3300
		0.0503	503	630	630	33	3400	630	630
	3×10^4	0.0001	3.33	3.2	1.3×10^6	100	3300	2000	100-3300
		0.0156	520	2000	2000	100	3300	2000	2000
0.005	10^7	0.0001	0.01	1.4×10^{-5}	2.5×10^6	0.30	3300	6.0	0.30-3300
		2.79	279	23	23	4.3	12500	23	23
	3×10^6	0.0001	0.0333	1.6×10^{-4}	2.5×10^6	1.0	3300	20	1.0-3300
		1.35	450	47	47	5.5	7700	47	47
	10^6	0.0001	0.1	0.0014	2.5×10^6	3.0	3300	60	3.0-3300
		0.643	643	99	99	8.1	5400	99	99
	3×10^5	0.0001	0.333	0.016	2.5×10^6	10	3300	200	10-3300
		0.253	843	250	250	16	4100	250	250
	10^5	0.0001	1	0.14	2.5×10^6	30	3300	600	30-3300
		0.0964	964	660	660	36	3600	660	660
	3×10^4	0.0001	3.33	1.6	2.5×10^6	100	3300	2000	100-3300
		0.0308	1030	2100	2100	110	3400	2100	2100
0.001	10^7	0.0001	0.01	2.9×10^{-6}	1.3×10^7	0.30	3300	6.0	0.30-3300
		6.79	679	47	47	18	25000	47	47
	3×10^6	0.0001	0.0333	3.2×10^{-5}	1.3×10^7	1.0	3300	20	1.0-3300
		3.51	1170	91	91	20	15000	91	91
	10^6	0.0001	0.1	2.9×10^{-4}	1.3×10^7	3.0	3300	60	3.0-3300
		1.85	1850	170	170	24	9400	170	170
	3×10^5	0.0001	0.333	0.0032	1.3×10^7	10	3300	200	10-3300
		0.854	2840	370	370	35	6100	370	370
	10^5	0.0001	1	0.029	1.3×10^7	30	3300	600	30-3300
		0.382	3820	830	830	58	4500	830	830
	3×10^4	0.0001	3.33	0.32	1.3×10^7	100	3300	2000	100-3300
		0.139	4630	2300	2300	130	3700	2300	2300

Table 2.5: $G_s(0)$ Values for Different Surface Site Densities

$[G_s(0)]_{min}$	K	X	$G_s(0)$					
			S_1	S_2	S_3	S_4	S_{max}	S range
0.05	10^7	0.0001	0.05	0.05	95	3.8	530	3.8-95
		0.643	0.05	0.05	0.014	3.7×10^{-4}	0.05	0.05
	3×10^6	0.0001	0.05	0.05	29	3.8	160	3.8-29
		0.253	0.05	0.05	0.011	0.0012	0.05	0.05
	10^6	0.0001	0.05	0.05	9.5	3.7	53	3.7-9.5
		0.0964	0.05	0.05	0.0099	0.0035	0.05	0.05
	3×10^5	0.0001	0.05	0.05	2.9	3.4	16	2.9-3.4
		0.0308	0.05	0.05	0.0093	0.011	0.05	0.05
	10^5	0.0001	0.05	0.05	0.95	2.8	5.3	0.95-2.8
		0.0105	0.05	0.05	0.0092	0.026	0.05	0.05
	3×10^4	0.0001	0.05	0.05	0.29	1.5	1.6	0.29-1.5
		0.00316	0.05	0.05	0.0091	0.047	0.05	0.05
0.01	10^7	0.0001	0.01	0.01	95	3.8	530	3.8-95
		1.85	0.01	0.01	0.0044	7.3×10^{-5}	0.01	0.01
	3×10^6	0.0001	0.01	0.01	29	3.8	160	3.8-29
		0.855	0.01	0.01	0.0031	2.4×10^{-4}	0.01	0.01
	10^6	0.0001	0.01	0.01	9.5	3.7	53	3.7-9.5
		0.382	0.01	0.01	0.0024	7.1×10^{-4}	0.01	0.01
	3×10^5	0.0001	0.01	0.01	2.9	3.4	16	2.9-3.4
		0.139	0.01	0.01	0.0020	0.0022	0.01	0.01
	10^5	0.0001	0.01	0.01	0.95	2.8	5.3	0.95-2.8
		0.0503	0.01	0.01	0.0019	0.0053	0.01	0.01
	3×10^4	0.0001	0.01	0.01	0.29	1.5	1.6	0.29-1.5
		0.0156	0.01	0.01	0.0018	0.0095	0.01	0.01
0.005	10^7	0.0001	0.005	0.005	95	3.8	530	3.8-95
		2.79	0.005	0.005	0.0027	3.7×10^{-5}	0.005	0.005
	3×10^6	0.0001	0.005	0.005	29	3.8	160	3.8-29
		1.35	0.005	0.005	0.0019	1.2×10^{-4}	0.005	0.005
	10^6	0.0001	0.005	0.005	9.5	3.7	53	3.7-9.5
		0.643	0.005	0.005	0.0014	3.5×10^{-4}	0.005	0.005
	3×10^5	0.0001	0.005	0.005	2.9	3.4	16	2.9-3.4
		0.253	0.005	0.005	0.0011	0.0011	0.005	0.005
	10^5	0.0001	0.005	0.005	0.95	2.8	5.3	0.95-2.8
		0.0964	0.005	0.005	9.9×10^{-4}	0.0026	0.005	0.005
	3×10^4	0.0001	0.005	0.005	0.29	1.5	1.6	0.29-1.5
		0.0308	0.005	0.005	9.3×10^{-4}	0.0047	0.005	0.005
0.001	10^7	0.0001	0.001	0.001	95	3.8	530	3.8-95
		6.79	0.001	0.001	8.1×10^{-4}	7.5×10^{-6}	0.001	0.001
	3×10^6	0.0001	0.001	0.001	29	3.8	160	3.8-29
		3.51	0.001	0.001	6.0×10^{-4}	2.4×10^{-5}	0.001	0.001
	10^6	0.0001	0.001	0.001	9.5	3.7	53	3.7-9.5
		1.85	0.001	0.001	4.4×10^{-4}	7.1×10^{-5}	0.001	0.001
	3×10^5	0.0001	0.001	0.001	2.9	3.4	16	2.9-3.4
		0.854	0.001	0.001	3.1×10^{-4}	3.2×10^{-4}	0.001	0.001
	10^5	0.0001	0.001	0.001	0.95	2.8	5.3	0.95-2.8
		0.382	0.001	0.001	2.4×10^{-4}	5.3×10^{-4}	0.001	0.001
	3×10^4	0.0001	0.001	0.001	0.29	1.5	1.6	0.29-1.5
		0.139	0.001	0.001	2.0×10^{-4}	9.5×10^{-4}	0.001	0.001

Table 2.6: $G_s(0)/G_a(0)$ Values for Different Surface Site Densities

$[G_s(0)]_{min}$	K	X	$G_s(0)/G_a(0)$					
			S_1	S_2	S_3	S_4	S_{max}	S range
0.05	10^7	0.0001	4.7×10^{-5}	8.5×10^4	0.1	1100	2.0	0.1-1100
		0.643	1.2	1.2	0.1	660	1.2	1.2
	3×10^6	0.0001	1.6×10^{-4}	2.5×10^4	0.1	330	2.0	0.1-330
		0.253	1.6	1.6	0.1	260	1.6	1.6
	10^6	0.0001	4.7×10^{-4}	8500	0.1	110	2.0	0.1-110
		0.0964	1.8	1.8	0.1	99	1.8	1.8
	3×10^5	0.0001	0.0016	2500	0.1	33	2.0	0.1-33
		0.0308	1.9	1.9	0.1	32	1.9	1.9
	10^5	0.0001	0.0048	840	0.1	11	2.0	0.1-11
		0.0105	2.0	2.0	0.1	11	2.0	2.0
	3×10^4	0.0001	0.016	250	0.1	3.3	2.0	0.1-3.3
		0.00316	2.0	2.0	0.1	3.3	2.0	2.0
0.01	10^7	0.0001	9.5×10^{-6}	4.2×10^5	0.1	1100	2.0	0.1-1100
		1.85	0.70	0.70	0.1	380	0.70	0.70
	3×10^6	0.0001	3.2×10^{-5}	1.3×10^5	0.1	330	2.0	0.1-330
		0.855	1.1	1.1	0.1	180	1.1	1.1
	10^6	0.0001	9.5×10^{-5}	4.2×10^4	0.1	110	2.0	0.1-110
		0.382	1.5	1.5	0.1	78	1.5	1.5
	3×10^5	0.0001	3.2×10^{-4}	1.3×10^4	0.1	33	2.0	0.1-33
		0.139	1.8	1.8	0.1	28	1.8	1.8
	10^5	0.0001	9.5×10^{-4}	4200	0.1	11	2.0	0.1-11
		0.0503	1.9	1.9	0.1	10	1.9	1.9
	3×10^4	0.0001	0.0032	1300	0.1	3.3	2.0	0.1-3.3
		0.0156	2.0	2.0	0.1	3.2	2.0	2.0
0.005	10^7	0.0001	4.7×10^{-6}	8.5×10^5	0.1	1100	2.0	0.1-1100
		2.79	0.53	0.53	0.1	290	0.53	0.53
	3×10^6	0.0001	1.6×10^{-5}	2.5×10^5	0.1	330	2.0	0.1-330
		1.35	0.86	0.86	0.1	140	0.86	0.86
	10^6	0.0001	4.7×10^{-5}	8.5×10^4	0.1	110	2.0	0.1-110
		0.643	1.2	1.2	0.1	66	1.2	1.2
	3×10^5	0.0001	1.6×10^{-4}	2.5×10^4	0.1	33	2.0	0.1-33
		0.253	1.6	1.6	0.1	26	1.6	1.6
	10^5	0.0001	4.7×10^{-4}	8500	0.1	11	2.0	0.1-11
		0.0964	1.8	1.8	0.1	9.9	1.8	1.8
	3×10^4	0.0001	0.0016	2500	0.1	3.3	2.0	0.1-3.3
		0.0308	1.9	1.9	0.1	3.2	1.9	1.9
0.001	10^7	0.0001	9.5×10^{-7}	4.2×10^6	0.1	1100	2.0	0.1-1100
		6.79	0.26	0.26	0.1	140	0.26	0.26
	3×10^6	0.0001	3.2×10^{-6}	1.3×10^6	0.1	330	2.0	0.1-330
		3.51	0.44	0.44	0.1	73	0.44	0.44
	10^6	0.0001	9.5×10^{-6}	4.2×10^5	0.1	110	2.0	0.1-110
		1.85	0.70	0.70	0.1	38	0.70	0.70
	3×10^5	0.0001	3.2×10^{-5}	1.3×10^5	0.1	33	2.0	0.1-33
		0.854	1.1	1.1	0.1	18	1.1	1.1
	10^5	0.0001	9.5×10^{-5}	4.2×10^4	0.1	11	2.0	0.1-11
		0.382	1.5	1.5	0.1	7.8	1.5	1.5
	3×10^4	0.0001	3.2×10^{-4}	1.3×10^4	0.1	3.3	2.0	0.1-3.3
		0.139	1.8	1.8	0.1	2.8	1.8	1.8

Table 2.7: Rebinding Probabilities P for Different Surface Site Densities

$[G_s(0)]_{min}$	K	X	P					
			S_1	S_2	S_3	S_4	S_{max}	S range
0.05	10^7	0.0001	2.4×10^{-9}	0.79	5.0×10^{-6}	0.050	1.0×10^{-4}	5.0×10^{-6}-0.050
		0.643	1.0×10^{-4}	1.0×10^{-4}	8.2×10^{-6}	0.050	1.0×10^{-4}	1.0×10^{-4}
	3×10^6	0.0001	2.6×10^{-8}	0.79	1.7×10^{-5}	0.050	3.3×10^{-4}	1.7×10^{-5}-0.050
		0.253	3.3×10^{-4}	3.3×10^{-4}	2.1×10^{-5}	0.050	3.3×10^{-4}	3.3×10^{-4}
	10^6	0.0001	2.4×10^{-7}	0.79	5.0×10^{-5}	0.050	0.0010	5.0×10^{-5}-0.050
		0.0964	0.0010	0.0010	5.5×10^{-5}	0.050	0.0010	0.0010
	3×10^5	0.0001	2.6×10^{-6}	0.79	1.7×10^{-4}	0.050	0.0033	1.7×10^{-4}-0.050
		0.0308	0.0033	0.0033	1.7×10^{-4}	0.050	0.0033	0.0033
	10^5	0.0001	2.4×10^{-5}	0.79	5.0×10^{-4}	0.050	0.0098	5.0×10^{-4}-0.050
		0.0105	0.0098	0.0098	5.1×10^{-4}	0.050	0.0098	0.0098
	3×10^4	0.0001	2.7×10^{-4}	0.79	0.0017	0.050	0.031	0.0017-0.050
		0.00316	0.031	0.031	0.0017	0.050	0.031	0.031
0.01	10^7	0.0001	4.8×10^{-10}	0.95	5.0×10^{-6}	0.050	1.0×10^{-4}	5.0×10^{-6}-0.050
		1.85	1.0×10^{-4}	1.0×10^{-4}	1.4×10^{-5}	0.050	1.0×10^{-4}	1.0×10^{-4}
	3×10^6	0.0001	5.3×10^{-9}	0.95	1.7×10^{-5}	0.050	3.3×10^{-4}	1.7×10^{-5}-0.050
		0.855	3.3×10^{-4}	3.3×10^{-4}	3.1×10^{-5}	0.050	3.3×10^{-4}	3.3×10^{-4}
	10^6	0.0001	4.8×10^{-8}	0.95	5.0×10^{-5}	0.050	0.0010	5.0×10^{-5}-0.050
		0.382	0.0010	0.0010	6.9×10^{-5}	0.050	0.0010	0.0010
	3×10^5	0.0001	5.3×10^{-7}	0.95	1.7×10^{-4}	0.050	0.0033	1.7×10^{-4}-0.050
		0.139	0.0033	0.0033	1.9×10^{-4}	0.050	0.0033	0.0033
	10^5	0.0001	4.8×10^{-6}	0.95	5.0×10^{-4}	0.050	0.0098	5.0×10^{-4}-0.050
		0.0503	0.0098	0.0098	5.3×10^{-4}	0.050	0.0098	0.0098
	3×10^4	0.0001	5.3×10^{-5}	0.95	0.0017	0.050	0.031	0.0017-0.050
		0.0156	0.031	0.031	0.0017	0.050	0.031	0.031
0.005	10^7	0.0001	2.4×10^{-10}	0.98	5.0×10^{-6}	0.050	1.0×10^{-4}	5.0×10^{-6}-0.050
		2.79	1.0×10^{-4}	1.0×10^{-4}	1.9×10^{-5}	0.050	1.0×10^{-4}	1.0×10^{-4}
	3×10^6	0.0001	2.6×10^{-9}	0.98	1.7×10^{-5}	0.050	3.3×10^{-4}	1.7×10^{-5}-0.050
		1.35	3.3×10^{-4}	3.3×10^{-4}	3.9×10^{-5}	0.050	3.3×10^{-4}	3.3×10^{-4}
	10^6	0.0001	2.4×10^{-8}	0.98	5.0×10^{-5}	0.050	0.0010	5.0×10^{-5}-0.050
		0.643	0.0010	0.0010	8.2×10^{-5}	0.050	0.0010	0.0010
	3×10^5	0.0001	2.6×10^{-7}	0.98	1.7×10^{-4}	0.050	0.0033	1.7×10^{-4}-0.050
		0.253	0.0033	0.0033	2.1×10^{-4}	0.050	0.0033	0.0033
	10^5	0.0001	2.4×10^{-6}	0.98	5.0×10^{-4}	0.050	0.0098	5.0×10^{-4}-0.050
		0.0964	0.0098	0.0098	5.5×10^{-4}	0.050	0.0098	0.0098
	3×10^4	0.0001	2.6×10^{-5}	0.98	0.0017	0.050	0.031	0.0017-0.050
		0.0308	0.031	0.031	0.0017	0.050	0.031	0.031
0.001	10^7	0.0001	4.8×10^{-11}	1.0	5.0×10^{-6}	0.050	1.0×10^{-4}	5.0×10^{-6}-0.050
		6.79	1.0×10^{-4}	1.0×10^{-4}	3.9×10^{-5}	0.050	1.0×10^{-4}	1.0×10^{-4}
	3×10^6	0.0001	5.3×10^{-10}	1.0	1.7×10^{-5}	0.050	3.3×10^{-4}	1.7×10^{-5}-0.050
		3.51	3.3×10^{-4}	3.3×10^{-4}	7.5×10^{-5}	0.050	3.3×10^{-4}	3.3×10^{-4}
	10^6	0.0001	4.8×10^{-9}	1.0	5.0×10^{-5}	0.050	0.0010	5.0×10^{-5}-0.050
		1.85	0.0010	0.0010	1.4×10^{-4}	0.050	0.0010	0.0010
	3×10^5	0.0001	5.3×10^{-8}	1.0	1.7×10^{-4}	0.050	0.0033	1.7×10^{-4}-0.050
		0.854	0.0033	0.0033	3.1×10^{-4}	0.050	0.0033	0.0033
	10^5	0.0001	4.8×10^{-7}	1.0	5.0×10^{-4}	0.050	0.0098	5.0×10^{-4}-0.050
		0.382	0.0098	0.0098	6.9×10^{-4}	0.050	0.0098	0.0098
	3×10^4	0.0001	5.3×10^{-6}	1.0	0.0017	0.050	0.031	0.0017-0.050
		0.139	0.031	0.031	0.0019	0.050	0.031	0.031

In Tables 2.4 – 2.7 equilibrium constants K are in units of M^{-1}, concentrations A are in units of nM, and surface site densities are in units of molecules/μm^2. $G_s(0)$ values, $G_a(0)$ values, X = KA values, and rebinding probabilities P are unit-less. In all cases, it has been assumed that d = 0.1 μm, h = 0.5 μm, D = 50 $\mu m^2 s^{-1}$ and $k_a = 10^6\ M^{-1}s^{-1}$. Data are given for the four cases in which the minimum tolerable value of $G_s(0)$, denoted by $[G_s(0)]_{min}$, is 0.05, 0.01, 0.005 or 0.001.

By comparing the material in Tables 2.4 – 2.7 with that in Table 2.3 and Eqs. 2.13-2.18, the following conclusions can be made: 1) The values of X = KA can be considerably higher if it is possible to work at lower values of $G_s(0)$ than those specified by Criterion C. For example, if the minimum allowed value of $G_s(0)$ is 0.001, for K = 10^7 M^{-1}, X values as high as 6.8 can be tolerated, and for K = 3 x 10^4 M^{-1}, X values up to 0.14 are predicted to be tolerable. These higher values of X would make it more likely that k_a, in addition to k_d, could be measured. Higher X values would also facilitate measurement of a broader range of K values by using either $F_{pos}(A)$ and $F_{neg}(A)$, or $G_{pos}(0)$ and $G_{neg}(0)$. 2) The minimum and maximum values of the surface site densities set by the minimum value of $G_s(0)$, S_1 and S_2, are lower and higher, respectively, for given values of K and X. 3) The surface site densities at which $G_s(0)$ is maximized, S_{max}, do not change. 4) The minimum surface site densities set by Criterion D, S_3, do not change. 5) The rebinding probabilities P depend only on S, X, k_a and D. Thus, changing Criterion C does not change the maximum surface site densities S_4 set by Criterion E. 6) Reducing the minimum allowed value of $G_s(0)$ changes the ratios $G_s(0)/G_a(0)$ in a rather complex manner. However, this ratio is still always much greater than 0.1, for the conditions considered, when $S = S_{max}$. 7) The rebinding probabilities also change, but are often very low, remain equal to 0.05 when $S = S_4$, and are always less than 0.05 when $S = S_{max}$.

2.5.4 Future Directions

The use of TIR-FCS to quantify the thermodynamic and kinetic parameters governing the reversible association of fluorescent ligands with non-fluorescent surface binding sites shows great promise. However, the large number of parameters that affect the ability of TIR-FCS to provide information about surface binding kinetics complicates experimental design. The work described herein provides a comprehensive guide that addresses this issue. The theoretical predictions should be testable by careful *in vitro* measurements as a function of K, k_a, k_d, A, S, d, h, D and the excitation intensity. Only a simple reversible bimolecular reaction between soluble, fluorescent ligands and laterally immobile, non-fluorescent surface binding sites has been addressed here, but in many cases a more complex situation will be of interest. However, understanding this first simple mechanism in the context of TIR-FCS is a pre-requisite for extension to more complex processes, the need for which becomes evident after reviewing prior, related experimental results. Three extensions of interest are as follows: 1) the use of a single fluorescent reporter in solution to examine the thermodynamic and kinetic parameters describing the interaction of soluble, non-fluorescent molecules that compete with the fluorescent reporters for occupation of the surface binding sites; 2) the use of a single fluorescent reporter in solution to examine the thermodynamic and kinetic parameters describing the interaction of soluble, non-fluorescent molecules with the surface binding sites that subsequently inhibits or enhances the interaction of the fluorescent reporters with the surface binding sites; and 3) the use of a single fluorescent reporter in solution to investigate its interaction with soluble, non-fluorescent molecules that inhibit or enhance the interaction of the fluorescent reporter with the surface binding sites. All three of

these extensions are quite important for processes in which the non-fluorescent molecules of interest are too small to be directly conjugated to a fluorophore without perturbing the values of the parameters of interest. As described above, additional extensions of interest include application of TIR-FCS to enzyme kinetics; multivalent, fluorescent ligands; and cellular or other processes in which the binding sites are laterally mobile.

2.6 Acknowledgements

We thank Gabriel Yeung and Matthew Hrabak for their contributions. This work was supported by NSF grant MCB-0641087 and NIH grant GM-041402.

2.7 References

1. Thompson, N. L., Navaratnarajah, P., Wang, X. (2010) Total internal reflection with fluorescence correlation spectroscopy. *Reviews in Fluorescence*; Geddes, CD, Ed.; Springer: New York; pp 345-380.

2. Thompson, N. L., Wang, X., Navaratnarajah, P. (2008) Total internal reflection with fluorescence correlation spectroscopy: Applications to substrate-supported planar membranes. *Journal of Structural Biology 168*, 95-106.

3. Thompson, N. L., Steele, B. L. (2007) Total internal reflection with fluorescence correlation spectroscopy. *Nature Protocols 2*, 878-890.

4. Thompson, N. L., Pero, J. K. (2006) Total internal reflection-fluorescence correlation spectroscopy. *Reviews in Fluorescence*. Springer, New York, Vol.3, 15-237.

5. Anhut, T., Hassler, K., Lasser, T., Konig, K., Rigler, R. (2005) Fluorescence correlation spectroscopy on dielectric surfaces in total internal reflection geometries. *Proceedings of the SPIE 5699*, 159-166.

6. Leutenegger, M., Blom, H., Widengren, J., Eggeling, C., Gösch, M., Leitgeb, R. A., Lasser, T. (2006) Dual-color total internal reflection fluorescence cross-correlation spectroscopy. *Journal of Biomedical Optics 11*, 1-3.

7. Ohsugi, Y., Saito, K., Tamura, M., Kinjo, M. (2006) Lateral mobility of membrane-binding proteins in living cells measured by total internal reflection fluorescence correlation spectroscopy. *Biophysical Journal 91*, 3456-3464.

8. Ohsugi, Y., Kinjo, M. (2006) Analysis of membrane-binding protein mobility in living cells using total internal reflection fluorescence correlation spectroscopy. *Biophysical Reviews and Letters 1*, 293-299.

9. Hassler, K., Anhut, T., Rigler, R., Gösch, M., Lasser, T. (2005) High count rates with total internal reflection fluorescence correlation spectroscopy. *Biophysical Journal 88*, L01-L03.

10. Hassler, K., Leutenegger, M., Rigler, P., Rao, R., Rigler, R., Gösch, M., Lasser, T. (2005) Total internal reflection fluorescence correlation spectroscopy (TIR-FCS) with low background and high count-rate per molecule. *Optics Express 13*, 7415-7423.

11. Harlepp, S., Robert, J., Darnton, N. C., Chatenay, D. (2004) Subnanometric measurements of evanescent wave penetration depth using total internal reflection microscopy combined with fluorescent correlation spectroscopy. *Applied Physics Letters 85*, 3917-3919.

12. Ruckstuhl, T., Seeger, S. (2004) Attoliter detection volumes by confocal total-internal-reflection fluorescence microscopy. *Optics Letters 29*, 569-571.

13. Pero, J. K., Hass, E. M., Thompson, N. L. (2006) Size dependence of protein diffusion very close to membrane surfaces: Measurement by total internal reflection with fluorescence correlation spectroscopy. *Journal of Physical Chemistry 110*, 10910-10918.

14. Starr, T. E., Thompson, N. L. (2002) Local diffusion and concentration of IgG near planar membranes: Measurement by total internal reflection with fluorescence correlation spectroscopy, *Journal of Physical Chemistry B 106*, 2365-2371.

15. Kyoung, M., Sheets, E. D. (2008) Vesicle diffusion close to a membrane: intermembrane interactions measured with fluorescence correlation spectroscopy. *Biophysical Journal 95*, 5789-5797.

16. McCain, K. S., Schluesche, P., Harris, J. M. (2004) Modifying the adsorption behavior of polyamidoamine dendrimers at silica surfaces investigated by total internal reflection fluorescence correlation spectroscopy. *Analytical Chemistry 76*, 930-938.

17. McCain, K. S., Schluesche, P., Harris, J. M. (2004) Poly(amidoamine) dendrimers as nanoscale diffusion probes in sol-gel films investigated by total internal reflection fluorescence spectroscopy. *Analytical Chemistry 76*, 939-946.

18. McCain, K. S., Harris, J. M. (2003) Total internal reflection fluorescence-correlation spectroscopy study of molecular transport in thin sol-gel films. *Analytical Chemistry 75*, 3616-3624.

19. Holt, M., Cooke, A., Neef, A., Lagnado, L. (2004) High mobility of vesicles supports continuous exocytosis at a ribbon synapse. *Current Biology 14*, 173-183.

20. Johns, L. M., Levitan, E. S., Shelden, E. A., Holz, R. W., Axelrod, D. (2001) Restriction of secretory granule motion near the plasma membrane of chromaffin cells. *Journal of Cell Biology 153*, 177-190.

21. Thompson, N. L., Axelrod, D. (1983) Immunoglobulin surface-binding kinetics studied by total internal reflection with fluorescence correlation spectroscopy. *Biophysical Journal 43*, 103-114.

22. Hansen, R. L., Harris, J. M. (1998) Total internal reflection fluorescence correlation spectroscopy for counting molecules at solid/liquid interfaces. *Analytical Chemistry 70*: 2565-2575.

23. Hansen, R. L., Harris, J. M. (1998) Measuring reversible adsorption kinetics of small molecules at solid/liquid interfaces by total internal reflection fluorescence correlation spectroscopy. *Analytical Chemistry 70*, 4247-4256.

24. Sonesson, A. W., Blom, H., Hassler, K., Elofsson, U. M., Callisen, T. H., Widengren, J., Brismar, H. (2008) Protein-surfactant interactions at hydrophobic interfaces studied with total internal reflection fluorescence correlation spectroscopy (TIR-FCS). *Journal of Colloid and Interface Science 317*, 449-457.

25. Lieto, A. M., Cush, R. C., Thompson, N. L. (2003) Ligand-receptor kinetics measured by total internal reflection with fluorescence correlation spectroscopy. *Biophysical Journal 85*, 3294-3302.

26. Hassler, K., Rigler, P., Blom, H., Rigler, R., Widengren, J., Lasser, T. (2007) Dynamic disorder in horseradish peroxidase observed with total internal reflection fluorescence correlation spectroscopy. *Optics Express 15*, 5366-5375.

27. Blom, H., Chmyrov, A., Hassler, K., Davis, L. M., Widengren, J. (2009) Triplet-state investigations of fluorescent dyes at dielectric interfaces using total internal reflection fluorescence correlation spectroscopy. *Journal of Physical Chemistry A 113*, 5554-5566.

28. Blom, H., Chmyrov, A., Hassler, K., Davis, L. M., Widengren, J. (2010) Electrostatic interactions of fluorescent molecules with dielectric interfaces studied by total internal reflection fluorescence correlation spectroscopy. *International Journal of Molecular Sciences 11*, 386-406.

29. Ohsugi, Y., Kinjo, M. (2009) Multipoint fluorescence correlation spectroscopy with total internal reflection fluorescence microscope. *Journal of Biomedical Optics 14*, 014030-1—014030-4.

30. Digman, M. A., Brown, C. M., Horwitz, A. R., Mantulin, W. W., Gratton, E. (2008) Paxillin dynamics measured during adhesion assembly and disassembly by correlation spectroscopy. *Biophysical Journal 94*, 2819-2831.

31. Sankaran, J., Manna, M., Guo, L., Kraut, R., Wohland, T. (2009) Diffusion, transport, and cell membrane organization investigated by imaging fluorescence cross-correlation spectroscopy. *Biophysical Journal 97*, 2630-2639.

32. Guo, L., Har, Y., Sankaran, J., Hong, Y. M., Kannan, B., Wohland, T. (2008) Molecular diffusion measurement in lipid bilayers over wide concentration ranges: A comparative study. *ChemPhysChem 9*, 721-728.

33. Kannan, B., Guo, L., Sudhaharan, T., Ahmed, S., Maruyama, I., Wohland, T. (2007) Spatially resolved total internal reflection fluorescence correlation

microscopy using an electron multiplying charge-coupled device camera. *Analytical Chemistry 79*, 4463-4470.

34. Thompson, N. L. (1982) Surface binding kinetic rates of nonfluorescent molecules may be obtained by total internal reflection with fluorescence correlation spectroscopy. *Biophysical Journal 38*, 327-329.

35. Lieto, A. M., Thompson, N. L. (2004) Total internal reflection with fluorescence correlation spectroscopy: Nonfluorescent competitors. *Biophysical Journal* 87, 1268-1278.

36. Starr, T. E., Thompson, N. L. (2001) Total internal reflection with fluorescence correlation spectroscopy: Combined surface reaction and solution diffusion. *Biophysical Journal 80*, 1575-1584.

37. Thompson, N. L., Burghardt, T. P., Axelrod, D. (1981) Measuring surface dynamics of biomolecules by total internal reflection fluorescence with photobleaching recovery or correlation spectroscopy. *Biophysical Journal 33*, 435-454.

38. Gesty-Palmer, D., Thompson, N. L. (1997) Binding of the soluble, truncated form of an Fc receptor (mouse FcγRII) to membrane-bound IgG as measured by total internal reflection fluorescence microscopy. *Journal of Molecular Recognition 10*, 63-72.

39. Thompson, N. L., Pearce, K. H., Hsieh, H. V. (1993) Total internal reflection fluorescence microscopy: Application to substrate-supported planar membranes. *Eur. Biophysical Journal 22*, 367-378.

40. Pearce, K. H., Hof, M., Lentz, B. R., Thompson, N. L. (1993) Comparison of the membrane binding kinetics of bovine prothrombin and its fragment 1. *Journal of Biological Chemistry 268*, 22984-22991.

41. Hsieh, H. V., Poglitsch, C. L., Thompson, N. L. (1992) Direct measurement of the weak interactions between a mouse Fc receptor (FcγRII) and IgG1 in the absence and presence of hapten: A total internal reflection fluorescence microscopy study. *Biochemistry 31*, 11562-11566.

42. Pisarchick, M. L., Thompson, N. L. (1990) Binding of a monoclonal antibody and its Fab fragment to supported phospholipid monolayers measured by total internal reflection fluorescence microscopy. *Biophysical Journal 58*, 1235-1249.

43. Lagerholm, B. C., Thompson, N. L. (1998) Theory for ligand rebinding at cell membrane surfaces. *Biophysical Journal 74*, 1215-1228.

44. Lagerholm, B. C., Thompson, N. L. (2000) Temporal dependence of ligand dissociation and rebinding at cell membrane surfaces. *Journal of Physical Chemistry B 104*, 863-868.

45. Abramowitz, M., Stegun, I. A. (1974) Handbook of Mathematical Functions. Dover Publications, New York. 297-329.

46. Hsieh, H. V., Thompson, N. L. (1995) Dissociation kinetics between a mouse Fc receptor (FcγRII) and IgG: Measurement by total internal reflection with fluorescence photobleaching recovery. *Biochemistry 34*, 12481-12488.

47. Pisarchick, M. L., Gesty, D., Thompson, N. L. (1992) Binding kinetics of an anti-dinitrophenyl monoclonal Fab on supported phospholipid monolayers measured by total internal reflection with fluorescence photobleaching recovery. *Biophysical Journal 63*, 215-223.

Chapter 3

Rifampicin – independent interactions between the pregnane X receptor ligand binding domain and peptide fragments of co-activator and co-repressor proteins

3.1 PXR as a Potential Test System for TIR-FCS

As discussed in the introduction, theoretical work predicted that TIR-FCS can yield thermodynamic and kinetic information about nonfluorescent molecules that bind surface binding sites and in so doing, alter the binding of fluorescent reporters to the same sites. Two types of nonfluorescent ligands have been defined: 1) nonfluorescent effectors bind surface-bound receptors and allosterically enhance the binding of fluorescent ligands to these receptors; while 2) nonfluorescent competitors compete with fluorescent ligands to bind surface-bound receptors.

To test the theoretical predictions relating to TIR-FCS and nonfluorescent effectors, we set out to establish a model system consisting of a nuclear receptor called the pregnane X receptor (PXR), peptides derived from one of its co-activator proteins and an established PXR agonist, rifampicin. Nuclear receptors are transcription factors and the existing model of nuclear receptor action states that upon binding agonists, nuclear receptors preferentially associate with co-activators, which in turn recruit downstream members of the cell's transcription machinery.

We established an experimental system in which PXR, immobilized on a neutravidin-coated fused silica surface, served as a surface binding site, while a fluorescently labeled peptide derived from the steroid receptor co-activator 1 (SRC-1) served as a fluorescent reporter. Rifampicin was to act as a nonfluorescent effector. As the interaction among PXR, its co-activators and agonists had not been biophysically characterized prior to our work, we used established techniques, TIRFM and TIRFM combined with fluorescence recovery after photobleaching, to obtain the thermodynamics and kinetics of PXR interacting with fluorescently labeled SRC-1 peptide in the presence and absence of rifampicin. Much to our surprise, rifampicin did not act as an effector and increase PXR's affinity for the co-activator peptide. These findings have significant implications for the existing model of PXR action and are the subject of this chapter.

It goes without saying that PXR and its interacting partners cannot serve as a model to test whether TIR-FCS yields kinetic information about nonfluorescent effectors. However, during the course of our work we found that peptides derived from co-repressor proteins compete with co-activators to bind PXR. Moreover, co-activators and co-repressors interact with PXR with equilibrium dissociation constants that are significantly different, making PXR and its co-regulators a suitable model with which to test theoretical predictions pertaining to nonfluorescent competitors. These proteins can also be used to test experimental conditions detailed in Chapter 2 that were predicted to yield autocorrelation curves containing significant thermodynamic and kinetic information about relevant ligand-receptor interactions.

3.2 Overview

The pregnane X receptor (PXR), a member of the nuclear receptor superfamily, regulates the expression of drug-metabolizing enzymes in a ligand-dependent manner. The conventional view of nuclear receptor action is that ligand binding enhances the receptor's affinity for co-activator proteins, while decreasing its affinity for co-repressors. To date, however, no known rigorous biophysical studies have been conducted to investigate the interaction between PXR, its co-regulators and ligands. In the present work, steady-state total internal reflection fluorescence microscopy (TIRFM) and total internal reflection with fluorescence recovery after photobleaching were used to measure the thermodynamics and kinetics of the interaction between the PXR ligand binding domain and a peptide fragment of the steroid receptor co-activator-1 (SRC-1) in the presence and absence of the established PXR agonist, rifampicin. Equilibrium dissociation and dissociation rate constants of about 5 μM and 2 s^{-1}, respectively, were obtained both in the presence and absence of rifampicin, indicating that the ligand does not enhance the affinity of the PXR and SRC-1 fragments. Additionally, TIRFM was used to examine the interaction between PXR and a peptide fragment of the co-repressor protein, the silencing mediator for retinoid and thyroid receptors (SMRT). An equilibrium dissociation constant of about 70 μM was obtained for SMRT in the presence and absence of rifampicin. These results strongly suggest that the mechanism of ligand-dependent activation in PXR differs significantly from that seen in many other nuclear receptors.

3.3 Introduction

The nuclear receptor superfamily consists of structurally related proteins that regulate the transcription of target genes in a ligand-dependent manner. Nuclear receptors, which include the estrogen, androgen, thyroid and vitamin D receptors, regulate a variety of biological processes including reproduction, development, metabolism and energy homeostasis, in response to various hydrophobic ligands. The pregnane X receptor (PXR), a member of the nuclear receptor superfamily, protects the body from potentially toxic compounds by regulating the expression of proteins that metabolize and excrete these compounds from cells (*1*).

PXR binds promiscuously to a wide variety of compounds including naturally occurring steroids, hormones and bile acids, as well as exogenous ligands like insecticides, herbal extracts and pharmaceutical products (*1*). PXR has been implicated in adverse drug-drug interactions, whereupon being activated by a drug, PXR promotes the expression of enzymes that metabolize the activating drug, as well as other co-administered therapeutics. Such adverse effects have been observed with hyperforin, a constituent in the herbal product St. John's Wort, and rifampicin, an antibiotic, both of which have been shown to bind and activate PXR (*2-7*).

PXR works in concert with its heterodimerization partner, the retinoid X receptor (RXR), to bind promoter regions of target genes and co-activators like the steroid receptor co-activator-1 (SRC-1). The PXR-RXR-co-activator-DNA complex then recruits and directs downstream members of the transcription machinery (*5, 6*). Crystal structures of several nuclear receptor ligand binding domains (LBDs) in the apo- and ligand-bound states indicate that in the presence of an agonist, an α-helix at the C-

terminus called activation function-2 (AF-2) undergoes a conformational change that allows nuclear receptors to bind co-activators (*8-11*). Specifically, in the active conformation nuclear receptors form a critical charge clamp with conserved LXXLL motifs (where X is any amino acid) found in co-activators (*11, 12*).

In the absence of ligand, the transcriptional activity of nuclear receptors is, in part, downregulated by the action of co-repressor proteins. The nuclear receptor co-repressor known as the silencing mediator of retinoid and thyroid receptors (SMRT) has been shown to repress both the basal and ligand-induced transcriptional activity of PXR (*13-15*). Co-repressors bind nuclear receptors via receptor interaction domains containing conserved LXXXIXXXL motifs and recruit proteins, including histone deacetylases, that suppress transcription. A crystal structure of a nuclear receptor (peroxisome proliferator-activated receptor-α) LBD in complex with a peptide fragment of SMRT shows that the AF-2 is displaced from its active confirmation upon co-repressor binding (*16*). Co-repressors thereby inhibit the transcriptional activity of nuclear receptors by preventing the recruitment of co-activators.

This paper provides a biophysical assessment of the interaction between PXR-LBD and peptides derived from the co-activator, SRC-1, and the co-repressor, SMRT, in the presence and absence of the well established PXR agonist, rifampicin. For the first time, we report equilibrium constants for PXR-LBD/co-regulator interactions and dissociation rate constants for the PXR-LBD/SRC-1 interaction measured by steady-state total internal reflection fluorescence microscopy [TIRFM; (*17-20*)] and total internal reflection with fluorescence recovery after photobleaching [TIR-FRAP; (*21-23*)], respectively. This quantitative information strongly suggests that the mode of ligand-

dependent activation of PXR differs from that of most other nuclear receptors studied to date.

3.4 Materials and Methods

3.4.1 PXR-LBD Cloning, Expression, Purification and Labeling

The LBD of human PXR (residues 130-434; see Figure 3.1) was expressed as a fusion protein with an amino-terminal AviTag™ and His_6 tag (for purification). The AviTag™ allows for the specific biotinylation of the tagged protein by the *Escherichia coli* enzyme BirA. A codon-optimized version of the PXR-LBD gene (GenScript USA, Piscataway, NJ) was cloned into pET21c(+) between NdeI and HindIII, along with an N-terminal AviTag™ sequence (Avidity, Denver, CO) followed by a His_6 sequence. With this insert, two stop-codons were introduced upstream of the C-terminal His_6 tag normally found in pET21c(+). PXR-LBD was co-expressed with an 88-amino acid fragment of SRC-1 to enhance PXR stability. The SRC-1 fragment (residues 623-710), along with the T7 promoter, had been previously inserted into the pACYC184 vector at the HindIII and BamHI sites (*24*, *25*). The pET21c-AviTag-His_6-PXR-LBD and pACYC184-SRC-1 plasmids were co-transformed into the BL21 DE3 Gold *E. coli* strain.

Figure 3.1: Domain Organization of PXR. Activation function 1 (AF-1) is situated at the N-terminus. AF-1 has been shown to mediate ligand-independent transcriptional activity in some nuclear receptors. AF-1 is followed by the DNA binding domain (DBD) and ligand binding domain (LBD). The numbers refer to amino acids.

Terrific Broth (3 L) supplemented with ampicillin (100 µg/mL) and chloramphenicol (35 µg/mL) was inoculated with an overnight culture (0.5% innoculant). Cells were grown at 37 °C to an OD_{600} of ~2.7 and induced with 0.1 mM isopropyl β-D-thiogalactopyranoside at 18 °C for ~16 h. Cells were harvested by centrifugation (30 min, 3500 g, 4 °C) and stored at -80 °C. Cell pellets (~ 25 g) were resuspended in 125 mL of Buffer A [20 mM Tris, pH 7.9, 250 mM NaCl, 5% glycerol, 20 mM imidazole, 0.1 mM Tris(2-carboxyethyl)phosphine (TCEP; Soltec Ventures, Beverly, MA)] supplemented with three protease inhibitor tablets (complete, EDTA-free, Roche Diagnostics, Mannheim, Germany) and DNase (50 µg/mL; Worthington Biochemical Corp., Lakewood, NJ), and then subjected to Dounce homogenization. Cell homogenates were tip sonicated on ice and the cell lysates were then clarified by centrifugation (45 min, 27000 g, 4 °C). The clarified cell lysates were incubated with 750 µL of His-Select® Ni resin (Sigma-Aldrich, St. Louis, MO) equilibrated in Buffer A for 1 h at 4 °C. The resin was subsequently washed with 125 mL of Buffer B (20 mM Tris, pH 7.9, 500 mM NaCl, 5% glycerol, 20 mM imidazole). PXR-LBD was eluted using six aliquots of 1 mL each of Buffer C (20 mM Tris, pH 7.9, 250 mM NaCl, 5% glycerol, 2 mM TCEP, 300 mM imidazole). Protein fractions were combined and dialyzed against Buffer D (20 mM Tris, pH 7.9, 250 mM NaCl, 5% glycerol, 2 mM TCEP) at 4 °C. Thereafter, PXR-LBD was quickly frozen in liquid N_2 and stored at -80 °C in 1 mL aliquots at a concentration of 0.1 mg/mL.

The AviTag-His_6-PXR-LBD fusion protein, henceforth referred to as PXR-LBD, is 38,750 Da with an extinction coefficient at 280 nm of 34,080 $M^{-1}cm^{-1}$ (*26*). Protein concentrations were measured by using both absorbance at 280 nm and the Bradford

Assay (Bio-Rad Laboratories, Hercules, CA). SDS-PAGE with Coomassie Brilliant Blue and silver stains indicated that the primary band was at the molecular weight expected for PXR-LBD and impurities were negligible. Silver stained gels showed no bands close to or at 10 kDa, suggesting that the co-expressed, 9.8 kDa SRC-1 fragment was removed during PXR purification. Western blots with anti-biotin antibodies conjugated to horse radish peroxidase (Cell Signaling Technology, Beverly, MA) were used to confirm *in vivo* biotinylation. The molar ratio of biotin to PXR-LBD, as estimated by using Pierce® Biotin Quantitation Kit (Thermo Scientific, Rockford, IL), ranged from 0.7 to 1.3, indicating that a majority of the protein was biotinylated.

For some control measurements, PXR-LBD was fluorescently labeled with an amine reactive dye, Alexa Fluor® 488 5-TFP (Invitrogen, Carlsbad, CA). Briefly, PXR-LBD eluted from the Ni affinity column during purification was concentrated to about 1.5 mg/mL and incubated with a 10-15 molar excess of the dye for 2 h at 4 °C with continuous, gentle stirring. Free dye was removed by passing the solution through an anion exchange column (4 mL) constructed from Dowex® 1X8 resin (Acros Organics, Morris Plains, NJ) and equilibrated in 10 mM sodium phosphate, 5% glycerol, pH 5.3. Protein was immediately dialyzed against Buffer D. The molar ratio of dye to protein, as determined by the relative absorptivities at 280 and 494 nm, was approximately 0.3. As before, protein aliquots were frozen in liquid N_2 and stored at -80 °C.

A ligand-bound mimic of PXR-LBD was made by mutating two residues in the ligand binding pocket to tryptophans: S247W and C284W (*27*). The mutations were made sequentially using the QuikChange-II Site-Directed Mutagenesis Kit (Stratagene, La Jolla, CA) according to the manufacturer's protocol. The following primers (with

underlining indicating mutated nucleotides) were used for the S247W mutation: forward 5'-gcacatggcagatatg*TGG*acctatatgttcaaaggc-3' and reverse 5'-gcctttgaacatataggt*CCA*cat atctgccatgtgc-3'; and for the C284W mutation: forward 5'-gcagcgtttgaactg*TTG*cagctgcgt ttcaac-3' and reverse 5'-gttgaaacgcagctg*CCA*cagttcaaacgctgc-3'. Mutations were generated using the pET21c-AviTag-His_6-PXR-LBD plasmid as template, and confirmed by sequencing. PXR-LBD (S247W/C284W) was expressed and purified as described above for wild type PXR-LBD.

3.4.2 Co-regulator Peptide Synthesis and Fluorescence Labeling

A 25 amino acid fragment of SRC-1 (676-CPSSWSSLTERHKI**LHRLL**QEGSPS -700) was synthesized at the UNC Microprotein Sequencing and Peptide Synthesis Facility. Residue 680 was mutated from histidine to tryptophan (H680W) to facilitate peptide quantification. The average and monoisotopic molecular weights of the peptide are 2849.18 and 2847.44 g/mol, respectively. The molar absorptivity of the peptide at 280 nm is 5810 $M^{-1}cm^{-1}$. The N-terminal cysteine residue was fluorescently labeled with a thiol-reactive dye, fluorescein C_5 maleimide (AnaSpec, Fremont, CA). Briefly, peptide (5 mg, 1.8 μM), a 2-fold molar excess of TCEP and 4-fold molar excess of dye were combined in 50 mM sodium phosphate, pH 7.6. The reaction mixture was stirred under argon for ~5 h at room temperature, and an additional ~19 h at 4 °C. Free dye was removed by passing the mixture through an anion exchange column (4 mL) constructed from Dowex® 1X8 resin, both equilibrated and washed with 50 mM sodium acetate, pH 5.0. The peptide was further purified using HPLC to remove salts. Briefly, a 0 to 40% gradient of Solvent B (95% acetonitrile, 5% water, 0.1% trifluoroacetic acid) in Solvent A (95% water, 5% acetonitrile, 0.1% trifluoroacetic acid) was generated on an Atlantis

dC_{18} (10 x 100 mm) column and Waters HPLC with Delta 600 pumps (Waters Corp., Milford, MA) at a flow rate of 4 mL/min. Peptide fractions were combined, lyophilized and stored at -20 °C. Peptide labeling was confirmed by mass spectrometry. The molar ratio of fluorescein to peptide was determined by using the absorptivities at 280 nm and 494 nm. Labeling ratios ranged from 0.35 to 0.50. The fluorescently labeled SRC-1 peptide is henceforth denoted as F-SRC-1. Labeled and unlabeled peptides were mixed to form an overall F-SRC-1 labeling ratio of 0.10, unless otherwise indicated.

Peptide fragments of SMRT (2337-TNMG**LEAIIRKAL**MGKYDQWEE-2358) and of a second co-repressor protein, called the nuclear receptor co-repressor (NCoR, 2251-GHSFADPAS-NLG**LEDIIRKAL**MGSF-2275) were synthesized at the UNC Microprotein Sequencing and Peptide Synthesis Facility. The concentration of SMRT (2337 – 2358) was determined spectrophotometrically using the peptide's extinction coefficient at 280 nm, 6970 $M^{-1}cm^{-1}$. The concentration of NCoR (2251 – 2275) was determined by measuring the mass of the lyophilized peptide.

3.4.3 Other Reagents

D-Biotin (Acros Organics, Morris Plains, NJ), unreactive fluorescein reference standard (Invitrogen, Eugene, OR), NeutrAvidin (Thermo Scientific, Rockford, IL), ovalbumin (Sigma-Aldrich, St. Louis, MO), and rifampicin (Fisher Scientific, Fairlawn, NJ) were obtained commercially. Concentrations for the last four reagents were determined spectrophotometrically by using the following extinction coefficients: fluorescein, 68,000 $M^{-1}cm^{-1}$, 494 nm; NeutrAvidin, 99,600 $M^{-1}cm^{-1}$, 280 nm; ovalbumin, 31,500 $M^{-1}cm^{-1}$, 280 nm; and rifampicin, 26,400 $M^{-1}cm^{-1}$, 334 nm. For some control measurements, NeutrAvidin was fluorescently labeled with Alexa Fluor® 488 5-TFP

(Invitrogen, Carlsbad, CA). NeutrAvidin (2 mg/mL) and a 5-fold molar excess of dye were dissolved in 100 mM sodium phosphate, pH 8.0. The mixture was incubated at 25 °C for 1 h with continuous, gentle stirring. Thereafter, free dye was removed by passing the mixture through an anion exchange column (4 mL) constructed from Dowex® 1X8 resin and equilibrated in 100 mM sodium acetate, 500 mM NaCl, pH 4.0. Labeled protein was dialyzed against Buffer D. The molar ratio of dye to protein, determined spectrophotometrically, was approximately 0.7.

3.4.4 Sample Preparation

Immediately before use, all protein samples were centrifuged (~100,000 g, 30 min; Airfuge; Beckman-Coulter, Fullerton, CA) to remove possible aggregates. NeutrAvidin and ovalbumin were filtered (0.1 µm, 13 mm, Anatop; Whatman, GE Healthcare, Piscataway, NJ) following centrifugation. Microscope (3 in. x 1 in. x 1 mm; Gold Seal® Products, Porstmouth, NH) and fused silica (0.25 in. x 1 in. x 1 mm; Quartz Scientific, Fairport Harbor, OH) slides were cleaned by boiling in ICN detergent (MP Biomedicals, Solon, OH) diluted in water, bath sonicating, rinsing extensively in deionized water, and drying at 120 °C. Immediately prior to collecting data, the substrates were further cleaned in an argon ion plasma cleaner (PDC-3XG; Harrick Scientific, Ossining, NY) for 15 min at room temperature. Fused silica slides were mounted on microscope slides using double sided, 0.13 mm thick, tape (part no. 021200-64988; 3M Corp., St. Paul, MN). NeutrAvidin/ovalbumin (0.5/0.1 mg/mL in Buffer D, 60 µL) was applied to the space between the fused silica and microscope slides. Slides were incubated at room temperature for 1 h, allowing the NeutrAvidin and ovalbumin to coat the surfaces of the substrates. Excess protein was removed by washing the inner

sample chambers with Buffer D (200 µL, x 10). NeutrAvidin/ovalbumin – coated sample chambers were treated with PXR-LBD (0.1 mg/mL in Buffer D, 200 µL) for 5 min at room temperature and washed with Buffer D (200 µL, x 10) to remove excess PXR. For steady-state TIRFM and TIR-FRAP measurements to obtain F-SRC-1/PXR-LBD equilibrium and dissociation rate constants, solutions (200 µL) containing F-SRC-1 and ligand in Buffer D at the indicated concentrations were applied to the sample chambers. Immediately thereafter, samples were mounted onto the microscope for data collection. For competition curves to obtain SMRT/PXR-LBD equilibrium constants, solutions (200 µL) containing 5 µM F-SRC-1, rifampicin and SMRT in Buffer D at the indicated concentrations were applied to the sample chambers. SMRT was replaced with a peptide fragment of the co-repressor, NCoR, in some measurements.

3.4.5 Fluorescence Microscopy

Steady-state TIRFM and TIR-FRAP were carried out using the equipment described below. A through-prism TIRFM apparatus was used to generate evanescent illumination with an elliptically Gaussian spatial profile having $1/e^2$- radii of $w_x = 22.4 \pm 0.5$ µm and $w_y = 65.0 \pm 0.4$ µm, respectively (*28*). Measurements were conducted using an argon ion laser (Innova 90-3; Coherent, Palo Alto, CA), an inverted microscope (Zeiss Axiovert 35; Carl Zeiss Inc., Thornwood, NY) with a 40x, 0.55 numerical aperture, long working distance objective (Nikon Instruments Inc., Nelville, NY) and an avalanche photodiode (SPCM-AQ-151; EG&G Optoelectronics, Quebec, Canada) detector. An in-house LabVIEW program and DAQ board (PCI-MIO-16XE-50, National Instruments, Austin, TX) were used to control the instruments. Fluorescence was excited at 488 nm

and detected through a dichroic mirror and barrier filter, at room temperature. All data were fitted in SigmaPlot 11.0 (Systat Software Inc., San Jose, CA).

3.4.6 Steady-State Total Internal Reflection Fluorescence Microscopy

Steady-state TIRFM (*17-19*) was used to measure equilibrium dissociation constants for the interaction between F-SRC-1/PXR-LBD and SMRT/PXR-LBD under different conditions, including at different rifampicin concentrations. All samples were evanescently illuminated and the surface-associated fluorescence was measured using a PC-based correlator board (ALV-5000/E, ALV, Langen, Germany). Fluorescence intensities, averaged over 10 s, were measured at eight distinct sites on a given sample.

To characterize the F-SRC-1/PXR-LBD interaction, the surface-associated fluorescence of samples was measured as a function of the F-SRC-1 concentration in solution. The measured surface-associated fluorescence was assumed to be proportional to the average density of fluorescent molecules bound to surface binding sites (PXR-LBD), as well as the average density of such molecules diffusing in the evanescent wave. To obtain the fluorescence associated with F-SRC-1/PXR-LBD complexes alone, fluorescence measured in the absence of PXR-LBD was subtracted from the total fluorescence. This background-corrected fluorescence was plotted as a function of the F-SRC-1 concentration, and fit to a model of single-site binding to obtain an apparent equilibrium dissociation constant.

Competition curves were used to determine the equilibrium dissociation constant for the interaction between PXR-LBD and co-repressor peptides. TIRFM was used to measure the surface-associated fluorescence arising from 5 μM F-SRC-1 reversibly interacting with surface-immobilized PXR-LBD in the presence of an increasing

concentration of co-repressor peptide. The co-repressor competed with F-SRC-1 to bind PXR-LBD and a corresponding decrease in the surface-associated fluorescence was observed. Background, arising from fluorescence due to the diffusion of free F-SRC-1 in the evanescent wave, was subtracted and the data were fit to an appropriate model (see *Results*) to obtain the equilibrium dissociation constant for the interaction between the PXR and co-repressor fragments.

3.4.7 Total Internal Reflection with Fluorescence Recovery After Photobleaching

TIR-FRAP (*21, 22, 29, 30*) was used to measure the apparent dissociation rate constant for the F-SRC-1/PXR-LBD interaction. In this technique, an evanescently illuminated area is photobleached, and the subsequent fluorescence recovery is observed as a function of time. Fluorescence recovery, which occurs when photobleached molecules on the surface are replaced by unbleached molecules from solution, is proportional to the intrinsic rate at which photobleached molecules dissociate from surface binding sites, in the absence of surface rebinding. Recovery curves were fit to an appropriate exponential model to obtain the off-rate for the F-SRC-1/PXR-LBD interaction (see *Results* for more detail). TIR-FRAP measurements were conducted using bleach pulses with intensities of 100 to 300 mW and associated bleach times of 100 to 50 ms, respectively. Fluorescence recovery was monitored for 30 s after photobleaching.

3.5 Results

TIRFM and related techniques specifically allow one to probe the behavior of fluorescent species close to or at interfaces. Therefore, we immobilized biotinylated PXR-LBD on NeutrAvidin-coated microscope slides via the biotin-avidin linkage.

TIRFM-based techniques were used to examine co-activator and co-repressor peptides in solution reversibly interacting with surface-bound PXR-LBD, in the presence and absence of rifampicin.

3.5.1 Control Measurements

It was necessary, first, to confirm that NeutrAvidin and PXR-LBD were irreversibly bound to the surface. To probe the surface life-time of NeutrAvidin, fluorescently labeled NeutrAvidin (0.5 mg/mL) along with ovalbumin (0.1 mg/mL) was immobilized on microscope slides, the slides were then washed, and the surface-associated fluorescence was monitored for 90 min at 30 min intervals using TIRFM (data not shown). Although the fluorescence decreased 13 ± 3 % over the first 30 min period, no further decrease was observed. To probe the surface life-time of PXR-LBD, slides were coated with a mixture of NeutrAvidin (0.5 mg/mL) and ovalbumin (0.1 mg/mL), washed, treated with fluorescently labeled PXR-LBD (0.1 mg/mL), washed, and then the surface-associated fluorescence was monitored for 90 min at 30 min intervals using TIRFM (data not shown). Although the fluorescence decreased 13 ± 3 % over the 90 min period, the decrease was only 3 ± 3 % after 30 min. As all TIRFM equilibrium and TIR-FRAP kinetic measurements, for individual samples, were obtained within at least 30 min after the final wash, the calibrated surface residency times for NeutrAvidin and PXR were judged to be sufficient.

PXR-LBD was biotinylated at its N-terminal, away from the ligand binding pocket, the SRC-1 peptide binding site, the SMRT binding site and AF-2 (*7, 25*), to minimize the possibility that biotinylation and subsequent immobilization would affect the interaction with ligands and co-regulators. To determine whether PXR-LBD

specifically bound NeutrAvidin during surface immobilization, fluorescently labeled PXR-LBD (F-PXR-LBD) was applied to NeutrAvidin-coated substrates in the presence and absence of excess (100 μM) d-biotin. Figure 3.2 shows that in the presence of excess d-biotin the surface-associated fluorescence decreased markedly, indicating that F-PXR-LBD specifically bound NeutrAvidin. All subsequent measurements were conducted at PXR-LBD concentrations of 0.1 mg/mL.

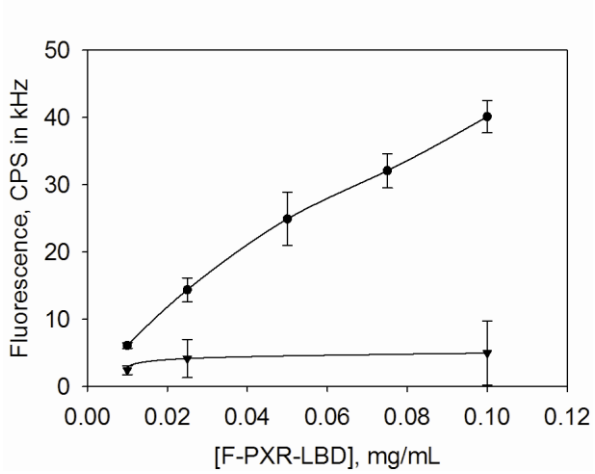

Figure 3.2: Specificity of PXR-LBD Immobilization. The surface-associated fluorescence of F-PXR-LBD bound to immobilized NeutrAvidin was measured, after treating surfaces in the (triangles) presence and (circles) absence of 100 μM d-biotin. The molar ratios of d-biotin to PXR-LBD ranged from approximately 400 (0.01 mg/mL PXR-LBD) to 40 (0.1 mg/mL PXR-LBD). Fluorescence was measured after incubating F-PXR-LBD with surface-bound NeutrAvidin for 5 min and washing with 2 mL of Buffer D. Mean values from three separate samples (obtained from eight points per sample) were averaged to generate the above curve. Uncertainties are standard deviations associated with the three-fold averages. All subsequent measurements were carried out with 0.1 mg/mL PXR-LBD.

PXR has the ability to bind many types of ligands, and in the measurements reported here, the SRC-1 peptide was labeled with fluorescein maleimide. To ensure that fluorescein is not a PXR ligand, the surface-associated fluorescence as a function of the concentration of unreactive fluorescein reference standard in solution was examined in the presence and absence of surface-bound PXR-LBD (data not shown). Data were obtained for fluorescein concentrations ranging up to 9 μM, above the maximum

concentration of *labeled* F-SRC-1 used in subsequent measurements (usually 3.5 μM). The evanescently excited fluorescence intensities measured in the presence and absence of PXR-LBD were identical and linear with the fluorescein concentration indicating that the fluorescence arose solely from fluorescein in solution and that, therefore, fluorescein is not a PXR ligand.

3.5.2 F-SRC-1/PXR-LBD Equilibrium Dissociation Constants Measured by Steady-State TIRFM

Steady-state TIRFM was used to examine the thermodynamics of the interaction between F-SRC-1 and PXR-LBD at different rifampicin concentrations. The surface-associated fluorescence arising from both F-SRC-1 bound to immobilized PXR-LBD and free F-SRC-1 in solution that were close enough to the surface to be excited by the evanescent field, denoted by F(+), was measured as a function of the F-SRC-1 concentration in solution. Also measured was the fluorescence solely from F-SRC-1 in solution, denoted by F(-), obtained from samples not treated with PXR-LBD. The difference, which gives a measure of the density of specifically bound F-SRC-1, is denoted by F(+) - F(-). These three quantities are, in the simplest case, given by

$$\begin{aligned} F(+) &= \frac{QSA}{K_d + A} + QdA + b \\ F(-) &= QdA + b \\ F(+) - F(-) &= \frac{QSA}{K_d + A} \end{aligned} \qquad (3.1)$$

In Eq. 3.1, Q is a proportionality constant, S is the surface density of PXR-LBD, A is the solution concentration of F-SRC-1 (only 10% or 30% of which is actually labeled), K_d is the equilibrium dissociation constant describing the reversible association of F-SRC-1

with PXR-LBD, d is the depth of the evanescent field, and b is a constant background signal.

For a given, matched set of measured F(+) and F(-) intensities (see Figure 3.3A), the following procedure was used to find the best-fit value of the equilibrium dissociation constant K_d. The experimentally determined values of F(-) were fit to the second expression in Eq. 3.1 with A as the abscissa, and Qd and b as free parameters. The best-fit values of Qd and b were used to calculate theoretical values for F(-) for the values of A at which F(+) intensities had been obtained. The theoretical values of F(-) were subtracted from the experimental values of F(+) (see Figure 3.3B). The fluorescence differences were then fit to the third expression in Eq. 3.1 with QS and K_d as free parameters. A representative binding curve from a single trial is shown in Figure 3.3.

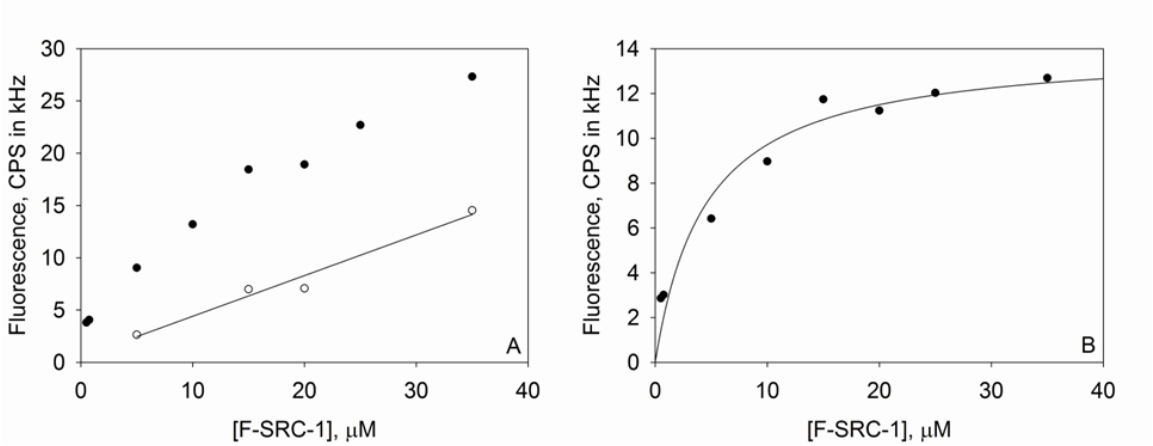

Figure 3.3: Representative F-SRC-1/PXR-LBD Binding Isotherm. These plots, obtained from a single trial, show the surface-associated fluorescence of F-SRC-1 interacting with PXR-LBD in the presence of 1 μM rifampicin: A) Representative values of F(+) (closed circles) and F(-) (open circles); B) Background-subtracted data, F(+) – F(-), curve-fit to the third expression in Eq. 3.1, which yields a K_d of 4.5 ± 1.4 μM, where the error is that associated with the fit. The PXR-LBD surface site density is 2.0 ± 0.2 x 10^3 molecules/μm^2.

Equilibrium dissociation constants pertaining to the F-SRC-1/PXR-LBD interaction, obtained at rifampicin concentrations that ranged from 0 to 100 μM, are tabulated in Table 3.1. As the reported equilibrium dissociation constants for rifampicin

and PXR-LBD are ≤ 10 μM (*31*, *32*), at 100 μM rifampicin one would expect most (≥ 91%) of the surface-immobilized PXR-LBD to be in the ligand-bound state. The measured dissociation constants are within error of each other, indicating that rifampicin does not affect the affinity of the receptor for F-SRC-1. To verify these results, binding curves were obtained where the surface-associated fluorescence was measured as a function of the rifampicin concentration, ranging from 0 to 100 μM (data not shown). In these measurements, the F-SRC-1 was kept constant at 2.5 μM. The surface-associated fluorescence did not change, within experimental uncertainty, with the rifampicin concentration, supporting our previous results that rifampicin does not affect the interaction between the PXR-LBD and SRC-1 fragment. A PXR-LBD mutant (S247W/C284W), which was made to mimic a ligand-bound state of the receptor by introducing bulky tryptophan residues into the ligand binding pocket (*27*), served as a control. Many such mutants have been shown to constitutively recruit co-activator and promote the transcription of reporter genes in a ligand-independent manner (*7*, *27*). The present measurements indicate that the F-SRC-1 peptide interacts with PXR-LBD as though it is ligand-bound, even in the absence of rifampicin (Table 3.1). Additional measurements were carried out with 5 mM TCEP or F-SRC-1 with 30% labeling, as opposed to 2 mM TCEP and 10% labeling for all other curves (Table 3.1). Equilibrium constants obtained at 5 mM TCEP were within error of the K_d values obtained at 2 mM TCEP (10% labeling). This result indicates that 2 mM TCEP was sufficient to prevent significant dimerization of unlabeled SRC-1 molecules via the formation of disulfide bonds, as well as to maintain cysteine residues in PXR-LBD in their reduced state, as they would be *in vivo*. Equilibrium constants obtained using F-SRC-1 with 30% labeling

were within error of those obtained using co-activator with 10% labeling (2 mM TCEP), indicating that the fluorescein tag does not significantly interfere with PXR-LBD/SRC-1 binding.

Table 3.1: F-SRC-1/PXR-LBD Equilibrium Dissociation Constants Measured by Steady-State TIRFM.

PXR-LBD	[Rifampicin], μM	K_d, μM
WT	0	4 ± 2
WT	0.1	5 ± 3
WT	1	4 ± 2
WT	10	5 ± 3
WT	100	4 ± 3
S247W/C284W	0	4 ± 2
WT / S247W/C284W (5 mM TCEP)	0	4 ± 2
WT (30% labeled F-SRC-1)	0	5 ± 2

Reported K_d values are averages of values obtained from two binding isotherms. Controls were carried out with a ligand-bound mimic of the receptor, PXR-LBD (S247W/C284W); 5 mM TCEP, as opposed to 2 mM; and F-SRC-1 with 30% labeling, instead of 10%. For the 5 mM TCEP control, one curve was measured for wild type PXR-LBD and the other for the double tryptophan mutant. Uncertainties are propagated from the errors associated with each of the two fits. WT PXR-LBD refers to AviTag-His_6-PXR-LBD (130-434) fusion protein, with no other modifications.

The density, S, of PXR-LBD at the surface was experimentally determined by using the best fit values of QS (the saturating fluorescence in the binding isotherm) and Qd (the slope of the background), and an estimated value of d ≈ 85 nm for our system (*33*). The density of PXR-LBD at the surface served as an internal control, as the values of *S* should be on the same order of magnitude for all binding curves and within error of each other for measurements conducted with a single batch of PXR. The densities ranged from 1 – 7 x 10^3 molecules/μm^2, with an average of 4 ± 2 x 10^3 molecules/μm^2. For

measurements carried out using the same batch of PXR, the S values, as returned by the fitting program, were always within error of each other.

3.5.3 F-SRC-1/PXR-LBD Dissociation Rate Constants Measured by TIR-FRAP

TIR-FRAP was employed to examine the kinetics of the interaction between F-SRC-1 and PXR-LBD at 0, 10 and 100 μM rifampicin. In conducting these measurements, the surface-associated fluorescence generated by TIR illumination was monitored before and after a short, intense bleach pulse. Once an evanescently illuminated area is photobleached, the fluorescence recovers as surface-bound, photobleached molecules dissociate and are replaced by unbleached molecules in solution. The rate of this recovery reflects the rate at which photobleached molecules dissociate from surface binding sites (*22, 29*). In the absence of surface rebinding, the temporal shape of the recovery curve is predicted to be a single exponential with a rate equal to the intrinsic off-rate (*34*).

Figure 3.4 shows two representative fluorescence recovery curves for 1.25 μM (Fig. 3.4A) and 20 μM (Fig. 3.4B) F-SRC-1 interacting with PXR-LBD in the absence of rifampicin. The curves were obtained using a 300 mW, 50 ms bleach pulse, and fluorescence was measured for 30 s after photobleaching. As shown, fluorescence recovery was rapid and essentially complete after 30 s.

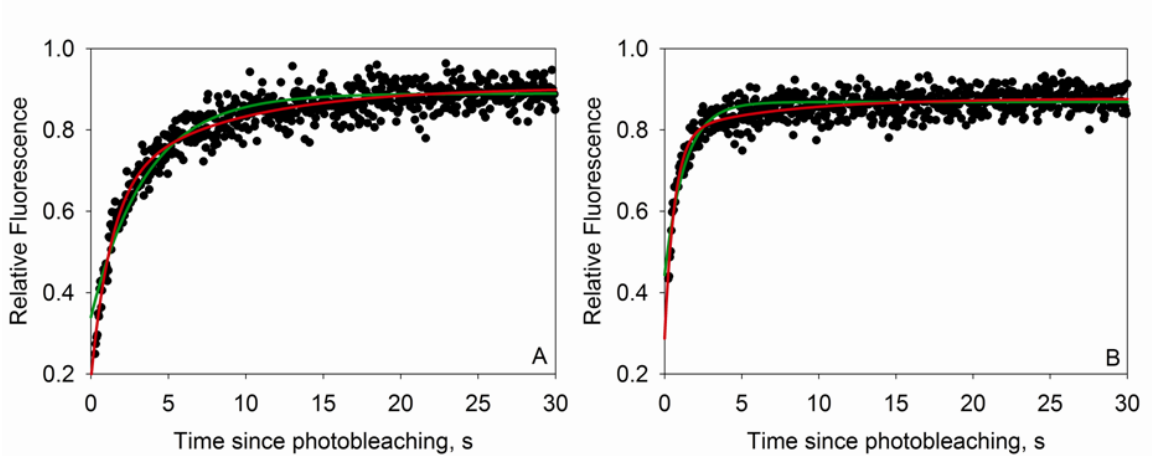

Figure 3.4: Representative Fluorescence Recovery Curves. These plots show typical fluorescence recovery curves for (A) 1.25 μM and (B) 20 μM F-SRC-1 interacting with PXR-LBD in the absence of ligand, obtained using a 300 mW, 50 ms bleach pulse. Fluorescence values have been normalized to average pre-bleach fluorescence values and then fit to one- (green curves; $f_2 = 0$ in Eq. 3.2) and two- (red curves; $f_2 \neq 0$ in Eq. 3.2) exponential models. It is evident, especially at the early recovery times, that the two-exponential model is a better fit for the data. All reported values are derived from two-exponential fits. For the curves shown here the values of f_1, k_1, f_2, k_2 and μ were (A) 8.0 ± 0.4 kHz, 0.76 ± 0.08 s^{-1}, 4.3 ± 0.4 kHz, 0.126 ± 0.012 s^{-1} and 0.88, respectively, and (B) 15.0 ± 0.8 kHz, 1.56 ± 0.13 s^{-1}, 2.5 ± 0.3 kHz, 0.15 ± 0.02 s^{-1} and 0.83, respectively. The weighted average of the two rate constants, k_{off}, was (A) 0.54 s^{-1} and (B) 1.36 s^{-1}.

To confirm that F-SRC-1 was indeed highly reversibly interacting with immobilized PXR-LBD, the surface associated fluorescence was measured following the application of F-SRC-1 and immediately after washing with 2 mL of Buffer D. The surface associated fluorescence was at background levels after washing, indicating that F-SRC-1 was completely washed away and interacts only reversibly with PXR-LBD. This observation also informs one that the larger fragment of SRC-1, with which PXR-LBD is co-expressed, is most likely removed during the washing step following the application of PXR-LBD to the substrate, if not before during PXR-LBD purification (as indicated by gel electrophoresis, see *Materials and Methods*).

In a system such as ours where F-SRC-1 reversibly interacts with surface-bound PXR-LBD, one would at first expect a single intrinsic dissociation rate constant. Hence,

fluorescence recovery curves were expected to be monoexponential, with the single exponent reflecting the one rate constant. However, as illustrated in Figure 3.4 and as previously observed for a variety of other systems (*19, 22, 29*), the curves are not monoexponential, but are in fact better described by the sum of two exponentials,

$$f(t) = f_0 + f_1\left(1 - e^{-k_1 t}\right) + f_2\left(1 - e^{-k_2 t}\right), \tag{3.2}$$

where f_0 is the fluorescence at time zero, defined as the center of the bleach pulse. The weighted average of the two exponential factors, k_1 and k_2, can be used to determine an average off-rate, as follows:

$$k_{off} = \frac{f_1 k_1 + f_2 k_2}{f_1 + f_2}. \tag{3.3}$$

The fractions of the pre-bleach fluorescence, f_p, that were bleached (β) and then recovered (μ) were calculated as follows:

$$\beta = 1 - \frac{f(0)}{f_p} = 1 - \frac{f_0}{f_p};$$
$$\mu = \frac{f(\infty) - f(0)}{f_p - f(0)} = \frac{f_1 + f_2}{f_p - f_0}. \tag{3.4}$$

In the TIR-FRAP measurements, the monitoring excitation intensity was low enough so that in the absence of a bleach pulse, the evanescently excited fluorescence was constant with no measurable decrease during the typical post-bleach monitoring time of 30 s. Potential photo-induced artifacts arising from the intense photobleaching pulse were ruled out by three different types of control measurements. Here, quantitative analysis of recovery curves indicated no significant difference in the best-fit values of k_{off} for (a) a three-fold increase in the bleaching intensity; (b) a two-fold increase in the

bleaching time; or (c) recovery curves obtained following sequential bleaching of identical regions after previous fluorescence recovery.

TIR-FRAP recovery curves were obtained for a range of F-SRC-1 concentrations, at the three different rifampicin concentrations. As shown in Figure 3.5, fluorescence recovery was significantly slower at lower F-SRC-1 concentrations. This observation is almost certainly due to the fact that at lower F-SRC-1 concentrations there is an increased density of free PXR-LBD on the surface. Consequently, bleached molecules that dissociate from surface binding sites rebind free PXR-LBD at a higher frequency, reducing the overall rate of fluorescence recovery and thereby the observed rate constants. The intrinsic dissociation rate constant was taken to be the value at which the weight-averaged off-rate, k_{off}, was maximized and independent of the F-SRC-1 concentration. Towards this end, average off-rates were plotted as a function of the F-SRC-1 concentration and fit to the model shown in Eq. 3.5 (*29*) to determine the limit of the off-rate as the F-SRC-1 concentration approached infinity, given by k_{off}^{∞}:

$$k_{off}(A) = \frac{Ak_{off}^{\infty}}{C + A} \tag{3.5}$$

In Eq. 3.5, $k_{off}(A)$ is the measured average off-rate for a given value of A, and C is an arbitrary constant. The free parameters were k_{off}^{∞} and C. Intrinsic, average dissociation rate constants, k_{off}^{∞}, were obtained for the F-SRC-1/PXR-LBD interaction at 0,10 and 100 μM rifampicin and found to be 2.0 ± 0.1 s^{-1}, 2.4 ± 0.3 s^{-1} and 2.4 ± 0.1 s^{-1}, respectively (Figure 3.5A). As with the thermodynamics, rifampicin does not affect the kinetics of the interaction between F-SRC-1 and PXR-LBD.

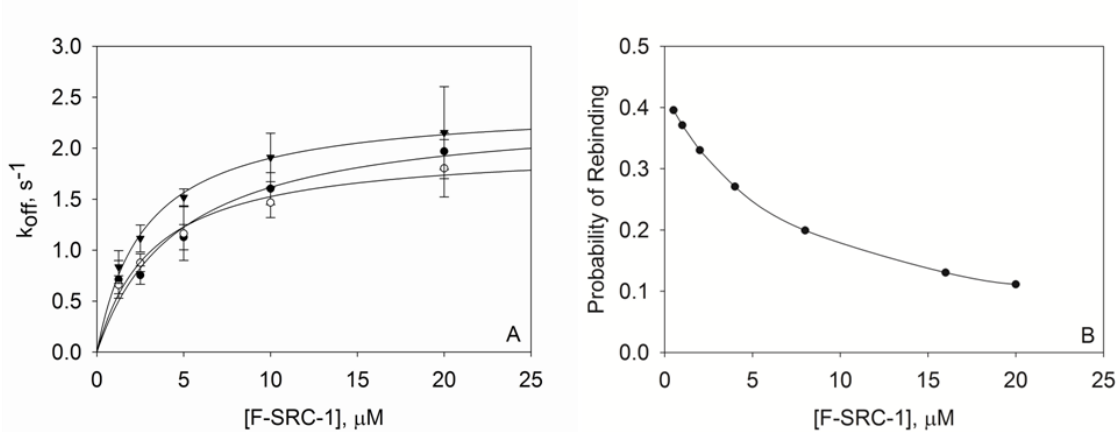

Figure 3.5: F-SRC-1/PXR-LBD Dissociation Rate Constants Measured by TIR-FRAP and Theoretical Probabilities of Rebinding. (A) Four to six recovery curves were measured for each of four (0 μM rifampicin) or three (10 and 100 μM rifampicin) independently prepared samples, for each F-SRC-1 concentration. These measurements were carried out using 300 mW, 50 ms; 200 mW, 50 ms; and 100 mW, 100 ms bleach pulses. Each recovery curve was fit to Eq. 3.2 and the best-fit values of f_1, k_1, f_2, k_2 were used to calculate k_{off} according to Eq. 3.3. The off rates (k_{off}) obtained from the recovery curves pertaining to a single sample were averaged. The points shown in the plot are the averages of 3-4 of these mean k_{off} values for each F-SRC-1 and rifampicin concentration, with the associated standard deviation. These values of k_{off} as a function of F-SRC-1 concentration, in the absence (open circles) and presence (10 μM, closed circles; 100 μM, closed triangles) of rifampicin, were fit to the model in Eq. 3.5. The best-fit values of the intrinsic dissociation rates, k_{off}^{∞}, were 2.0 ± 0.1 s^{-1}, 2.4 ± 0.3 s^{-1} and 2.4 ± 0.1 s^{-1} at 0, 10 and 100 μM rifampicin, respectively. (B) Probabilities of rebinding computed by numerically integrating Eq. 3.6 from t = 0 s (the center of the bleach pulse) to t = 30 s (after photobleaching), using K_d = 4 μM, k_{off} = 2 s^{-1}, S = 3000 molecules μm^{-2}, D = 100 μm^2 s^{-1}, w_x = 22.4 μm and w_y = 65.0 μm.

As previously shown (*35*), the probability that a bleached molecule which dissociates from the origin at time zero has rebound at least once within the illuminated and observed area after the duration of the post-bleach observation is

$$P = -\int_0^{t_f} dt \int_{-w_x}^{w_x} dx \int_{-w_y}^{w_y} dy \frac{1}{4\pi D t} \exp\left(-\frac{x^2+y^2}{4Dt}\right) \frac{d}{dt}\left[\exp\left(\eta^2 t\right) erfc\left(\eta\sqrt{t}\right)\right], \qquad (3.6)$$

where t_f is the duration of the observation time after photobleaching, w_x and w_y are the $1/e^2$-radii of the elliptically Gaussian illuminated area, D is diffusion coefficient of F-SRC-1 in solution and η describes the propensity for rebinding. The parameter η is given by

$$\eta = \frac{k_{on} S}{\sqrt{D}\left(1 + A/K_d\right)}, \tag{3.7}$$

where k_{on} is the association rate constant, obtained by computing the quotient of the measured dissociation rate constant and equilibrium dissociation constant. Figure 3.5B shows the values of Eq. 3.6 numerically evaluated for t_f = 30 s, K_d = 4 μM, k_{off} = 2 s^{-1}, S = 3000 molecules μm^{-2}, D = 100 μm^2 s^{-1}, w_x = 22.4 μm and w_y = 65.0 μm. As shown, P is significant at the lower F-SRC-1 concentrations but becomes negligibly small for the higher F-SRC-1 concentrations. This information is consistent with the interpretation that the measured fluorescence recovery curves are significantly affected by surface rebinding at low F-SRC-1 concentrations but, that at the higher F-SRC-1 concentrations, the effects of surface rebinding are negligible and the recovery curves accurately report the intrinsic surface dissociation kinetics.

3.5.4 SMRT/PXR-LBD Equilibrium Dissociation Constants Measured by Steady-State TIRFM

SMRT/PXR-LBD equilibrium constants were obtained from competition curves in which SMRT was titrated against a fixed concentration of F-SRC-1 (5 μM). Steady-state TIRFM was used to measure the decrease in surface-associated fluorescence as increasing amounts of SMRT competed with a fixed concentration of F-SRC-1 to bind surface-bound PXR-LBD. Competition curves were obtained at rifampicin concentrations of 0, 10 and 100 μM. Background-subtracted data were fit to Eq. 3.8 to obtain the equilibrium dissociation constant, K_d', for the interaction between co-repressor and PXR-LBD.

$$F(+) - F(-) = \frac{QS[A/K_d]}{1 + [A/K_d] + [B/K_d']} \tag{3.8}$$

In Eq. 3.8 Q is a proportionality constant, S is the surface density of PXR-LBD, K_d is the F-SRC-1/PXR-LBD dissociation constant, A is the concentration of F-SRC-1 and B is the concentration of co-repressor. QS and K_d' were free parameters, while K_d and A were fixed at 5 μM. Figure 3.6 (closed circles) shows the background-subtracted, SMRT competition curve obtained in the absence of ligand. Fitting the data in Figure 3.6 to Eq. 3.8 yielded an equilibrium dissociation constant of 65 ± 13 μM for the interaction between SMRT and PXR-LBD. An equilibrium dissociation constant of 51 ± 14 μM was obtained at 100 μM rifampicin (see Table 3.2). The fact that these values are within error of each other indicate that rifampicin does not alter the affinity of SMRT and PXR fragments. Competition curves were also obtained using a peptide fragment of another co-repressor called the nuclear receptor co-repressor (NCoR). NCoR, which has been reported to not interact with PXR (*13*), competed even more weakly with F-SRC-1 to bind surface-bound PXR-LBD (see Figure 3.6; open circles). Fitting these data to Eq. 3.8 yielded an equilibrium constant of 200 ± 50 μM for the NCoR/PXR-LBD interaction in the absence of ligand. This value was within error of those obtained at 10 and 100 μM rifampicin as shown in Table 3.2.

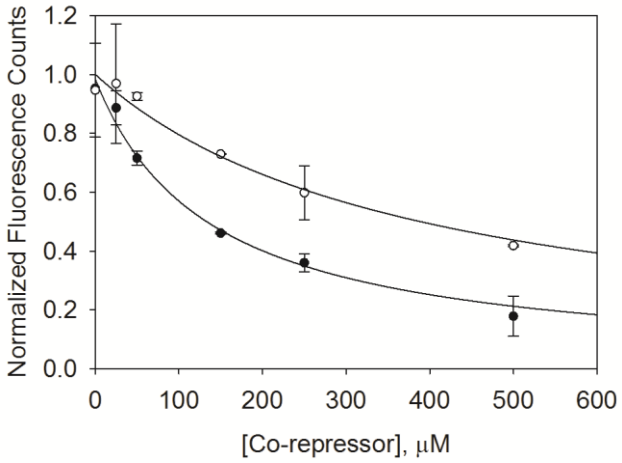

Figure 3.6: Representative Co-repressor Competition Data. This plot shows the background-subtracted and normalized fluorescence as a function of SMRT (closed circles) and NCoR (open circles) concentrations obtained at 5 μM F-SRC-1, in the absence of ligand. Background fluorescence, measured in the absence of surface-immobilized PXR-LBD, was subtracted and the data were fit to Eq. 3.8 with QS and $K_{d'}$ as free parameters and using the fixed parameters, A = 5 μM and K_d = 5 μM. Equilibrium dissociation constants of 65 ± 13 μM and 200 ± 50 μM were obtained for the SMRT/PXR-LBD (closed circles) and NCoR/PXR-LBD (open circles) interactions, respectively. The above data were normalized to fluorescence counts determined using the fit parameter QS, A = 5 μM, K_d = 5 μM and B = 0 μM (no co-repressor). The data are averages of two trials and the errors are the corresponding standard deviations.

Table 3.2: Co-repressor/PXR-LBD Equilibrium Dissociation Constants Measured by Steady-State TIRFM.

[Rifampicin], μM	K_d', μM	
	SMRT	NCoR
0	65 ± 13	200 ± 50
10	82 ± 11	160 ± 40
100	51 ± 14	160 ± 40

Reported K_d' values are averages obtained from two competition curves. Uncertainties are propagated from the errors associated with each of the two fits.

3.6 Discussion

The nuclear receptor PXR plays an important role in the metabolism of endobiotic and xenobiotic compounds, including many pharmaceutical products, by regulating the expression of drug-metabolizing enzymes. The conventional view of nuclear receptor action is that upon binding agonists, nuclear receptors preferentially associate with co-activators, which in turn recruit downstream members of the transcription machinery (*36*). In the present study, we investigated the interaction between the ligand binding domain of PXR and a relevant peptide derived from the co-activator, SRC-1, in the presence and absence of the PXR agonist, rifampicin. Specifically, TIRFM and TIR-FRAP were employed to examine the thermodynamics and kinetics of PXR-LBD interacting with a fluorescently labeled SRC-1 peptide at different rifampicin concentrations. The equilibrium and dissociation rate constants for the PXR-LBD/F-SRC-1 interaction were unchanged in the presence of rifampicin. In the absence of ligand, the basal transcriptional activity of PXR was reported to be significantly reduced by the co-repressor SMRT (*13*). Thus, the thermodynamics of the interaction between PXR-LBD and a peptide fragment of SMRT was also measured using TIRFM. Again, rifampicin had no effect on the PXR-LBD/SMRT interaction. These results indicate that the agonist rifampicin does not affect PXR's affinity for (at least these two) co-regulators.

While no known rigorous biophysical studies have been previously conducted to quantitatively characterize the interaction between PXR, co-activators and ligands, the thermodynamics and kinetics of other nuclear receptors, particularly the steroid hormone receptors, interacting with co-regulators and ligands have been measured. As reported above, apparent equilibrium and dissociation rate constants of 5 μM and 2 s^{-1},

respectively, were obtained for the interaction between PXR-LBD and SRC-1 (676 – 700) both in the presence and absence of rifampicin. This measured apparent equilibrium dissociation constant is at the weak end of the spectrum of affinities measured for nuclear receptors, many of which fall in the nanomolar range. Fluorescence polarization assays of full length SRC-1 interacting with the full length estrogen receptor (ER) and ER-LBD in the presence of estrogen yielded a K_d of ~ 30 nM on both occasions (*37*). In the absence of ligand, no interaction was observed. Equilibrium constants of full length ER and another member of the steroid receptor co-activator family, SRC-2, interacting in live cells have been estimated using fluorescence cross-correlation spectroscopy. Estimated K_d values of ~200 nM, < 6 nM and > 3 μM were obtained for ER/SRC-2 in the apo-, agonist-bound and antagonist-bound states, respectively (*38*). Equilibrium constants of ~160 nM were obtained for the thyroid receptor LBD interacting with a SRC-2 fragment in the presence of thyroxin (*39, 40*). Surface plasmon resonance yielded an apparent dissociation rate constant on the order of 1×10^{-2} s^{-1} for this interaction (*40*). However, a recent study showed that the glucocorticoid receptor (GR), like PXR, binds many co-regulator peptides with micromolar affinity in the presence of the GR agonist, dexamethasone (*41*). Further studies have shown that another receptor, the peroxisome proliferator-activated receptor-γ (PPARγ), is able to bind SRC-1 in the absence of ligand with an equilibrium dissociation constant of 34.2 μM (*42*). Addition of a ligand did increase the affinity of PPARγ and SRC-1, and a K_d of 0.96 μM was obtained. The ability of both PXR and PPARγ to bind co-activators in the absence of ligand may account for their relatively high level of basal activity. FRET measurements have been used to look at the interaction between full length, human PXR and the same 25 amino

acid fragment of SRC-1 used in the present study, as a function of the rifampicin concentration (*43*). While the assay did not yield equilibrium dissociation constants for PXR and SRC-1, it did show, contrary to our findings, that rifampicin slightly, but within experimental uncertainty, increased co-activator recruitment. We cannot yet account for this discrepancy.

The structures of LBDs are conserved among the various members of the nuclear receptor superfamily (*44*, *45*). Briefly, nuclear receptor LBDs consist of approximately twelve α-helices arranged into three layers and two to five β-strands that line a side of the ligand binding pocket. The ligand binding pocket exists as a cavity on one side of the LBD and is lined primarily by hydrophobic residues from several α-helices and β-strands. The co-activator binding site consists of a hydrophobic groove on the surface of the LBD, created by α helices 3, 4 and 12 in PXR.

Crystal structures of nuclear receptors in the apo- and agonist- bound states have contributed to an existing molecular model of ligand-mediated interaction between nuclear receptors and co-activators. A crystal structure of the retinoid acid receptor in the apo-state showed helix 12 (H12), or activation function-2 (AF-2), extended away from the main body of the LBD (*9*), whereas subsequent structures of ligand-bound nuclear receptor LBDs showed H12 folded against the body of the LBD (*10, 11*). In this folded conformation, LBDs can bind conserved LXXLL motifs in co-activators via a charge clamp (*11*). Therefore, it is thought that H12 serves as the molecular switch that is modulated by ligands to promote nuclear receptor interaction with co-activators. PXR-LBD was co-crystallized with the same 25 amino acid fragment of SRC-1 (residues 676-700) used in this study, and the agonist SR12813 (*12*). The SRC-1 fragment formed a

kinked α-helix and bound to a groove on the surface of PXR-LBD created by helices H3, H4 and H12. Two polar contacts between PXR-LBD and SRC-1 [K259 (H3): carbonyl oxygen L694; E427 (H12): amine nitrogen I689] constituted the charge clamp that has also been observed in other nuclear receptor/co-activator complexes. In addition, a hydrogen bond was formed between K227 (H4) and H687. This lysine residue is also conserved in other nuclear receptors, including the constitutive androstane, liver X, farnesoid X and vitamin D receptors.

Crystal structures of ligand-bound nuclear receptors have helped elucidate the manner in which many endogenous ligands stabilize H12 in the folded or active conformation. It appears that a canonical π-cation interaction stabilizes H12 in the folded state in the steroid hormone receptors (*46*), which encompass the glucocorticoid, mineralcorticoid, progesterone, androgen and estrogen receptors, as well as in other nuclear receptors, including the vitamin D, thyroid hormone, farnesoid X and liver X receptors (*47*). In the non-steroid hormone receptors, an oxygen atom from each receptor's endogenous ligand forms an electrostatic interaction with a conserved histidine in H10 or H11, which in turn makes π-cation interactions with a conserved tryptophan or phenylalanine in H12. In this way, ligands of many nuclear receptors indirectly stabilize H12 in the active conformation. However, it is not immediately clear from crystal structures of ligand-bound PXR-LBD how agonists might stabilize PXR's H12 in the folded state. PXR ligands are structurally diverse and appear to lack a common chemical feature that could stabilize the active conformation. Furthermore, attempts to design an antagonist directed at the PXR ligand binding pocket have thus far failed, with many of the proposed compounds instead serving as agonists (*48*). It appears that any compound

that binds PXR's ligand binding pocket serves to activate the receptor. (Compounds that antagonize PXR by competing with co-activators to bind the receptor have been described (*27, 31*).) Therefore, it is likely that PXR ligands do not directly stabilize the active conformation and increase the receptors's affinity for co-activators, but instead work through an alternate mechanism to upregulate PXR activity.

A crystal structure of apo-PXR-LBD shows H12 in the active conformation, indicating that the folded state may be favored even in the absence of ligand (*25*). If the active conformation is energetically favored in the apo-state, that fact could explain our observation that PXR-LBD interacts with the SRC-1 fragment in a ligand-independent manner. Furthermore, PXR has a high level of basal activity relative to other nuclear receptors (*49*), indicating that the receptor maybe able to adopt a stable active conformation in the absence of ligand. In support of this conclusion, molecular dynamics simulations on PXR have shown that the AF-2 region of the receptor moves as a correlated unit in the absence of ligands (*50*).

PXR is somewhat unique because it binds promiscuously to structurally diverse ligands. In fact, ligands that range in molecular weight from 232 (phenobarbitol) to 823 (rifampicin) have been shown to activate PXR. A 60 amino acid insert found in PXR-LBD that serves to create a 5-stranded β sheet lining one side of the ligand binding pocket, as opposed to the 2- or 3-stranded β sheet seen in other nuclear receptors, is thought to contribute to a large, flexible ligand binding pocket that enables PXR to accommodate diverse ligands (*25*). The ligand binding pocket can range in volume from 1150 $Å^3$ in the apo-state (*25*) to ~1900 $Å^3$ with rifampicin bound (*7*). Such a large cavity in the body of this globular protein may serve to destabilize apo-PXR. Ligand binding

may increase the stability of PXR and thereby its lifetime *in vivo*. Ligand-dependent activation of PXR might then be a consequence of the increased stability of ligand-bound receptor.

Nonetheless, studies of the interaction between PXR and SRC-1 in cells suggest that the interaction is enhanced in the presence of ligands. *In vitro* co-precipitation assays of bacterially expressed GST-tagged PXR-LBD and a [^{35}S]-labeled SRC-1 fragment, containing the co-activator's receptor interaction domain (RID), showed a weakly enhanced interaction in the presence of various agonists, including rifampicin (*5*, *51*). It is worth noting that the corresponding interaction between a GST-tagged LBD of the estrogen receptor (ER) and radio-labeled SRC-1-RID was much more greatly enhanced in the presence of estradiol (*51*). Mammalian two-hybrid assays have also demonstrated a ligand-dependent interaction for SRC-1-RID and PXR, with similar results being obtained for both full length PXR and PXR-LBD (*31*, *52*). Indeed these studies were conducted with SRC-1-RID, which contains three LXXLL motifs, as opposed to the 25 amino acid fragment used in this study, which only has one LXXLL motif, albeit the most strongly interacting one (*53*). However, yeast two-hybrid assays have shown that co-activator fragments as small as eight amino acids, containing a single LXXLL motif, are able to interact with ER-LBD in a ligand-dependent manner (*54*). Therefore, it is unlikely that our observation that the interaction between PXR-LBD and the SRC-1 fragment is rifampicin-independent is due to the use of a 25 amino acid fragment of SRC-1, as opposed to the use of a larger fragment or the full length protein which is 1441 residues long. It is possible that the observed ligand-dependence in the *in vivo* biochemical assays is due to an increased stability of ligand-bound PXR.

Thermal denaturation studies using circular dichroism spectropolarimetry have shown that ligands do stabilize PXR-LBD. Melting temperatures of 43.0 ± 0.08 (*12*), 48.4 ± 0.05 (*12*) and 46.5 ± 0.05 °C (*55*) were obtained for apo-, SR12813-bound and rifampicin-bound PXR-LBD, respectively. A complex of SRC-1 and PXR-LBD had a melting temperature of 48.2 ± 0.08 °C (*12*). These results show that agonists and co-activator each serve to stabilize PXR-LBD. Ternary complexes of PXR-LBD and SRC-1 with either SR12813 or rifampicin were even more stable with melting temperatures of 52.5 ± 0.05 (*12*) and 52.6 ± 0.03 °C, respectively. One might expect that this increase in stability upon addition of the third component would mean that the agonist and co-activator bind co-operatively, resulting in a ligand-dependent increase in affinity for the co-activator and vice versa. However, if the increased thermal stability is due to rifampicin and SRC-1 independently stabilizing different regions of PXR-LBD, binding of one may not increase the receptor's affinity for the other.

Another possibility is that ligand-dependent activation of PXR occurs through a novel pathway that is as yet uncharacterized. A recent study demonstrated that the nuclear receptor peroxisome proliferator-activated receptor-γ (PPARγ) is activated by structurally diverse serotonin and fatty acid metabolites (*42*). PPARγ, like PXR, has a flexible ligand binding pocket that can accommodate many different endogenous and exogenous ligands. Crystal structures of PPARγ in complex with a mimic of serotonin metabolites, indomethacin (IDM), showed that it bound in a distinct region of the ligand binding pocket and made direct contact with H12, securing the helix in the active conformation. However, fatty acid metabolites bound away from H12 and failed to make any contact with the helix. Surface plasmon resonance studies showed IDM induced

PPARγ to recruit SRC-1. In fact, equilibrium dissociation constants of 34.2 μM and 0.96 μM were obtained for PPARγ and SRC-1 in the absence and presence of IDM, respectively. While IDM brought about a thirty-fold increase in the affinity of PPARγ for SRC-1, the fatty acid metabolite, nitro-233, failed to enhance the interaction between the receptor and co-activator. Instead, it was proposed that nitro-233 may modulate heterodimerization with the retinoid X receptor. Given the structural diversity of PXR ligands, agonists like rifampicin may very well use different pathways to activate PXR.

Another aspect related to nuclear receptor function is the previous observation that many receptors have the capability of forming homodimers or heterodimers with other nuclear receptors. In the case of PXR, the physiologically relevant receptor dimer is thought to be one with RXR. Nonetheless, a previous work has shown that PXR-LBD homodimerizes *in vitro* with an equilibrium dissociation constant of 4.5 μM (*26*). A dimerization-null mutant was found to be incapable of binding SRC-1 peptide either in the presence or absence of ligand. However, this result is not completely consistent with a separate report in which ligand-dependent SRC-1 peptide interaction with PXR-LBD was observed *in vitro* for a receptor concentration of 20 nM (*43*), well below the K_d for dimerization where one would predict that the PXR-LBD was present almost exclusively in monomeric form. One possibility is that the discrepancy arises in an indirect manner as a consequence of the mutations introduced to form the dimerization-null PXR-LBD. Independent of these results, it is important to address the question of the state of dimerization of the PXR-LBD used in the work reported herein. The solution concentration before application to the surface was 0.1 mg/mL = 2.6 μM; thus, the previously measured dimerization K_d would imply that the solutions contained primarily

monomeric PXR-LBD with a non-negligible fraction of dimeric PXR-LBD. It is not possible to determine, after application to the surfaces and washing, what fraction of the immobilized PXR-LBD was in monomeric or dimeric form. Nonetheless, the results show clearly that the SRC-1 peptide does specifically and reversibly interact with at least a fraction of the immobilized PXR-LBD. Definitive conclusions about the interaction of SRC-1 peptides with monomeric and dimeric forms of PXR-LBD await further measurements.

The interaction between co-repressors and nuclear receptors, particularly PXR, has not been as extensively studied as that between co-activators and nuclear receptors. Certainly, the authors are unaware of any biophysical studies of PXR and its co-repressors. Instead, cell-based assays have been used to show that the SMRT-RID specifically interacts with PXR, while that of NCoR does not (*13*). Hence, the present finding that the peptide derived from SMRT binds PXR-LBD with greater affinity (K_d' = ~ 70 μM) than the NCoR fragment (K_d' = ~ 170 μM), is consistent with what has been reported in the literature. Only one of two interaction domains (LXXXIXXXL; ID1 and ID2), ID2, in the SMRT-RID was shown to actually bind PXR (*14*). In addition, of the two major SMRT splicing isoforms, α and τ, ID2 derived from SMRTα was found to bind preferentially to PXR (*15*). Compared to SMRTτ, SMRTα contains a 46 amino acid insert immediately downstream of ID2. For the purposes of the present study, a peptide containing ID2 from SMRTα was used. Reporter assays showed that SMRT (α and τ) reduces both the basal and rifampicin-induced transcriptional activity of PXR on the CYP3A4 promoter (*13, 14*). These results indicate that SMRT is able to compete with

co-activators to bind PXR both in the absence and presence of ligand, and thereby reduce the receptor's transcriptional activity.

In addition to the fact that SMRTα binds preferentially to PXR, it has been shown that SMRTα resists rifampicin-induced dissociation from PXR (*15*), while SMRTτ does not (*14*). These results are consistent with our observation that the co-repressor peptide derived from SMRTα binds PXR-LBD with equal affinity both in the presence and absence of rifampicin. However, the measured equilibrium dissociation constant of SMRTα (2337-2358) and PXR-LBD, which averages to ~ 70 μM over the three rifampicin concentrations (see Table 3.2), is quite weak. In comparison, fluorescence polarization measurements of the thyroid hormone receptor-β LBD and SMRTα (2329-2358) yielded equilibrium dissociation constants of ~ 1 μM (*16*). It is unclear whether a larger fragment of SMRTα would have interacted with PXR-LBD with greater affinity. However, if the measured equilibrium constant is accurate, the interaction between SMRTα and PXR-LBD may not be physiologically relevant. It is possible that there are other co-repressors that interact with PXR with higher affinity and in a ligand-dependent manner.

Crystal structures of nuclear receptor LBDs and peptide fragments of SMRT have revealed the mode of co-repressor binding, and thereby elucidated the reason for the competition between co-repressors and co-activators to bind nuclear receptors. A crystal structure of a PPAR isoform, PPARα, LBD in complex with an antagonist, GW490544, and the same peptide fragment of SMRTα (2337-2358) that was used in the present work, showed that the co-repressor bound to a hydrophobic groove on the surface of the LBD that overlapped with the co-activator binding site (*16*). GW490544, like many nuclear

receptor antagonists, had a portion that protruded out from the ligand binding pocket and prevented H12 (AF-2) from assuming its active conformation. This repositioning of H12 allowed the co-repressor peptide to bind a groove formed by H3, H3', H4 and H5. In the ternary complex, SMRT adopted a three-turn α-helix, unlike the two-turn α-helix formed by SRC-1. The additional helical turn in SMRT extended into the space that is normally occupied by H12 in the active conformation. The co-repressor/PPAR-α complex was stabilized by polar contacts between the backbone carbonyls of A2348 and L2349 and the amine nitrogen of the same, conserved lysine residue in H3 that helps form the charge clamp with co-activators. Since the co-activator and co-repressor binding-sites overlap so greatly, one of these co-regulators binding a nuclear receptor would necessarily prevent the other from binding. In the apo-state, when H12 is allowed to freely sample active and inactive conformations, one would expect co-activators and co-repressors to compete with each other to bind nuclear receptors. If in fact rifampicin fails to secure H12 in the active conformation, as is implied by existing structural data and the present thermodynamic and kinetic data for SRC-1/PXR-LBD interactions, one would expect, as observed, that rifampicin does not affect the ability of co-repressors to bind PXR-LBD.

The present thermodynamic and kinetic measurements indicate that rifampicin does not increase the affinity of PXR-LBD for the SRC-1 fragment, or decrease the receptor's affinity for SMRT. The vast structural diversity of PXR ligands makes it unlikely that all agonists would be able to form direct or indirect interactions with residues in H12, as seen with the π-cation interactions, to stabilize the active conformation. It is possible that the different PXR ligands work through an alternate mechanism, or even several mechanisms like in the case with PPARγ, to activate the

receptor. One such possibility is that ligands, by filling the large cavity that is the ligand binding pocket, confer stability to PXR and increase the receptor's *in vivo* lifetime. Other plausible ligand-dependent regulatory mechanisms include an interplay between (physiologically relevant) co-repressors and co-activators, homodimerization or heterodimerization with RXR, phosphorylation, and the differential affinity of PXR for various chaperone proteins in the ligand-bound versus apo- states. These possible mechanisms of action are all avenues for future study.

3.7 Acknowledgments

We thank Linda L. Spremulli, Brooke E. Christian, Valerie Hansen, Laurie Betts, Kaiulani Houston, Marcey Waters, Qunzhao Wang, David Lawrence, Yuan Cheng and Xiang Wang for their assistance.

3.8 References

1. di Masi, A., De Marinis, E., Ascenzi, P., and Marino, M. (2009) Nuclear receptors CAR and PXR: Molecular, functional, and biomedical aspects, *Mol. Asp. Med. 30*, 297-343.

2. Moore, L. B., Goodwin, B., Jones, S. A., Wisely, G. B., Serabjit-Singh, C. J., Willson, T. M., Collins, J. L., and Kliewer, S. A. (2000) St. John's wort induces hepatic drug metabolism through activation of the pregnane X receptor, *Proceedings of the National Academy of Sciences 97*, 7500-7502.

3. Wentworth, J., Agostini, M., Love, J., Schwabe, J., and Chatterjee, V. (2000) St John's wort, a herbal antidepressant, activates the steroid X receptor, *Journal of Endocrinology 166*, R11-R16.

4. Watkins, R. E., Maglich, J. M., Moore, L. B., Wisely, G. B., Noble, S. M., Davis-Searles, P. R., Lambert, M. H., Kliewer, S. A., and Redinbo, M. R. (2003) 2.1 Å crystal structure of human PXR in complex with the St. John's Wort compound hyperforin, *Biochemistry 42*, 1430-1438.

5. Lehmann, J. M., McKee, D. D., Watson, M. A., Willson, T. M., Moore, J. T., and Kliewer, S. A. (1998) The human orphan nuclear receptor PXR is activated by compounds that regulate CYP3A4 gene expression and cause drug interactions, *The Journal of Clinical Investigation 102*, 1016-1023.

6. Bertilsson, G., Heidrich, J., Svensson, K., Åsman, M., Jendeberg, L., Sydow-Bäckman, M., Ohlsson, R., Postlind, H., Blomquist, P., and Berkenstam, A. (1998) Identification of a human nuclear receptor defines a new signaling pathway for CYP3A induction, *Proceedings of the National Academy of Sciences 95*, 12208-12213.

7. Chrencik, J. E., Orans, J., Moore, L. B., Xue, Y., Peng, L., Collins, J. L., Wisely, G. B., Lambert, M. H., Kliewer, S. A., and Redinbo, M. R. (2005) Structural Disorder in the Complex of Human Pregnane X Receptor and the Macrolide Antibiotic Rifampicin, *Mol. Endocrinol. 19*, 1125-1134.

8. Nagy, L., and Schwabe, J. W. R. (2004) Mechanism of the nuclear receptor molecular switch, *Trends in Biochemical Sciences 29*, 317-324.

9. Bourguet, W., Ruff, M., Chambon, P., Gronemeyer, H., and Moras, D. (1995) Crystal structure of the ligand-binding domain of the human nuclear receptor RXR-[alpha], *Nature 375*, 377-382.

10. Renaud, J.-P., Rochel, N., Ruff, M., Vivat, V., Chambon, P., Gronemeyer, H., and Moras, D. (1995) Crystal structure of the RAR-[gamma] ligand-binding domain bound to all-trans retinoic acid, *Nature 378*, 681-689.

11. Nolte, R. T., Wisely, G. B., Westin, S., Cobb, J. E., Lambert, M. H., Kurokawa, R., Rosenfeld, M. G., Willson, T. M., Glass, C. K., and Milburn, M. V. (1998) Ligand binding and co-activator assembly of the peroxisome proliferator-activated receptor-[gamma], *Nature 395*, 137-143.

12. Watkins, R. E., Davis-Searles, P. R., Lambert, M. H., and Redinbo, M. R. (2003) Coactivator binding promotes the specific interaction between ligand and the pregnane X receptor, *Journal of Molecular Biology 331*, 815-828.

13. Takeshita, A., Taguchi, M., Koibuchi, N., and Ozawa, Y. (2002) Putative Role of the Orphan Nuclear Receptor SXR (Steroid and Xenobiotic Receptor) in the Mechanism of CYP3A4 Inhibition by Xenobiotics, *J. Biol. Chem. 277*, 32453-32458.

14. Johnson, D. R., Li, C.-W., Chen, L.-Y., Ghosh, J. C., and Chen, J. D. (2006) Regulation and Binding of Pregnane X Receptor by Nuclear Receptor Corepressor Silencing Mediator of Retinoid and Thyroid Hormone Receptors (SMRT), *Molecular Pharmacology 69*, 99-108.

15. Li, C.-W., Dinh, G. K., and Chen, J. D. (2009) Preferential Physical and Functional Interaction of Pregnane X Receptor with the SMRTα Isoform, *Molecular Pharmacology 75*, 363-373.

16. Xu, H. E., Stanley, T. B., Montana, V. G., Lambert, M. H., Shearer, B. G., Cobb, J. E., McKee, D. D., Galardi, C. M., Plunket, K. D., Nolte, R. T., Parks, D. J., Moore, J. T., Kliewer, S. A., Willson, T. M., and Stimmel, J. B. (2002) Structural basis for antagonist-mediated recruitment of nuclear co-repressors by PPAR[alpha], *Nature 415*, 813-817.

17. Pisarchick, M. L., and Thompson, N. L. (1990) Binding of a monoclonal antibody and its Fab fragment to supported phospholipid monolayers measured by total internal reflection fluorescence microscopy, *Biophys. J. 58*, 1235-1249.

18. Hsieh, V., H., Poglitsch, L., C., Thompson, and L., N. (1992) Direct measurement of the weak interactions between a moue Fc receptor (Fcgamma RII) and IgG1 in the absence and presence of hapten: A total internal reflection fluorescence microscopy study, *Biochemistry 31*, 11562-11566.

19. Gesty-Palmer, D., and Thompson, N. L. (1997) Binding of the soluble, truncated form of an Fc receptor (mouse FcγRII) to membrane-bound IgG as measured by total internal reflection fluorescence microscopy, *Journal of Molecular Recognition 10*, 63-72.

20. Jung, H., Yang, T., Lasagna, M. D., Shi, J., Reinhart, G. D., and Cremer, P. S. (2008) Impact of Hapten Presentation on Antibody Binding at Lipid Membrane Interfaces, *Biophys. J. 94*, 3094-3103.

21. Pisarchick, M. L., Gesty, D., and Thompson, N. L. (1992) Binding kinetics of an anti-dinitrophenyl monoclonal Fab on supported phospholipid monolayers

measured by total internal reflection with fluorescence photobleaching recovery, *Biophys. J. 63*, 215-223.

22. Pearce, K. H., Hiskey, R. G., and Thompson, N. L. (1992) Surface binding kinetics of prothrombin fragment 1 on planar membranes measured by total internal reflection fluorescence microscopy, *Biochemistry 31*, 5983-5995.

23. Sund, S. E., and Axelrod, D. (2000) Actin Dynamics at the Living Cell Submembrane Imaged by Total Internal Reflection Fluorescence Photobleaching, *Biophys. J. 79*, 1655-1669.

24. Jones, S. A., Moore, L. B., Shenk, J. L., Wisely, G. B., Hamilton, G. A., McKee, D. D., Tomkinson, N. C. O., LeCluyse, E. L., Lambert, M. H., Willson, T. M., Kliewer, S. A., and Moore, J. T. (2000) The pregnane X receptor: A promiscuous xenobiotic receptor that has diverged during evolution, *Mol. Endocrinol. 14*, 27-39.

25. Watkins, R. E., Wisely, G. B., Moore, L. B., Collins, J. L., Lambert, M. H., Williams, S. P., Willson, T. M., Kliewer, S. A., and Redinbo, M. R. (2001) The human nuclear xenobiotic receptor PXR: Structural determinants of directed promiscuity, *Science 292*, 2329-2333.

26. Noble, M., S., Carnahan, E., V., Moore, B., L., Luntz, Tom, Wang, H., Ittoop, R., O., Stimmel, B., J., Davis-Searles, R., P., Watkins, E., R., Wisely, Bruce, G., Lecluyse, Ed, Tripathy, Ashutosh, Mcdonnell, P., D., Redinbo, and R., M. (2006) Human PXR forms a tryptophan zipper-mediated homodimer, *Biochemistry 45*, 8579-8589.

27. Wang, H., Li, H., Moore, L. B., Johnson, M. D. L., Maglich, J. M., Goodwin, B., Ittoop, O. R. R., Wisely, B., Creech, K., Parks, D. J., Collins, J. L., Willson, T. M., Kalpana, G. V., Venkatesh, M., Xie, W., Cho, S. Y., Roboz, J., Redinbo, M., Moore, J. T., and Mani, S. (2008) The phytoestrogen coumestrol Is a naturally occurring antagonist of the human pregnane X receptor, *Mol. Endocrinol. 22*, 838-857.

28. Slade, K. M., Steele, B. L., Pielak, G. J., and Thompson, N. L. (2009) Quantifying green fluorescent protein diffusion in Escherichia coli by using continuous photobleaching with evanescent illumination, *The Journal of Physical Chemistry B 113*, 4837-4845.

29. Lagerholm, B. C., Starr, T. E., Volovyk, Z. N., and Thompson, N. L. (2000) Rebinding of IgE Fabs at haptenated planar membranes: Measurement by total internal reflection with fluorescence photobleaching Recovery, *Biochemistry 39*, 2042-2051.

30. Hsieh, V., H., Thompson, and L., N. (1995) Dissociation kinetics between a mouse FC receptor (FCGAMMA RII) and IgG : Measurement by total internal reflection with fluorescence photobleaching recovery, *Biochemistry 34*, 12481-12488.

31. Huang, H., Wang, H., Sinz, M., Zoeckler, M., Staudinger, J., Redinbo, M. R., Teotico, D. G., Locker, J., Kalpana, G. V., and Mani, S. (2007) Inhibition of drug metabolism by blocking the activation of nuclear receptors by ketoconazole, *Oncogene 26*, 258-268.

32. Xiao, L., Nickbarg, E., Wang, W., Thomas, A., Ziebell, M., Prosise, W. W., Lesburg, C. A., Taremi, S. S., Gerlach, V. L., Le, H. V., and Cheng, K. C. (2011) Evaluation of in vitro PXR-based assays and in silico modeling approaches for understanding the binding of a structurally diverse set of drugs to PXR, *Biochemical Pharmacology 81*, 669-679.

33. Pero, J. K., Haas, E. M., and Thompson, N. L. (2006) Size dependence of protein diffusion very close to membrane surfaces: Measurement by total internal reflection with fluorescence correlation spectroscopy, *The Journal of Physical Chemistry B 110*, 10910-10918.

34. Thompson, N. L., Burghardt, T. P., and Axelrod, D. (1981) Measuring surface dynamics of biomolecules by total internal reflection fluorescence with photobleaching recovery or correlation spectroscopy, *Biophys. J. 33*, 435-454.

35. Thompson, N. L., Navaratnarajah, P., and Wang, X. (2010) Measuring surface binding thermodynamics and kinetics by using total internal reflection with fluorescence correlation spectroscopy: Practical considerations, *The Journal of Physical Chemistry B 115*, 120-131.

36. Carnahan, V. E., and Redinbo, M. R. (2005) Structure and Function of the Human Nuclear Xenobiotic Receptor PXR, *Current Drug Metabolism 6*, 357-367.

37. Margeat, E., Poujol, N., Boulahtouf, A., Chen, Y., Müller, J. D., Gratton, E., Cavailles, V., and Royer, C. A. (2001) The human estrogen receptor [alpha] dimer binds a single SRC-1 coactivator molecule with an affinity dictated by agonist structure, *Journal of Molecular Biology 306*, 433-442.

38. Savatier, J., Jalaguier, S. p., Ferguson, M. L., Cavaillès, V., and Royer, C. A. (2009) Estrogen receptor interactions and dynamics monitored in live cells by fluorescence cross-correlation spectroscopy, *Biochemistry 49*, 772-781.

39. Arnold, L. A., Estébanez-Perpiñá, E., Togashi, M., Jouravel, N., Shelat, A., McReynolds, A. C., Mar, E., Nguyen, P., Baxter, J. D., Fletterick, R. J., Webb, P., and Guy, R. K. (2005) Discovery of Small Molecule Inhibitors of the Interaction of the Thyroid Hormone Receptor with Transcriptional Coregulators, *J. Biol. Chem. 280*, 43048-43055.

40. Valadares, N. F., Polikarpov, I., and Garratt, R. C. (2008) Ligand induced interaction of thyroid hormone receptor beta with its coregulators, *The Journal of Steroid Biochemistry and Molecular Biology 112*, 205-212.

41. Pfaff, S. J., and Fletterick, R. J. (2010) Hormone and co-regulator binding to the glucocorticoid receptor are allosterically coupled, *J. Biol. Chem.*

42. Waku, T., Shiraki, T., Oyama, T., Maebara, K., Nakamori, R., and Morikawa, K. (2010) The nuclear receptor PPAR[gamma] individually responds to serotonin- and fatty acid-metabolites, *EMBO J 29*, 3395-3407.

43. Mitro, N., Vargas, L., Romeo, R., Koder, A., and Saez, E. (2007) T0901317 is a potent PXR ligand: Implications for the biology ascribed to LXR, *FEBS Lett. 581*, 1721-1726.

44. Ingraham, H. A., and Redinbo, M. R. (2005) Orphan nuclear receptors adopted by crystallography, *Current Opinion in Structural Biology 15*, 708-715.

45. Moore, J. T., Collins, J. L., and Pearce, K. H. (2006) The Nuclear Receptor Superfamily and Drug Discovery, *ChemMedChem 1*, 504-523.

46. Queralt-Rosinach, N., and Mestres, J. (2010) A canonical cation–π interaction stabilizes the agonist conformation of estrogen-like nuclear receptors, *European Biophysics Journal 39*, 1471-1475.

47. Huang, P., Chandra, V., and Rastinejad, F. (2010) Structural overview of the nuclear receptor superfamily: Insights into physiology and therapeutics, *Annual Review of Physiology 72*, 247-272.

48. Xue, Y., Chao, E., Zuercher, W. J., Willson, T. M., Collins, J. L., and Redinbo, M. R. (2007) Crystal structure of the PXR-T1317 complex provides a scaffold to examine the potential for receptor antagonism, *Bioorganic & Medicinal Chemistry 15*, 2156-2166.

49. Goodwin, B., Redinbo, M. R., and Kliewer, S. A. (2002) Regulation of CYP3A gene transcription by the pregnane X receptor, *Annual Review of Pharmacology and Toxicology 42*, 1-23.

50. Teotico, D. G., Frazier, M. L., Ding, F., Dokholyan, N. V., Temple, B. R. S., and Redinbo, M. R. (2008) Active Nuclear Receptors Exhibit Highly Correlated AF-2 Domain Motions, *PLoS Comput Biol 4*, e1000111.

51. Kliewer, S. A., Moore, J. T., Wade, L., Staudinger, J. L., Watson, M. A., Jones, S. A., McKee, D. D., Oliver, B. B., Willson, T. M., Zetterström, R. H., Perlmann, T., and Lehmann, J. M. (1998) An orphan nuclear receptor activated by pregnanes defines a novel steroid signaling pathway, *Cell 92*, 73-82.

52. Wang, H., Huang, H., Li, H., Teotico, D. G., Sinz, M., Baker, S. D., Staudinger, J., Kalpana, G., Redinbo, M. R., and Mani, S. (2007) Activated pregnenolone X receptor Is a target for ketoconazole and its analogs, *Clinical Cancer Research 13*, 2488-2495.

53. Darimont, B. D., Wagner, R. L., Apriletti, J. W., Stallcup, M. R., Kushner, P. J., Baxter, J. D., Fletterick, R. J., and Yamamoto, K. R. (1998) Structure and specificity of nuclear receptor–coactivator interactions, *Genes & Development 12*, 3343-3356.

54. Heery, D. M., Kalkhoven, E., Hoare, S., and Parker, M. G. (1997) A signature motif in transcriptional co-activators mediates binding to nuclear receptors, *Nature 387,* 733-736.

55. Carnahan, V. E. (2007) 'Characterizing the pregnane X receptor's interactions and biophysical properties,' MS Thesis, University of North Carolina, Chapel Hill, NC, USA.

Chapter 4

FcγRII and IgG Interactions: A Test System for TIR-FCS

4.1 Introduction

Total internal reflection fluorescence microscopy combined with fluorescence correlation spectroscopy (TIR-FCS) is a novel technique that provides quantitative information about the behavior of fluorescent molecules at or near the interface between a solid transparent substrate and aqueous medium (*1*). In an application of the technique, TIR-FCS was used to examine the reversible association of a fluorescent species with surface-immobilized receptors. Specifically, the kinetic parameters of fluorescently labeled mouse antibodies (IgG) interacting with Fc receptors (FcγRII) reconstituted in supported planar bilayers were measured using TIR-FCS (*2*). When conducting these measurements, Lieto et al. (*2*) used low concentrations (~10 nM) of the fluorescent antibody (F-IgG) to obtain fluorescence fluctuations that were sufficiently large to be accurately measured. However, 10 nM F-IgG is far below the midpoint (~1 μM) of the IgG/FcγRII binding isotherm. To avoid possible rare, tight, nonspecific binding events, the effects of which could be unduly prominent at such low concentrations, F-IgG was mixed with unlabeled IgG to a final concentration of 1 μM. In deriving a general TIR-FCS expression to describe such a system (one in which fluorescent and nonfluorescent ligands compete to bind surface-bound receptors), Lieto and Thompson (*3*) showed that

at long correlation-lag times, τ, TIR-FCS curves, in theory, contain kinetic information about the nonfluorescent species.

As in Chapter 2, we sought to determine experimental conditions that might yield autocorrelation curves containing significant kinetic information about both the fluorescent ligand and a nonfluorescent competitor that is distinct from the labeled ligand. To test these conditions, we set out to establish a model system consisting of an IgG, immobilized via its antigen binding site to a supported planar bilayer, a fluorescently labeled, soluble, extracellular portion of FcγRII (F-sFcγRII) and a peptide derived from the IgG binding site on FcγRII that would serve as the nonfluorescent competitor. As mentioned in the previous Chapter, the pregnane X receptor and its interacting partners, which were initially meant to serve as a test system for the nonfluorescent effector theory, turned out to be well suited for the testing of the nonfluorescent competitor theory. Nevertheless, the soluble FcγRII and IgG can still be used to test the experimental conditions detailed in Chapter 2 that were predicted to yield autocorrelation curves containing significant information about the thermodynamic and kinetic parameters pertaining to the interaction between a single, fluorescent ligand and surface-bound receptor.

4.1.1 Theoretical Background

Lieto and Thompson (*3*) showed that, theoretically, TIR-FCS can be used to detect the cross-talk between fluorescent and nonfluorescent species as they compete for surface binding sites. In our system, nonfluorescent competitors, L_c, compete with fluorescently labeled reporter-ligands, L_f, to reversibly bind immobile surface binding sites, *B*, as shown below.

$$L_f + B \underset{k_{-1}}{\overset{k_1}{\rightleftharpoons}} C_f \qquad L_c + B \underset{k_{-2}}{\overset{k_2}{\rightleftharpoons}} C_c \tag{4.1}$$

$$K_1 = \frac{k_1}{k_{-1}} \qquad K_2 = \frac{k_2}{k_{-2}}$$

Lieto and Thompson (*3*) derived a general expression for G(τ) in terms of the rate of diffusion of the fluorescent ligand through the evanescent wave, and the association and dissociation rate constants of both the fluorescent reporter-ligand and nonfluorescent competitor. When the rate of diffusion through the evanescent field is much larger than the surface association and dissociation rate constants, as is often the case, the autocorrelation function separates into two components:

$$G(\tau) = G_a(\tau) + G_s(\tau), \tag{4.2}$$

where $G_a(\tau)$ pertains to fluorescence fluctuations due to diffusion through the evanescent field, and $G_s(\tau)$ contains information about the surface association and dissociation kinetics (*3*). $G_a(\tau)$ is given by

$$G_a(\tau) = G_a(0)\left\{(1-2R_z\tau)w\left[i(R_z\tau)^{1/2}\right] + 2\left(\frac{R_z\tau}{\pi}\right)^{1/2}\right\} \tag{4.3}$$

where $w(\xi) = \exp(-\xi^2)\mathrm{erfc}(-i\xi)$ and

$$G_a(0) = \frac{dK_1(1+X_f+X_c)^2}{2\pi h^2 X_f\left[K_1 S + d(1+X_f+X_c)\right]^2}, \tag{4.4}$$

with $X_f = K_1[L_f]$ and $X_c = K_2[L_c]$. R_z is the rate of diffusion of the fluorescent reporter-ligand through the evanescent field: $R_z = D_f / d^2$. D_f is the diffusion constant of the fluorescent ligand, d is the depth of the evanescent field and h is the radius of the

observed area in the sample plane as defined by the pin hole. S is the total density of surface binding sites.

At the reaction limit (*3-5*) when the likelihood of rebinding to the surface after dissociation is low (6), we find that

$$G_s(\tau) = G_s(0)\left(s_1 e^{-\lambda_1 \tau} + s_2 e^{-\lambda_2 \tau}\right), \tag{4.5}$$

where

$$G_s(0) = \frac{K_1^2 S(1+X_c)}{\pi h^2 X_f \left[K_1 S + d\left(1+X_f+X_c\right)\right]^2}. \tag{4.6}$$

The amplitudes, s_1 and s_2, and the rates, λ_1 and λ_2, are a function of the solution concentration and surface association and dissociation rate constants of fluorescent and nonfluorescent molecules. The amplitudes are given by

$$s_1 = \frac{1}{2} + \frac{(X_c - 1)X_f - (1+X_c) + \alpha(1+X_c)^2}{2(1+X_c)\beta} \tag{4.7}$$

and

$$s_2 = 1 - s_1 = \frac{1}{2} - \frac{(X_c - 1)X_f - (1+X_c) + \alpha(1+X_c)^2}{2(1+X_c)\beta}, \tag{4.8}$$

where

$$\alpha = \frac{k_{-2}}{k_{-1}}; \tag{4.9}$$

$$\beta = \sqrt{(1+X_f+\alpha+\alpha X_c)^2 - 4\alpha(1+X_f+X_c)}. \tag{4.10}$$

The rates are given by

$$\lambda_{1,2} = \frac{1}{2}\left(k_1[L_f] + k_2[L_c] + k_{-1} + k_{-2}\right) \mp \frac{1}{2}\left[\left(k_1[L_f] + k_2[L_c] + k_{-1} + k_{-2}\right)^2 - 4\left(k_1[L_f]k_{-2} + k_2[L_c]k_{-1} + k_{-1}k_{-2}\right)\right]^{1/2}. \tag{4.11}$$

Eqs. 4.5-4.11 show that the relationship between the autocorrelation function and equilibrium and rate constants is quite complex. It is not readily apparent what experimental conditions will yield data that also contain information about nonfluorescent competitors. By taking into consideration this relationship and the limits of detection and sensitivity of our technique, criteria were defined that, if satisfied, should yield autocorrelation curves containing significant information about the thermodynamics and kinetics of nonfluorescent competitors. We continue to explore the experimental conditions that allow us to meet these criteria by determining the range of permissible concentrations (of ligand), densities (of surface binding sites) and characteristic rates.

The magnitude of the autocorrelation function at $\tau = 0$, $G_s(0)$, is inversely related to the average number of fluorescent molecules in the observed volume. To obtain autocorrelation functions with magnitudes large enough to be accurately measured, the average number of fluorescent molecules in the observed volume has to be small. We think that $G_s(0) > 0.05$ is an appropriate limit that will allow for the acquisition of accurate measurements. Additionally, $G_s(0)$ will have to be sufficiently large compared to $G_a(0)$ to ensure that fluorescence fluctuations due to surface binding kinetics make a significant contribution to the observed FCS curves.

The general expressions for $G(\tau)$ and $G_s(\tau)$, as published by Lieto and Thompson (*3*), contain w-functions and the roots of a fourth order polynomial. At the reaction limit, $G_s(\tau)$ condenses to a much simpler sum of exponentials as seen in 4.5. For most conditions we have examined thus far, the probability that a fluorescent ligand rebinds to a surface binding site within the observed area is very low. However, if rebinding does present a problem, we can ensure the system approaches the reaction limit by minimizing

the density of surface binding sites. We can alternatively increase the concentration of reporter-ligand and/or competitor so as to decrease the density of free binding sites.

The fluorescence fluctuations due to association and dissociation kinetics will have to be sufficiently fast to allow for the measurement of $G_s(\tau)$. Typically, TIR-FCS can only be used to study systems with characteristic times of 10 s or less. To ensure that $G_s(\tau)$ has significant information about k_{-2}, we initially defined conditions for which either λ_1 differs from k_{-1} by a factor of 2 and $s_1 > 0.5$, or λ_2 differs from k_{-1} by a factor of 2 and $s_2 > 0.5$ (see below).

4.1.2 Model System

Fc receptors modulate immune responses by binding antibodies through their Fc regions and signaling to downstream effectors. In mice, there are four known Fc receptors that recognize the IgG class of antibodies: FcγRI, FcγRII, FcγRIII and FcγRIV (*7*). FcγRI is a high affinity receptor that displays nanomolar affinity for its target antibody, IgG2a. The remaining Fcγ receptors display moderate affinity (1-10 μM) for a broader spectrum of antibodies.

FcγRII is expressed in many cells types, including dendritic cells, macrophages and B- and T-lymphocytes. It induces endocytosis and phagocytosis when crosslinked by antigen-bound antibody (immune) complexes. Mutations in the human homologue of FcγRII can give rise to autoimmune diseases like systemic lupus erythematosus (*8, 9*). Hence, FcγRII is a potential therapeutic target, and of immense interest to the medical community.

FcγRII consists of two extracellular immunoglobulin domains (designated D1 and D2 in Figure 4.1), a single transmembrane helix and an intracellular region that signals

downstream. Crystal structures of the extracellular region of several human Fcγ receptors have been solved, both alone and in complex with the Fc regions of IgG (*10-12*). The crystal structure of human FcγRIIIA in complex with IgG1 Fc region suggests that an antibody can only bind one Fcγ receptor (*12*). Mutagenesis studies and crystal structures show that only one of the immunoglobulin domains (D2 in FcγRII) binds IgGs (*13-15*). These findings suggest that the stoichiometry of FcγRII-IgG binding is 1:1. Hence, the theoretical autocorrelation function also assumes 1:1 binding.

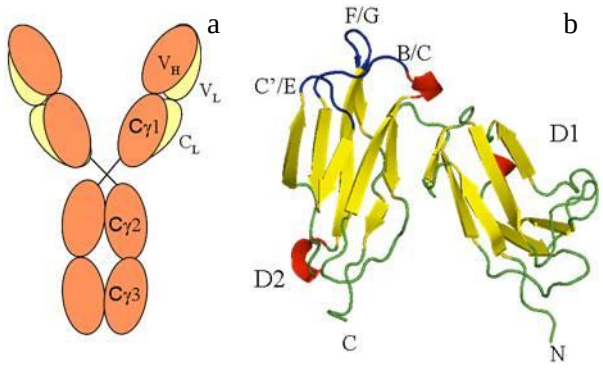

Figure 4.1: Structure of IgG1 and extracellular region of FcγRII. (a) IgG are composed of two light and heavy chains. The lights chains fold into a variable domain (V_L) and a constant domain (C_L). In IgG1, the heavy chains fold into one variable domain (V_H) and three constant domains (Cγ). (b) Extracellular region of FcγRII consisting of two immunoglobulin domains, D1 and D2. The IgG binding site on FcγRII has been mapped onto loops B/C, C'/E and F/G on D2. X-crystal-structure obtained from the Protein Data Bank (PDB entry 2fbs). The three loops bind the hinge region between Cγ1 and Cγ2 on IgG.

As mentioned above, TIR-FCS has been employed to measure the kinetic parameters of mouse IgG reversibly interacting with membrane-bound FcγRII (*2*). These measurements (K_d = ~1 μM; k_{on} = ~1 $\mu M^{-1}s^{-1}$; k_{off} = ~1 s^{-1}) are consistent with those obtained by other methods (*16-18*). To see whether these values would change with membrane-bound antibodies, complementary experiments were conducted where IgG was immobilized on supported planar bilayers and the soluble, extracellular region of FcγRII (sFcγRII) served as the fluorescently labeled ligand (*19*). TIRFM and TIR-FPR

(fluorescence photobleaching recovery) measurements showed that the thermodynamic and kinetic parameters did not change when the antibodies were immobilized on a planar substrate. In the present work, an experimental system consisting of membrane-bound antibodies and fluorescent sFcγRII in solution was used. Potential nonfluorescent competitors were derived from the regions of FcγRII that bind IgG. The crystal structure discussed above (*12*) and ELISA measurements conducted on FcγRII peptide libraries (*20*) were used as a guide to construct peptides that might compete with sFcγRII to bind IgG.

4.2 Materials and Methods

4.2.1 Cell Culture

A Chinese hamster ovary (CHO) cell line, D1959, which secretes sFcγRII, was provided by J. C. Unkeless at the Mount Sinai Medical School (*21*). The CHO cells were grown in Dulbecco's Modified Eagle Medium (DMEM/F-12) supplemented with 10% bovine calf serum, 100 units/mL penicillin, 100 µg/mL streptomycin, 1 mM sodium pyruvate, 2 mM L-glutamine and 2 µM methotrexate (Sigma-Aldrich, St. Louis, MO), in a humidified incubator at 37 °C under 5% carbon dioxide. All cell culture reagents were of the Gibco® brand (Invitrogen, Carlsbad, CA) unless otherwise stated.

The mouse IgG1, 1B7.11, was obtained from a hybridoma cell line of the same name (American Type Culture Collection, Rockville, MD). Except for the absence of methotrexate, 1B7.11 cells were cultured in the same way as the CHO cells above.

4.2.2 Purification of sFcγRII

Soluble FcγRII was purified from the CHO cell supernatant via affinity chromatography with 2.4G2-conjugated Sepharose 4B, as previously described (*19*).

(2.4G2 is an antibody against mouse FcγRII.) The receptor was eluted using 100 mM sodium acetate, 150 mM sodium chloride, pH 4.0, and immediately dialyzed against PBS. Purified sFcγRII was stored in PBS at 4 °C.

4.2.3 Purification of 1B7.11 Antibody

The 1B7.11 antibody was isolated from the 1B7.11 hybridoma supernatant. Briefly, the supernatant was passed over an affinity column consisting of dinitrophenyl-human serum albumin conjugated to Sepharose 4B (Sigma-Aldrich, St. Louis, MO) (*2*). The antibody was eluted with N-2,4-dinitrophenylglycine (DNP-G; Sigma-Aldrich, St. Louis, MO) in phosphate buffered saline (PBS; 50 mM sodium phosphate, 150 mM sodium chloride, 0.01 % sodium azide). The eluant was extensively dialyzed against PBS to remove DNP-G. Anion exchange chromatography was performed to remove residual DNP-G. Briefly, 1B7.11 fractions was dialyzed against an ion exchange buffer (10 mM sodium phosphate (monobasic); 100 mM sodium chloride; 0.01 % sodium azide, pH 5.7), concentrated and applied to a Dowex 1x8-200 column (5 mL; Acros Organics, Morris Plains, NJ). 1B7.11 was eluted using the same ion exchange buffer and immediately dialyzed against PBS. Purified 1B7.11 was stored in PBS at 4 °C.

4.2.4 Fluorescence Labeling

Fluorescein isothiocyanate (FITC; Invitrogen, Carlsbad, CA) was used to fluorescently label primary amines in sFcγRII and 1B7.11. A ~5 μM solution of either protein in 100 mM sodium bicarbonate, pH 9.2 was incubated with a 25-fold molar excess of FITC for 1 h at room temperature. FITC was initially dissolved in dimethylsulfoxide (DMSO) such that in the final reaction mixture there was less than 1% (v/v) DMSO. Gel filtration chromatography using Sephadex G-50 was employed to

remove excess dye. Eluted protein was dialyzed against PBS. Labeling ratios for sFcγRII (~0.5) and 1B7.11 (~1) were determined spectrophotometrically, assuming the following molar absorptivities: ε_{280}(1B7.11, IgG) = 210 000 M^{-1} cm^{-1}, ε_{280} (sFcγRII) = 33 000 M^{-1} cm^{-1}; ε_{280} (fluorescein) = 75 000 M^{-1} cm^{-1}.

4.2.5 Sample Preparation

All phospholipids were purchased from Avanti Polar Lipids (Birmingham, AL). Aliquots of dinitrophenylaminocaproyl-dipalmitoylphosphatidylethanolamine (DNP-cap-DPPE) and dipalmitoylphosphatidylcholine (DPPC) at DNP-cap-DPPE molar fractions of 0 and 0.25 were dried under nitrogen to a thin film. Residual chloroform was removed by centrifuging the mixtures *in vacuo* overnight. The dried phospholipids were reconstituted in water to make 2 mM phospholipid suspensions. To make small unilamellar vesicles (SUVs), the suspensions were sonicated to clarity. The vesicle suspension was stored in base-cleaned glass vials at room temperature and used within 72 h. Immediately prior to use, larger vesicles were pelleted by centrifuging the suspension for 30 min at 100,000 *g* in an air ultracentrifuge (Beckman Instruments, Palo Alto, CA). Only the top halves of the centrifuged vesicle suspensions were used (see below). These vesicles had diameters of about 100 nm as measured by dynamic light scattering (DLS).

Microscope (3 in. x 1 in. x 1 mm; Gold Seal® Products, Porstmouth, NH) and fused silica (0.25 in. x 1 in. x 1 mm; Quartz Scientific, Fairport Harbor, OH) slides were cleaned by boiling in ICN detergent (MP Biomedicals, Solon, OH) diluted in water. The slides were alternatively bath sonicated for 30 min and rinsed extensively in deionized water for two rounds, and dried at 120 °C. Immediately prior to collecting data, the substrates were further cleaned in an argon ion plasma cleaner (PDC-3XG; Harrick

Scientific, Ossining, NY) for 15 min at room temperature. Fused silica slides were mounted on microscope slides using double sided, 0.13 mm thick, tape (part no. 021200-64988; 3M Corp., St. Paul, MN). The SUV suspension (60 µL) was subsequently injected into the sample chamber created by the fused silica substrate and microscope cover slip. The sample slides were incubated at room temperature for an hour to allow the SUVs to fuse and form supported planar membranes. Excess vesicles were removed by washing with PBS (10X, 200 µL). The samples were incubated with ovalbumin (200 µL, 10 mg/mL) for 30 min to block nonspecific binding sites, prior to the addition of saturating amounts of 1B7.11 (200 µL, 9 µM, 30 min). The sample chambers were again washed with PBS (10X, 200 µL) to remove unbound 1B7.11. Finally, the samples were treated with desired concentrations of F-sFcγRII and nonfluorescent competitor.

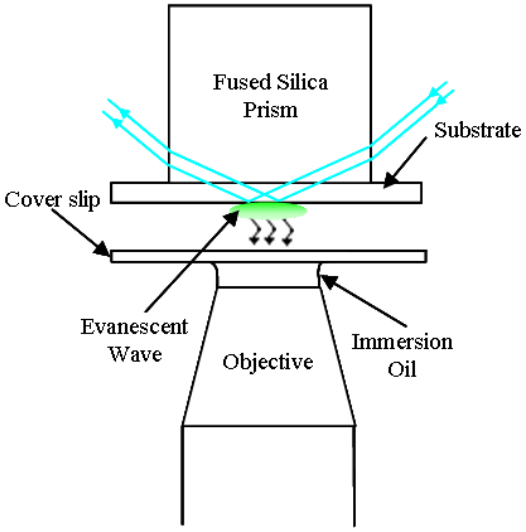

Figure 4.2: Through-prism TIRFM.

4.2.6 TIRFM Instrumentation

TIRFM was used to verify that 1B7.11 and F-sFcγRII were binding specifically to the surface and to measure the equilibrium dissociation constants of these specific interactions. The technique was also used to determine whether the various peptides

were behaving as competitors. Samples were imaged using an inverted fluorescence microscope (Zeiss Axiovert 35, Carl Zeiss Microimaging, Thornwood, NY). A fused silica prism was used to totally internally reflect a 488 nm laser beam, generated by an argon ion laser (Innova 90-3, Coherent, Palo Alto, CA), at the interface between the fused silica substrate and liquid medium, or sample. The resulting evanescent wave excited fluorescence in the 100 nm section of the sample adjacent to the fused silica substrate, as shown in Figure 4.2. A single-photon counting photomultiplier (RCA C31034A, Lancaster, PA) was used to detect the emitted fluorescence. SigmaPlot was used to fit the measured fluorescence to appropriate models.

4.2.7 Experiments

To determine whether peptides behaved as nonfluorescent competitors, TIRFM binding curves were obtained as a function of the peptide concentration at a F-sFcγRII concentration that is close to or below the mid-point of the F-sFcγRII/1B7.11 binding curve (see Figure 4.7b). Peptides that compete with F-sFcγRII to bind surface-bound 1B7.11 cause the surface-associated fluorescence to decrease as a function of the peptide concentration. Resulting curves were fit to the equilibrium binding model shown in Eq. 4.12:

$$F = \frac{QK_1[L_f]}{1 + K_1[L_f] + K_2[L_c]} \qquad 4.12$$

to obtain the peptide/1B7.11 association constant K_2. Q, a free parameter, is a proportionality constant. The association constant, K_1, pertaining to F-sFcγRII/1B7.11 binding and the concentration, $[L_f]$, of F-sFcγRII were fixed at their known values.

4.3 Results

4.3.1 Theoretical Work to Find Optimal Experimental Conditions

To find experimental conditions that would be most likely to yield autocorrelation curves containing significant information about both the fluorescent ligand and nonfluorescent competitor, we systematically explored the parameter space to find conditions that satisfied the criteria defined in section 4.1.1. Specifically, there are ten variables that affect the autocorrelation function: h, d, R_z, S, k_{-1}, k_{-2}, K_1, K_2, X_f and X_c. These variables were assigned a range of values that are typically seen associated with them (see Table 1). The values in Table 1 were used in 4.2-4.11 to find the conditions that would allow us to meet the criteria detailed above. We found that $\lambda_{1,2}$ only differ from k_{-1} by a factor of 2 and $s_{1,2} > 0.5$ when $K_1 = 10^7$ M^{-1}. Figure 4.3 shows that the autocorrelation function's dependence on α becomes more pronounced as α decreases. Given that $\alpha = k_{-2}/k_{-1}$ and $k_{-1} = 0.1$ s^{-1}, the shape of $G(\tau)$ is most affected by k_{-2} when $k_{-2} < k_{-1}$, i.e. when the nonfluorescent competitor binds the surface binding site more tightly than the fluorescent ligand. Furthermore, the effect of the nonfluorescent competitor on $G(\tau)$ is only seen at long correlation times ($\tau = \sim$10-100 s; see Figure 4.3). To sufficiently sample fluorescence fluctuations that occur at these frequencies and thereby, measure k_{-2}, we have to monitor the fluorescence over the course of many minutes, possibly hours. One potential difficulty is that our samples may not be stable for so long.

Table 4.1: TIR-FCS Variables and Associated Values

h	0.5 μm
d	0.1 μm
R_z	4000 s^{-1}
S	1 – 3000 molec μm^{-2}
k_{-1}	0.1 – 100 s^{-1}
K_1	10^4 – 10^7 M^{-1}
X_f (= $K_1[L_f]$	0.01 – 10
X_c(= $K_2[L_c]$	0.01 – 10

K_1 values were obtained from the corresponding range of k_{-1} values and the assumption that k_1 = 10^6 $M^{-1}s^{-1}$.

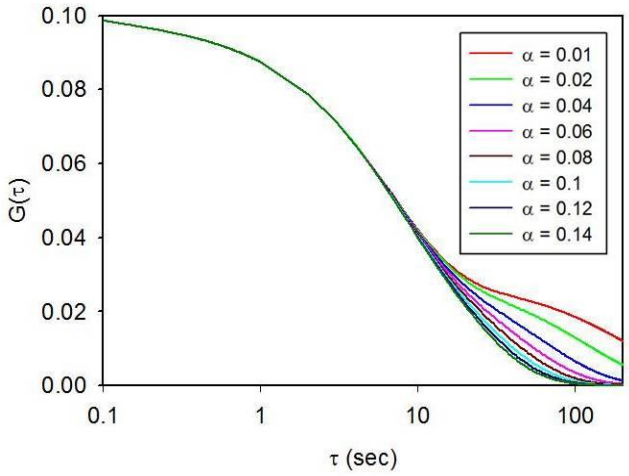

Figure 4.3: Sample Autocorrelation Plots with a Significant Dependence on k_{-2}. Autocorrelation functions computed using S = 30 molec μm^{-2}, K_1 = 10^7 $M^{-1}s^{-1}$, k_1 = 10^6 $M^{-1}s^{-1}$, k_{-1} = 0.1 s^{-1}, X_f = 0.5 and X_c = 5.

As the equilibrium constant for the binding of sFcγRII to IgG is ~10^6 M^{-1}, TIR-FCS data will be unlikely to contain significant information about the kinetics of nonfluorescent molecules that compete with fluorescent sFcγRII to bind membrane-bound IgG (see Figure 4.4a). While TIR-FCS may not allow us to measure rate constants, Eq. 4.6 shows that $G_s(0)$ is dependent on X_c and thereby, K_2. Hence, TIR-FCS experiments may yet yield equilibrium constants of nonfluorescent competitors interacting with membrane-bound receptors (see Figure 4.4b).

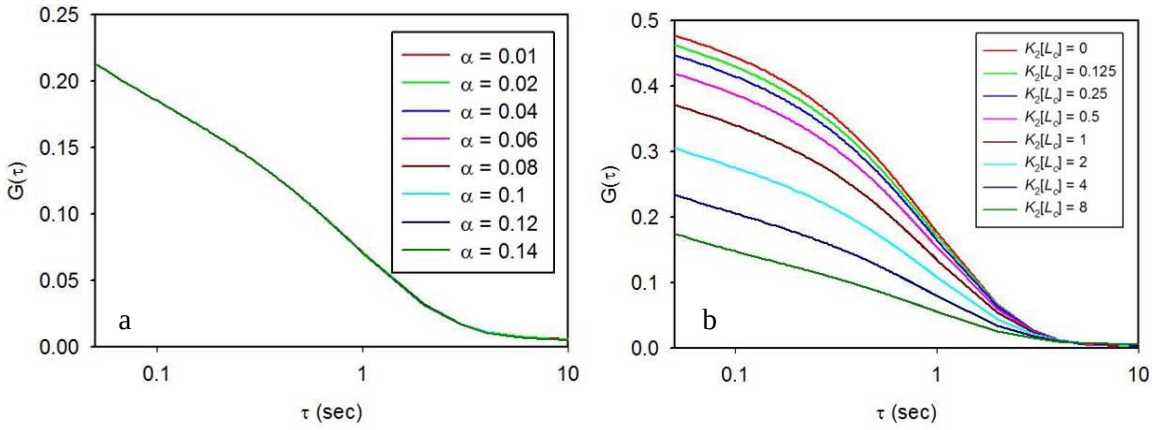

Figure 4.4: Sample Autocorrelation Plots with No Significant Dependence on k_{-2}. Autocorrelation functions were computed at S = 30 molec μm^{-2}, $K_1 = 10^6$ M^{-1}, $k_1 = 10^6$ $M^{-1}s^{-1}$, $k_{-1} = 1$ s^{-1} and $X_f = 0.01$. In (a) $X_c = 5$ and $0.01 \leq \alpha \leq 0.14$. In (b) $0 \leq X_c \leq 8$ and $\alpha = 0.1$.

Upon reviewing the criteria, we think we would get a better indication of whether the autocorrelation function contains significant information about k_{-2} by comparing rates obtained in the presence and absence of nonfluorescent competitors. Therefore, we will define the conditions where either λ_1's or λ_2's obtained in the presence and absence of competitor differ by a factor of 2 and the amplitudes associated with these rates are significant. This new criterion may change our understanding so that the conditions for which k_{-2} can be measured are broader. Reducing the fraction of fluorescently labeled reporter may further increase the conditions under which we can obtain k_{-2}.

4.3.2 Experimental Work to Establish the Model System

To test the nonfluorescent competitor theory, we wanted to establish a model system in which nonfluorescent molecules compete with the fluorescently labeled soluble, extracellular portion of FcγRII to bind the anti-DNP IgG, 1B7.11, immobilized on DNP-cap-DPPE – containing supported planar membranes (see Figure 4.5). Detailed below is the progress that has been made in realizing this system.

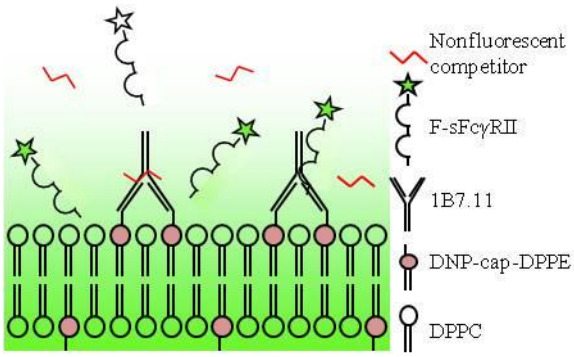

Figure 4.5: Schematic of Experimental System. Nonfluorescent competitors compete with F-sFcγRII to bind membrane-bound 1B7.11. The solid phase membrane is made of phospholipids, DNP-cap-DPPE and DPPC (see below). The green background represents the evanescent wave produced by TIR illumination.

4.3.2.1 1B7.11 was specifically immobilized on DNP-cap-DPPE – containing supported planar membranes.

The mouse IgG1, 1B7.11, is an antibody against trinitrophenyl (TNP). As TNP-conjugated phospholipids are not commercially available, 1B7.11 was immobilized on membranes containing dinitrophenylaminocaproyl-dipalmitoylphosphatidylethanolamine (DNP-cap-DPPE). The specificity of fluorescently labeled 1B7.11 (F-1B7.11) for solid-phase membranes containing 25 mole per cent DNP-cap-DPPE and 75 mole per cent dipalmitoylphosphatidylcholine (DPPC) was examined using TIRFM. The surface-associated fluorescence of DNP-cap-DPPE/DPPC membranes treated with F-1B7.11 and washed with PBS was significantly higher than that of DPPC membranes treated with F-1B7.11 (Figure 4.6). These results show that F-1B7.11 binds specifically to DNP-cap-DPPE/DPPC membranes. In membranes with 25 mole per cent DNP-cap-DPPE, 9 μM F-1B7.11 saturated 1B7.11 binding sites on the membrane.

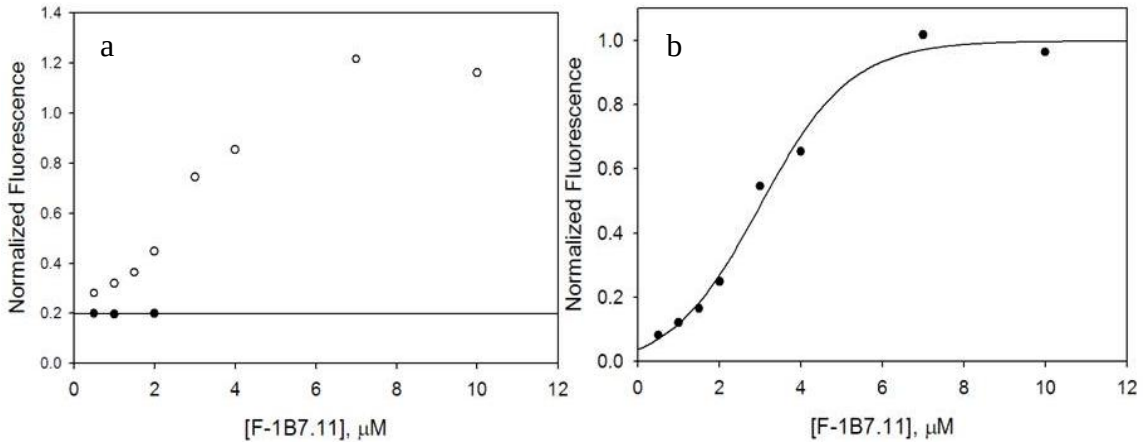

Figure 4.6: Binding of F-1B7.11 to DNP-cap-DPPE/DPPC Planar Membranes. (a) Normalized surface-associated fluorescence of DNP-cap-DPPE/DPPC (25:75, mol:mol) (○) and DPPC (•) membranes treated with F-1B7.11 and washed. The data for the DPPC membranes were fit to a line. (b) Normalized fluorescence obtained by subtracting the DPPC data from the data associated with DNP-cap-DPPE/DPPC membranes.

4.3.2.2 F-sFcγRII binds specifically to membrane-bound 1B7.11.

TIRFM was used to obtain binding curves for the association of F-sFcγRII and membrane-bound 1B7.11. DNP-cap-DPPE/DPPC (25:75, mol:mol) membranes were treated with saturating amounts of 1B7.11 (9 μM) and washed. The surface-associated fluorescence of 1B7.11-coated membranes was measured as a function of F-sFcγRII concentration (Figure 4.7a). The fluorescence of DNP-cap-DPPE/DPPC membranes that had not been treated with 1B7.11 was also measured as a function of F-sFcγRII concentration (Figure 4.7a). The difference in fluorescence between the 1B7.11-treated and –untreated membranes as a function of F-sFcγRII concentration, seen in Figure 4.7b, has the appearance of a conventional binding isotherm. This plot was fit to a model of reversible, bimolecular binding given by

$$\frac{F}{F_{\max}} = \frac{[A]}{K_d + [A]}, \qquad 4.13$$

Where F/F_{max} is the normalized fluorescence, [A] is the concentration of the fluorescent ligand and K_d is the dissociation constant. The free parameters were K_d and F_{max}. It was determined that F-sFcγRII binds 1B7.11 with a dissociation constant of 1.1±0.4 μM. This value is consistent with dissociation constants obtained for the binding of sFcγRII and another membrane-bound mouse IgG, GK14.1 (*19*). It is approximately equivalent to dissociation constants obtained for IgG in solution and FcγRII reconstituted in planar membranes (*2*, *16-18*).

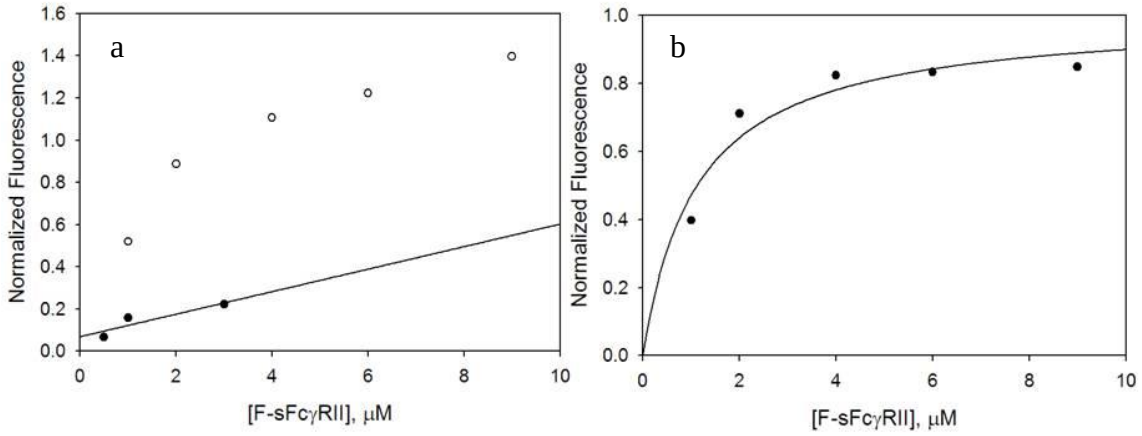

Figure 4.7: Equilibrium Binding of F-sFcγRII to 1B7.11-Coated DNP-cap-DPPE/DPPC Membranes. (a) Normalized surface-associated fluorescence of samples containing F-sFcγRII in the presence (°) and absence (•) of membrane-bound 1B7.11. The data from membranes with no 1B7.11 were fit to a line. (b) Normalized fluorescence associated with 1B7.11-bound F-sFcγRII, obtained by subtracting theoretical values from the line in (a) from the fluorescence data for membranes with 1B7.11. The difference data were fit to a one-site binding model, which yielded the equilibrium dissociation constant (K_d=1.1±0.4 μM).

4.3.2.3 Identification of peptide that competes with F-sFcγRII to bind 1B7.11 immobilized on supported planar membranes.

Several mutagenesis studies and crystal structures have identified three loops (B/C, C'/E and F/G) in the immunoglobulin domain, D2, of Fcγ receptors that are responsible for binding IgGs (*11-15*). ELISA measurements showed that two peptides derived from the B/C and F/G loops inhibit the binding of immune complexes to sFcγRII

(*20*). Hence, we had these two peptides (HSWRNKLLNR (peptide A) and KGSLGRTLHQSK (peptide B)) synthesized at the Microprotein Sequencing & Peptide Synthesis Facility at UNC-CH. A third peptide, HSWRNKLLNRISFFHNEKSVR-YHHYS (peptide C), that contains residues from both B/C and C'/E loops was also synthesized. TIRFM experiments were used to confirm whether these peptides inhibit the binding of F-sFcγRII to 1B7.11.

TIRFM was used to measure the surface-associated fluorescence of 1B7.11-coated membranes treated with 1.5 μM F-sFcγRII, as a function of nonfluorescent competitor concentration. Measurements of the surface-associated fluorescence of 1B7.11-coated membranes with 1.5 μM F-sFcγRII, as a function of the unlabeled sFcγRII concentration, show a nice monotonic decrease, as would be expected for a nonfluorescent competitor (Figure 4.8). However, the fluorescence associated with 1B7.11-coated membranes and F-sFcγRII did not decrease with increasing concentrations of peptide A, peptide B or a mixture of the two (data not shown). These results indicate that peptides A and B failed to compete with F-sFcγRII to bind 1B7.11. This outcome is unexpected as ELISA experiments showed both peptides inhibit the binding of immune complexes to sFcγRII (*20*). As peptides A and B only contain residues from one of the three loops that are thought to form the IgG binding site on FcγRII, it is possible that they alone cannot block the FcγRII binding site on 1B7.11, and thereby prevent F-sFcγRII from binding the membrane-bound receptor.

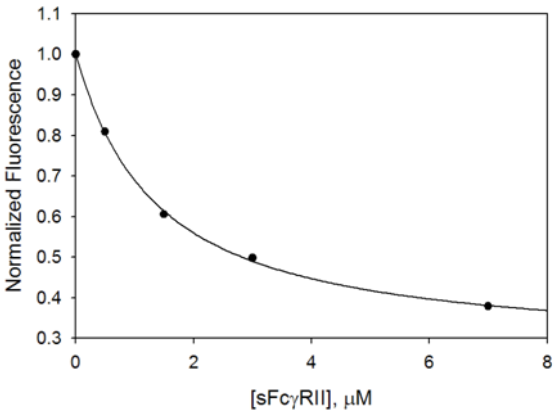

Figure 4.8: Control Measurements with Nonfluorescent sFcγRII. Equilibrium binding curves of 1.5 μM F-sFcγRII and 1B7.11 obtained as function of sFcγRII.

Peptide C, which contains residues from two of the three important loops, was insoluble in PBS (0.05 M sodium phosphate, 0.15 M NaCl, 0.01% NaN_3) at pH 7.4. Peptide C dissolved when the pH of the buffer was lowered to ~6.3. TIRFM experiments, conducted in PBS at pH 6.3, showed that the fluorescence of F-sFcγRII interacting with membrane-bound 1B7.11 did not decrease with increasing concentrations of peptide C (data not shown). However, when the same experiments were conducted in conditions of low salt (0.01 M sodium phosphate, 0.03 M NaCl, 0.01% NaN_3, pH 6.3), the fluorescence decreased, indicating peptide C successfully blocked F-sFcγRII from binding 1B7.11 (see Figure 4.9). However, it was observed that at such low salt concentrations, F-sFcγRII bound nonspecifically to DNP-cap-DPPE/DPPC membranes that had not been treated with 1B7.11 (data not shown). Therefore, this design of a negative control measurement of the specificity may not be adequate for low salt conditions. Instead, replicating the data shown in Figure 4.8 with the new solution conditions might be a better strategy. An alternate approach may include modifying the peptide sequence to increase its solubility at the higher pH and salt concentration, while

retaining its ability to compete with sFcγRII to bind 1B7.11. The use of organic co-solvents such a DMSO or dimethyl formamide (DMF) might also be a viable option.

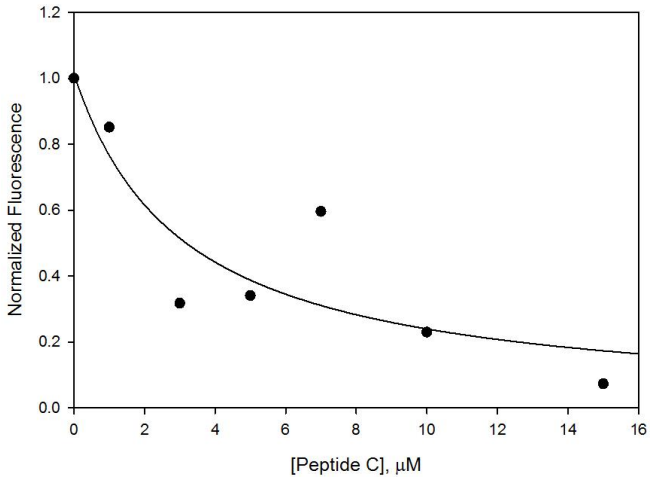

Figure 4.9: Nonfluorescent Peptide Competing with F- sFcγRII. Equilibrium binding curve of 0.8 μM F-sFcγRII and 1B7.11 obtained as a function of peptide C. The data were fit to the binding model in Eq. 4.14 to obtain K_2 ($K_2 = 0.6 \pm 0.2\ \mu M^{-1}$).

4.4 Conclusion

Progress was made towards identifying experimental conditions that are likely to yield autocorrelation curves containing significant kinetic information about nonfluorescent competitors. Towards this end, criteria that need to be satisfied to obtain informative autocorrelation curves were defined. Nonfluorescent competitor theory was systematically explored to identify experimental conditions that would satisfy the predetermined criteria. Few experimental conditions were found to meet all the criteria. In reviewing the criteria, however, it was determined that some of the criteria may not necessarily lead to the acquisition of data that contain significant kinetic information about nonfluorescent competitors. As a result, new criteria have been proposed. The theory will have to be revisited with these new criteria in mind to find optimal

experimental conditions that are likely to yield data from which kinetic information about nonfluorescent competitors can be extracted.

Work was conducted to establish a nonfluorescent competitor test system consisting of the IgG, 1B7.11, and the soluble portion of the Fc receptor, FcγRII. 1B7.11 was specifically immobilized on solid-phase, supported planar membranes. TIRFM measurement showed that F-sFcγRII specifically binds membrane-bound 1B7.11 with a binding constant of 1.1±0.4 μM, a value that is consistent with that obtained by Gesty-Palmer and Thompson (27). Additionally, TIRFM binding isotherms showed that unlabeled sFcγRII inhibits the binding of F-sFcγRII to membrane-bound 1B7.11. These experiments demonstrate that the system behaves as expected. Additionally, a peptide that appears to compete with F-sFcγRII to bind membrane-bound 1B7.11 was identified. However, if this peptide is to be used to test the nonfluorescent competitor theory, the model system at this point requires some further optimization.

4.5 References

1. Thompson, N. L., Pero, J. K. (2006) Total internal reflection-fluorescence correlation spectroscopy, in Reviews in Fluorescence Springer, New York, Vol. 3, pp. 215-237.

2. Lieto, A. M., Cush, R. C. and Thompson, N. L. (2003) Ligand-receptor kinetics measure by total internal reflection with fluorescence correlation spectroscopy. *Biophysical Journal 87,* 3294-3302.

3. Lieto, A. M. and Thompson, N. L. (2004) Total internal reflection with fluorescence correlation spectroscopy: nonfluorescent competitors. *Biophysical Journal 87*, 1268-1278.

4. Thompson, N.L., Burghardt, R.P., Axelrod, D. (1981) Measuring surface dynamics of biomolecules by total internal reflection fluorescence with photobleaching recovery or correlation spectroscopy. *Biophysical Journal 33*, 435-454.

5. Starr, T.E., Thompson, N.L. (2001) Total internal reflection with fluorescence correlation spectroscopy: combined surface reaction and solution diffusion. *Biophysical Journal 80*, 1575-1584.

6. Lagerholm, B.C., Thompson, N.L. (1998) Theory for ligand rebinding at cell membrane surfaces. *Biophysical Journal* 74: 1215-1228.

7. Nimmerjahn, F., Ravetch, J. V. (2008) Fcγ receptors as regulators of immune responses. *Nature Reviews Immunology 8*, 34-47.

8. Su, K. Li, X., Edberg, J. C. Wu, J., Ferguson, P., Kimberly, R. P. (2004) A promoter haplotype of the immunoreceptor tyrosine-based inhibitory motif bearing FcγRIIb alters receptor expression and associates with autoimmunity. II. Differential binding of GATA4 and Yin-Yang1 transcription factors and correlated receptor expression and function. *Journal of Immunology 172*, 7192-7199.

9. Su, K. Wu, J., Edberg, J. C., Li, X., Ferguson, P., Cooper, G. S., Langefeld, C. D., Kimberly, R. P. (2004) A promoter haplotype of the immunoreceptor tyrosine-based inhibitory motif bearing FcγRIIb alters receptor expression and associates with autoimmunity. I. Regulatory FCGR2B polymorphisms and their association with systemic lupus erythematosus. *Journal of Immunology 172*, 7186-7191.

10. Garman, S. C., Kinet, J. P., Jardetzky, T. S. (1998) Crystal structure of the human high-affinity IgE receptor. *Cell 95*, 951-961.

11. Maxwell, K. F., Powell, M. S., Hulett, M. D., Barton, P. A., McKenzie, I. F., Garret, T. P., Hogarth, P. M. (1999) Crystal structure of the human leukocyte Fc receptor, FcγRIIa. *Nature Structural Biology 6*, 437-442.

12. Sondermann, P., Huber, R., Oosthuizen, V., Jacob, U. (2000) The 3.2-Å crystal structure of the human IgG Fc fragment-FcγRIII complex. *Nature 406*, 267-273.

13. Hogarth, P.M., Hulett, M.D., Ierino, F.L., Tate, B., Powell, M.S. and Brinkworth, R.I. (1992) Identification of the immunoglobulin biding regions (IBR) of FcγRII and FcεRII. *Immunological Reviews 124*, 21-35.

14. Hulett, M.D., Witort, E., Brinkworth, R.I., McKenzie, I.F.C. and Hogarth, P.M. (1994) Identification of the IgG binding site of the human low affinity receptor for IgG FcγRII. *Journal of Biological Chemistry 269*, 15287-15293.

15. Hulett, M.D., Witort, E., Brinkworth, R.I., McKenzie, I.F.C., Hogarth, P.M. (1995) Multiple regions of human FcγRII (CD32) contribute to the binding of IgG. *Journal of Biological Chemistry 270*, 21188-21194.

16. Poglitsch, C. L., Thompson, N. L. (1990) Interaction of antibodies with Fc receptors in substrate-supported planar membranes measured by total internal reflection fluorescence microscopy. *Biochemistry 29*, 248-254.

17. Poglitsch, C. L., Sumner, M. T., Thompson, N. L. (1991) Binding of IgG to MoFc Gamma RII purified and reconstituted into supported planar membranes as measured by total internal reflection fluorescence microscopy. *Biochemistry 30*, 6662-6671.

18. Hsieh, H. V., Thompson, N. L. (1995) Dissociation kinetics between a mouse Fc receptor (FcγRII) and IgG: Measurement by total internal reflection with fluorescence photobleaching recovery. *Biochemistry 34*, 12481-12488.

19. Gesty-Palmer, D., Thompson, N. L. (1997) Binding of the Soluble, Truncated Form of an Fc Receptor (Mouse-FcγRII) to Membrane-Bound IgG as Measure by Total Internal Fluorescence Microscopy. *Journal of Molecular Recognition 10*, 63-72.

20. Goldsmith, E. B., Erickson, B. W., Thompson, N. L. (1997) Synthetic peptides from mouse Fc receptor (moFcγRII) that alter the binding of IgG to moFcγRII. *Biochemistry 36*, 952-959.

21. Qu, Z., Odin, J., Glass, J.D., Unkeless, J.C. (1988) Expression and characterization of a truncated murine Fcγ receptor. *Journal of Experimental Medicine 167*, 1195-1210.

Chapter 5

Summary and Future Directions

Theoretical work was conducted to ease the implementation of TIR-FCS with respect to its application to the study of ligand-receptor interactions (Chapter 2, (*1*)). Autocorrelation curves depend on numerous experimental parameters that are unique to either the particular instrumental setup or biological system. This rather large parameter space complicates the identification of experimental conditions that are likely to yield autocorrelation curves with good signal-to-noise ratios, containing significant information about the thermodynamic and kinetic parameters of interest. To address this difficulty, criteria, that need to be satisfied in order to obtain informative autocorrelation curves, were defined. Parameter space was systematically explored to identify experimental conditions under which these criteria would be satisfied. This work additionally serves as a general guide to define criteria and identify experimental conditions for TIR-FCS measurements of ligand-receptor interactions.

Theoretical work has also suggested that TIR-FCS can yield kinetic information about nonfluorescent effectors and competitors (*2, 3*). To test these theoretical predictions, work was conducted to establish model systems containing a nonfluorescent effector (Chapter 3, (*4*)) and nonfluorescent competitor (Chapter 4). The nonfluorescent effector test system was to consist of the pregnane X receptor (PXR), peptides derived from co-activator and co-repressor proteins, and a PXR ligand, rifampicin. In the process

of establishing this system, it was determined that the mechanism of PXR action differs from that of other nuclear receptors. Namely, the PXR ligand, rifampicin, does not enhance the receptor's affinity for co-activator or reduce PXR's affinity for co-repressors (*4*). These results are of great biological significance, and present many avenues for further study. Needless to say, rifampicin is not an effector, and this system cannot be used to test theory pertaining to nonfluorescent effectors. However, it was shown that co-activator and co-repressor peptides compete with each other to bind PXR (*4*), thereby, allowing the system to serve as a test system for nonfluorescent competitors.

It was originally thought that a model system consisting of an IgG and the mouse Fc receptor, FcγRII, could be used to test nonfluorescent competitor theory (Chapter 4). In establishing this system, IgG were immobilized on supported planar membranes via their hapten binding site, while the soluble, extracellular portion of FcγRII (sFcγRII) was fluorescently labeled. As a competitor had not been previously identified for this system, we thought to engineer a competitor by designing peptides from the antibody binding site on FcγRII. Of the three peptides that were synthesized, one competed with fluorescent sFcγRII to bind surface-associated IgG. For reasons discussed in Chapter 4, this system would require further optimization before it could be fully implemented for the purposes of testing nonfluorescent competitor theory.

Theoretical work was also conducted to identify experimental conditions that would increase the likelihood of obtaining autocorrelation curves containing significant information about nonfluorescent competitors (Chapter 4). As in Chapter 2, criteria were defined that, if satisfied, would yield kinetic information about nonfluorescent competitors. The parameter space was then explored to identify experimental conditions

that meet these criteria. A limited number of experimental conditions that satisfy all the criteria were found. However, the criteria have since been refined to better reflect the requirements for obtaining autocorrelation curves containing relevant information. Parameter space has yet to be explored in light of these new criteria to determine allowable experimental conditions. Upon completing this theoretical work, the PXR, co-activator and co-repressor system established here can be used to test the experimental conditions.

Parallel work will have to be conducted for nonfluorescent effectors. Theoretical work will be conducted to determine experimental conditions under which kinetic information about nonfluorescent effectors can be obtained. A model system will have to be established to test these experimental conditions. The most obvious candidate system would consist of another nuclear receptor like the estrogen receptor, where the agonist (estrogen) has been shown to increase the affinity of the receptor for the relevant co-activator. Extending TIR-FCS to the study of nonfluorescent species will be a major advancement, allowing the technique to be used to study biological systems containing compounds that are not readily amenable to fluorescence labeling.

In the immediate future, however, the application of TIR-FCS to the study of simple, bimolecular interactions will be fully characterized. In fact, PXR and the SRC-1 peptide are currently being used to test the experimental conditions that were predicted to yield informative autocorrelation curves in Chapter 2. Specifically, autocorrelation curves are being obtained for PXR/F-SRC-1 interactions within a range F-SRC-1 concentrations, PXR surface site densities and pin hole sizes that are thought to satisfy the criteria that were defined in Chapter 2. Preliminary data agree with theoretical

predictions. For instance, G(0) values were found to increase with decreasing F-SRC-1 concentrations, as would be expected for variables that are inversely related. Similarly, G(0) values measured in the presence of PXR are lower than corresponding G(0) values obtained in the absence of PXR, as binding causes an increase in the apparent, local concentration of fluorescent ligand. When $G_{neg}(0)$ versus F-SRC-1 concentrations are fit to an appropriate functional form, h values of ~1 μm are obtained as would be expected given a 50 μm pin hole and the magnification of the microscope. Similarly, when $G_{pos}(0)$ versus F-SRC-1 concentrations are fit to an appropriate theoretical form, surface site densities were obtained. These values agreed with those that had been obtained from TIRFM binding isotherms (see Chapter 3). $G_{neg}(0)$ and $G_{pos}(0)$ refer to G(0) values that were obtained in the absence and presence of PXR. Additionally, off rates of about 5 s^{-1} were obtained for PXR/F-SRC-1 interactions. These values are within the same order of magnitude as those obtained using TIR-FRAP (2 s^{-1}; Chapter 3). The off rates are also independent of the F-SRC-1 concentration, indicating that rebinding is negligible.

In the long term, TIR-FCS will be transformed into a high-throughput technique by introducing appropriate microfluidic devices and high-speed imaging cameras. In addition, the technique can be applied to the study of live-cells. For instance, TIR-FCS can be used to build kinetic maps of specific ligand-receptor interactions in cells. TIRFM combined with fluorescence cross-correlation spectroscopy will facilitate the study of multiple fluorescently labeled species.

5.1 References

1. Thompson, N. L., Navaratnarajah, P., Wang, X. (2011) Measuring surface binding thermodynamics and kinetics by using total internal reflection with fluorescence correlation spectroscopy: Practical considerations. *Journal of Physical Chemistry B 115*, 120-131.

2. Thompson, N. L. (1982) Surface binding rates of nonfluorescent molecules may be obtained by total internal relfection with fluorescence correlation spectroscopy. *Biophysical Journal 38*, 327-329.

3. Lieto, A. M. and Thompson, N. L. (2004) Total internal reflection with fluorescence correlation spectroscopy: nonfluorescent competitors. *Biophysical Journal 87*, 1268-1278.

4. Navaratnarajah, P., Steele, B. L., Redinbo, M. R., Thompson, N. L. (2012) Rifampicin – independent interactions between the pregnane X receptor ligand binding domain and peptide fragments of coactivator and corepressor proteins, *Biochemistry 51*, 19-31.